Radboud Repository

Radboud University Nijmegen

PDF hosted at the Radboud Repository of the Radboud University Nijmegen

The following full text is a publisher's version.

For additional information about this publication click this link.
https://hdl.handle.net/2066/214948

Please be advised that this information was generated on 2021-11-01 and may be subject to change.

Thin-Film III-V Solar Cells

Photon Recycling and Space Application Testing

Natasha Gruginskie

Thin-Film III-V Solar Cells - Photon Recycling and Space Application Testing
Natasha Gruginskie
PhD Thesis - Radboud University, Nijmegen, The Netherlands
With summary in Dutch and Portuguese
ISBN 978-94-028-1881-9
Printed by Ipskamp Printing
Cover design by Bruna Filippozzi

Thin-Film III-V Solar Cells

Photon Recycling and Space Application Testing

Proefschrift

ter verkrijging van de graad van doctor
aan de Radboud Universiteit Nijmegen
op gezag van de Rector Magnificus prof. dr. J.H.J.M. van Krieken
volgens besluit van het college van decanen
in het openbaar te verdedigen op maandag 27 Januari 2020,
om 14:30 uur precies

door

Natasha Gruginskie

geboren op 16 juni 1992
te Porto Alegre (Brazilie)

Promotor:
Prof. dr. E. Vlieg

Copromotor
Dr. ir. J.J. Schermer

Manuscriptcommissie:
Prof. dr. U. Zeitler
Prof. dr. E.P.A.M Bakkers (*Technische Universiteit Eindhoven*)
Dr. S. Taylor (*European Space Agency*)

Thin-film III-V solar cells

Photon Recycling and Space Application Testing

Doctoral thesis

to obtain the degree of doctor
from Radboud University Nijmegen
on the authority of the Rector Magnificus prof. dr. J.H.J.M. van Krieken
according to the decision of the Council of Deans
to be defended in public on Monday, January 27, 2020
at 14:30 hours

by

Natasha Gruginskie

born on June 16, 1992
in Porto Alegre (Brazil)

Supervisor
Prof. dr. E. Vlieg

Co-supervisor
Dr. ir. J.J. Schermer

Doctoral Thesis Committee:
Prof. dr. U. Zeitler
Prof. dr. E.P.A.M Bakkers (*Eindhoven University of Technology*)
Dr. S. Taylor (*European Space Agency*)

To my mother.
I will miss you forever

Contents

Chapter 1

Introduction

The energy infrastructure of the current society is heavily dependent on fossil fuels, such as coal, oil and natural gas, which are non-renewable energy sources. By burning fossil fuels, greenhouse gases are released into the atmosphere, which are further contributing to global warming and climate change [1]. With a fast growing world population and consequent growing energy consumption [2, 3], a transition to an integrated renewable energy generation matrix will be required. In this context, the Sun is an important renewable energy source, as it provides nearly unlimited and free energy for use.

The solar energy can be harvested either with thermal systems, using sunlight heat, or with photovoltaic systems, using the sunlight photon energy collected by solar cells, directly converting it to electricity. Currently, there are many types of solar cells available, ranging from single layer organic solar cells, to monocrystalline multi-junction devices based on III-V materials (see the overview in figure 1.1). The different cell types vary enormously in cost and efficiency, and in general the higher the efficiency of a solar cell, the more expensive it is. At present, virtually all the commercially available solar panels are based on single-junction solar cells composed of mainly Silicon (Si), but in smaller quantities also of Copper-Indium-Gallium-Selenide/Sulfide (CIGS) or Cadmium-Telluride (CdTe), with efficiencies ranging between 10 and 20%. On the other hand, significantly higher efficiencies of over 40% have been demonstrated with solar cells based on III-V materials [4]. However, these cells are mainly utilized in systems where their high efficiency outweighs their high price, such as in concentrated photovoltaic (CPV) systems or space applications.

A CPV system basically collects sunlight over a large area and focuses it on a small solar cell. In this way, the size of the solar cell that is required to produce a certain power output can be reduced by several orders of magnitude. The fact that

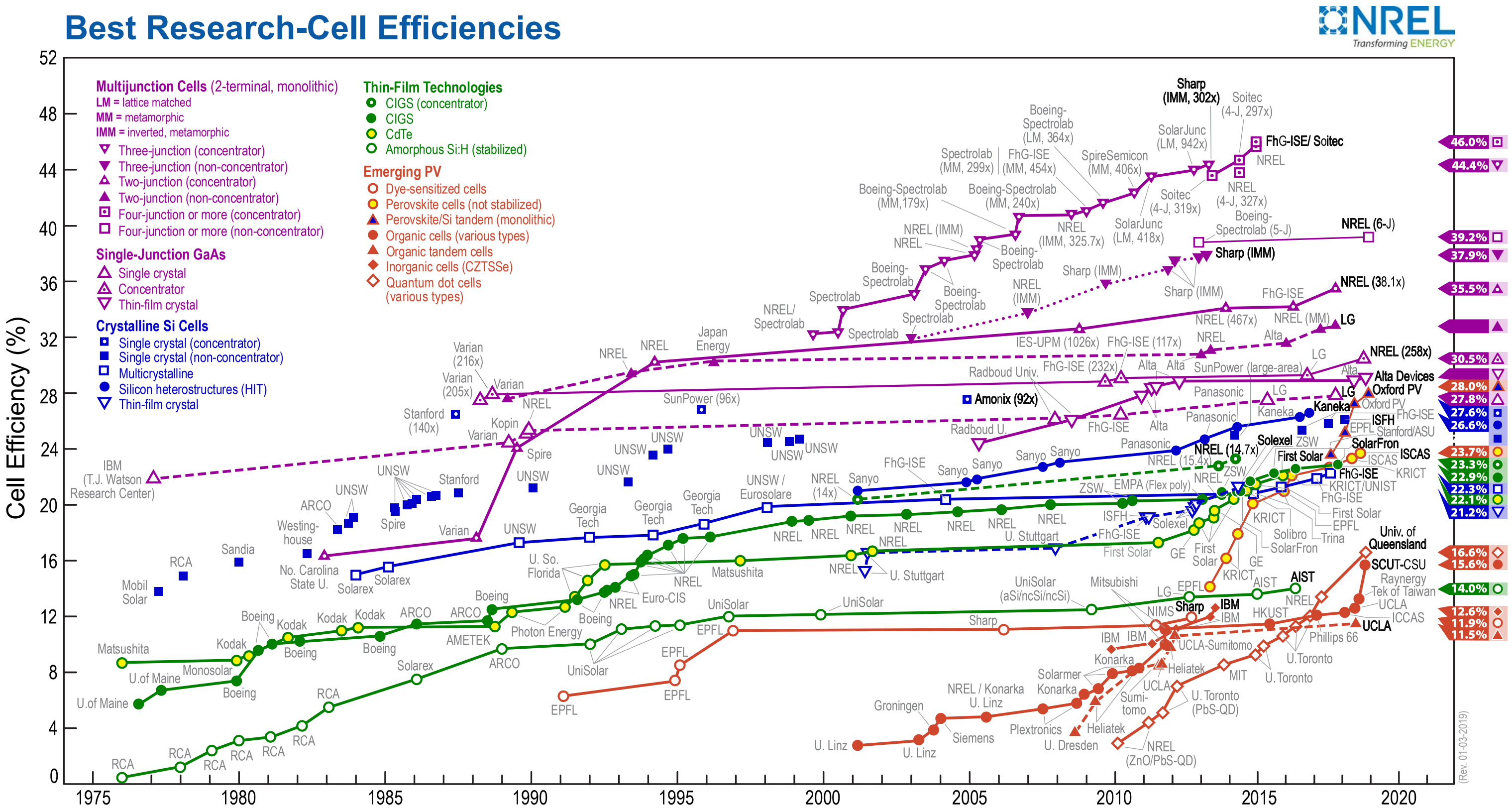

Figure 1.1: The National Renewable Energy Laboratory's best research-cell efficiency chart, displaying the highest solar cell efficiencies measured for various solar cell technologies [5]. The Applied Materials Science group of Radboud University has held three records in single-junction GaAs, one single crystal wafer based record and two thin-film cell records.

the required light concentrating optics in these systems are substantially cheaper per unit area than the solar cells allows for a reduction in the cost per watt output power. Since the solar cell in such applications only amounts to a small part of the total system costs, III-V solar cells are the most economical choice at sufficiently high concentration ratios (100×). In this context, multi-junction solar cells composed mainly of indium gallium phosphide (InGaP), gallium arsenide (GaAs) and germanium (Ge) sub-cells are widely used, as they can be tuned to efficiently absorb and convert a wide wavelength range of the incident light.

Another common application for III-V solar cells is in satellites and for space exploration purposes, where the high launch costs cause the high efficiency of the III-V solar cells to outweigh their high price. Furthermore, in these systems, the reliability of the solar cells is of great importance, since the solar cells should at least be operational in harsh space conditions during the entire mission.

1.1 III-V materials for solar cells

The semiconductor industry heavily relies on silicon, mostly because it is able to controllably form an electrically insulating oxide layer and because the material is abundantly available in nature, and therefore relatively inexpensive. For many applications, like micro-electronic circuitry, these qualities are favorable. However, silicon is an indirect band gap material and for opto-electronic circuits, semiconductors with direct band gaps, such as III-V materials, are required in order to obtain good and efficient working devices. The group of III-V semiconductor materials are formed by a one-to-one combination of elements from the third (mostly aluminum, gallium and indium) and the fifth (mostly phosphorous, arsenic and nitrogen) column of the periodic table (see figure 1.2).

In addition, III-V materials have the advantage that by changing the fractions of each element, while keeping the one-to-one ratio between third and fifth column elements constant, many material properties, such as bandgap, refractive index and resistivity to chemical processing, can be tuned. Furthermore, certain elements like zinc, carbon or silicon, can be easily added during formation of the III-V material resulting in highly controllable *p*- and *n*- type doping levels. However, III-V materials have the disadvantage that they are not able to form a stable and controllable oxide layer and most of the materials are relatively expensive because they are not yet explored at large scale.

Crystal growth techniques like liquid encapsulated Czochralski (LEC) growth, the horizontal Bridgeman (HB) method or the vertical gradient freeze (VGF) method are often employed for fabricating high quality III-V materials crystals. These methods

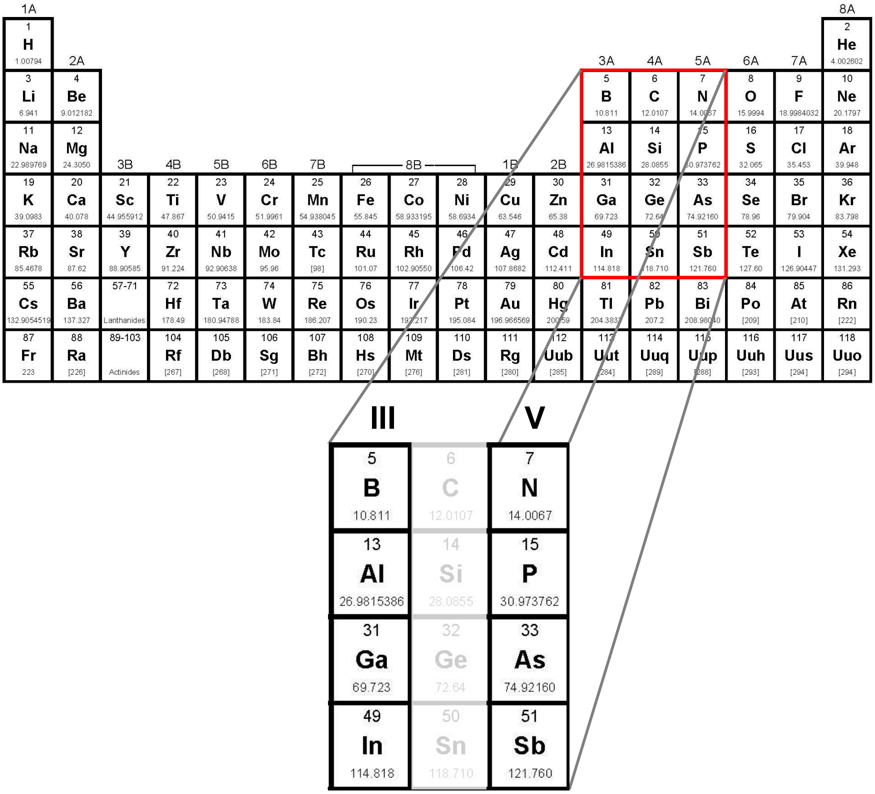

Figure 1.2: The periodic table of elements, with the relevant elements for the fabrication of III-V devices highlighted.

are usually only used to produce binary III-V compounds like GaAs and InP, because with these techniques the control of the composition for ternary or more complicated compounds is very difficult. The large crystal ingots or boules obtained in this way are usually cut into wafers. Subsequently these wafers are used as substrates or templates to produce epitaxial device layer structures utilizing crystal growth methods that allow for close control of the material composition and layer thickness. Common epitaxy techniques are liquid phase epitaxy (LPE), molecular beam epitaxy (MBE), metal organic chemical vapor deposition (MOCVD) or combinations of these techniques. In general, a thin layer or stack of layers in the order of a few micrometers is deposited on a substrate that should approximately have the same lattice constant, in order to obtain a virtually perfect single-crystalline structure.

The high production costs of III-V devices is for a large part determined by the price of the substrates that are necessary to obtain the generally desired single crystal layer structures or devices. Once a device is grown, the substrate usually does not have a function other than being an expensive carrier of the device structure. On the other hand, the most frequently used materials for these cells such as GaAs and InGaP are direct band gap semiconductors with high absorption coefficients. Therefore, a stack with a thickness of only a few micrometers of these materials is sufficient to absorb all light that the solar cell can convert into electricity. There are several methods for removal of the growth substrate, resulting in thin-film solar cells. By a selective etching process, the complete substrate can be removed using an etch stop layer that protect the solar cell layers. Another method is the Epitaxial Lift-Off (ELO) technique in which the thin-film III-V structures are separated from their wafer template so that the latter can be reused for growth of the next thin-film cell structure. In both cases, the actual thin-film structures are transferred to a low cost foreign carrier like a metal or plastic foil for stability and further processed into a genuine thin-film cell.

1.2 Thin-film GaAs solar cells

Thin-film solar cells have several application advantages over cells on the native substrate. The absence of a substrate results in final devices that are thinner and thus lighter. The cells can also be mounted on an arbitrary carrier, such as a low weight material for space applications, another low-bandgap solar cell to form a mechanically stacked tandem solar cell [6], or a good heat conductor in concentrator systems. Alternatively, with the application of a highly reflective mirror at the back surface, the incident light optical path is increased and the thickness of the active layers can be reduced, further reducing the production costs. An effective mirror also reflects most of the infra-red portion of light, reducing the overheating issue commonly faced in concentrator system applications.

The most suitable III-V material for a single junction solar cell is GaAs, since it has the optimal bandgap to match the spectral distribution of sunlight and it has produced the highest conversion rate among all types of single junction solar cells. As shown in figure 1.1, the world record for single-junction thin-film GaAs solar cells was first achieved by Radboud University in 2005, with an efficiency of 24.5% [7], and a few years later this geometry reached an efficiency of 26.1% [8], equating the performance of the best substrate based GaAs cell of the time, which was also produced at Radboud University. The current world record efficiency of 29.1% for thin-film GaAs was achieved by Alta Devices in 2018, and it is 1.3% higher than the current world record for the substrate based counterpart [4].

The superior performance of the thin-film solar cells geometry is atributed to an increased photon recycling. In the thin-film structure, radiatively emitted photons are reflected at the rear side of the cells back to the active layers, instead of being absorbed in the substrate. Because GaAs solar cells quality increased to a point where they are limited by radiative recombination, the high internal emissions in these cells make the optical design of the final devices extremely important. Theoretical studies indicate that improvements in the back-side reflectivity of the cell to a level beyond 95%, e.g. by the application of dedicated mirror-like structures, will further increase the cell efficiency super-linearly [9]. The superior performance of thin-film solar cells combined with a high power to weight ratio, flexibility, prospects for costs reduction and possibility of transferred applications brings to these devices a high potential for use in space power.

1.3 Challenges of the space environment

Most of the space applications for solar cells are in communication satellites, which are microwave repeater stations that permit two or more users with appropriate Earth stations to deliver or exchange information in various forms [10]. These satellites may operate in different orbits with varying altitude and position. The three most commonly used types of orbits are depicted in figure 1.3.

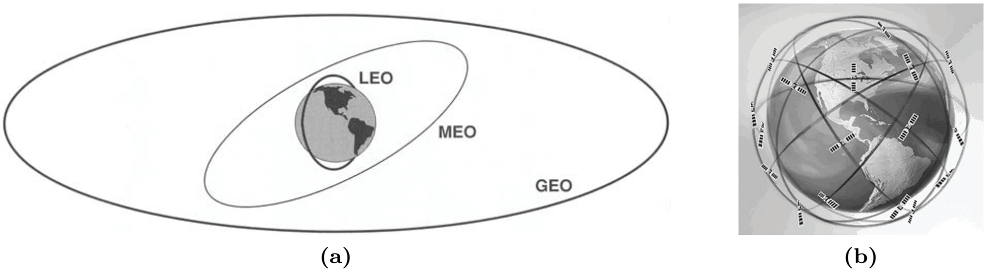

(a)

(b)

Figure 1.3: a) Depiction of the three most popular orbits for communication satellites LEO, MEO, and GEO. b) Schematic depiction of multiple orbits forming a satellite constellation, required for LEO and MEO satellites to provide continuous service [10].

A satellite in a geostationary Earth orbit (GEO) revolves around the Earth in the plane of the equator once in 24 hours, with a distance of 36,000 km. It maintains precise synchronization with the Earth's rotation and appears to remain directly above the same point on the ground. Therefore it does not require ground antennas that track the satellite. There are also 24-hour circular geosynchronous orbits that are inclined with respect to the equator. These are not called GEO because the satellite appears to move relative to the fixed point on the Earth.

Low Earth orbit (LEO) systems, on the other hand, employ satellites at altitudes ranging from 500 to 1,000 km. The shorter distance that the radio signal has to travel, requires less power for transmission and minimizes the propagation delay, as compared to GEO satellites. The altitude of a medium Earth orbit (MEO) is around 10,000 km, with transmission distance and delay greater than for LEO but still significantly less than for GEO. For both LEO and MEO systems, however, in order to obtain continuous operation of the communication channel, multiple satellites in different orbits must be used, in systems called satellite constellations (see figure 1.3b). At altitudes between LEO and MEO orbits (around 2,000 and 8,000 km) the Van Allen radiation Belt provides a zone of highly energetic charged particles captured by Earth's magnetic field. This is an inhospitable environment for most electronic components. Finally, other orbits have been used at smaller scale, such as the highly elliptical Earth orbit (HEO), that allows coverage of the northern latitudes.

All Earth-orbiting communication satellites use panels of solar cells to power their systems. Because the power output of a solar cell is proportional to the intensity of solar radiation reaching the cell, there is a seasonal variation that results from the angle between the ecliptic plane and the satellite's orbital plane. Especially for applications other than GEO, the arrangement of orbits and communication coverage requirements differ significantly, imposing unique constraints on solar power generation. These geometrical factors should provide some appreciation for the basic requirements for solar panel design. There are, however, many other factors to consider. In contrast to terrestrial applications, the space environment adds many additional challenges to the solar panel design. Reliability and durability are even more important, since after launch, repair is usually impossible. Additionally, space provides a number of environmental conditions not typically encountered in terrestrial applications, that will vary depending on the specific mission. In general the following conditions should be considered during device design:

- High vacuum: the high vacuum (10^{-8} – 10^{-15} Pa) encountered in space can cause out-gassing of volatile materials which may condense on other parts of the spacecraft. This may cause damage to the spacecraft or contaminate the surfaces of optical components such as solar panels.

- Micro-meteoroids/debris: both naturally occurring micro-meteoroids and man-made space debris might collide with the spacecraft at a high velocity (10-20 km/s). Upon impact this can inflict damage to the surface layers of the spacecraft and thereby expose underlying layers (for example solar cells) to the harsh space environment.

- Unequal charging: space crafts are exposed to naturally occurring plasma, this causes generation of photo-electrons at the spacecraft surface, leading to a build up of charge on the solar panel surface. Such a charge might discharge via the solar cells or other critical components of the panel, causing failure of the panel.

- UV radiation: on Earth most of the UV radiation (100–400 nm in wavelength) is filtered out by the atmosphere. In space, on the other hand, this UV radiation will reach the spacecraft. Potentially harmful effects include coloring of normally transparent parts (such as cell protective coatings or the mounting medium of the cover glass [11]) and the conversion of UV photons into heat. For a solar cell this would mean less light can enter the cell due to the coloring and less efficient operation of the solar cell because of the higher operating temperature [12].
- Charged particle radiation: the charged particle environment mainly consists of high-energy electrons and protons, but alpha particles, heavy ions and high-energy photons are also present. Such particles can create defects in the crystalline material of the solar cells, hence decreasing its performance [13].
- Thermal cycling: solar panels move in and out of the Earth's shadow, this induces a rapid temperature change (heating up or cooling down quickly). Differences in thermal expansion coefficients might cause stress between different layers in the solar panel, which in turn can result in cracking or delamination of one or more of the layers.
- Atomic oxygen (ATOX): molecular oxygen (O_2) and ozone (O_3) can photo-dissociate into atomic oxygen (ATOX). Since this process requires the presence of molecules it is mainly an issue for LEO, in which about 80% of the atmosphere consists of ATOX [14]. It can collide with the spacecraft, but since its penetration depth is small it only causes damage to the surface layers of a solar panel. This could give rise to problems when a flexible protective coating is used instead of a cover glass, since the polymers of such layers are generally severely damaged by ATOX.

For scientific research and exploration missions the challenges are typically even larger, depending on the type of mission, with more extreme environments. The exploration of celestial bodies further away from the sun provide a low intensity and low temperature (LILT) environment, such as the Jupiter icy moons explorer (JUICE), while other missions, such as explorations of Venus, can subject the solar cells to high intensity and high temperature (HIHT).

Lately, research has been applied to the development of the so-called high altitude pseudo-satellites (HAPS), that employ autonomous unmanned aerial vehicles (UAV) operating at the Earth stratosphere (above 20 km of altitude [15, 16]). These applications require a high power-to-weight ratio and should specifically employ optimized thin-film solar cells. The high altitude provides a large area coverage, but shields the solar cells from some of the most challenging conditions listed above. Most importantly, the severe reliability restrictions are significantly released because occurring flaws during operation can be corrected via landing and relaunching the UAV.

In view of the diversity of space systems, it is clear that in each application, a specific characteristic is required. Consequently, a more fundamental and in-depth analysis of the solar cells reliability needs to be done, in order to define which specific aspects of the solar cell development can be favorable to particular mission requirements. As technology advances and space launch becomes more accessible, not only the specific power needs to be taken into consideration, but cost-per-watt and adaptability as well. Therefore, the design of the solar cell needs to be fine-tuned, so the best balance between power generation, lifetime reliability and production costs can be found.

1.4 Scope and outline of this thesis

This thesis addresses the design and fabrication of thin-film GaAs solar cells, focusing on photon recycling mechanisms and their applicability in space missions. In chapter 2 the operational principles of solar cells are described and in chapter 3 the applied equipment and basic experimental procedures used for the studies described in this thesis are detailed. Then, a novel approach to process the bottom contact of solar cells is demonstrated in chapter 4, bringing an experimental proof-of-concept of the super-linear relation between the reflectance of the rear mirror and the open circuit voltage of the device. A detailed analysis of the performance limiting mechanisms preventing the solar cells to fully benefit from increased photon recycling is presented in chapter 5, linking important optical and electronic parameters to the solar cell output. In Chapters 6, 7 and 8 we present the investigation of the degradation mechanisms of GaAs solar cells under extreme conditions that mimic the space environment, namely exposure to electron irradiation (chapter 6), proton irradiation (chapter 7) and temperature cycling (chapter 8). Finally, chapter 9 summarizes and contextualizes the results and mechanisms identified in terms of potential applications and possibilities for further research.

Chapter 2

Basic solar cell theory

2.1 Sunlight

Light is part of the electromagnetic spectrum and its behaviour can be described both as waves with a certain wavelength λ or in terms of energy packages (photons) with discrete energies E_{ph}. The relation between the wavelength and the photon energy is given by:

$$E_{ph} = \frac{hc}{\lambda} \tag{2.1}$$

in which h is Planck's constant and c is the speed of light in vacuum. A light source is characterized by the wavelengths (photon energies) it emits. Some light sources such as lasers and LEDs only emit light within a very narrow wavelength (energy) range, whereas others such as incandescent light bulbs and the sun emit a broad spectrum of wavelengths (energies). It is important to know the spectral composition of the solar spectrum, as the spectral distribution of the light incident on a solar cell influences its performance.

The sun is approximately a black body radiator with a surface temperature of almost 6000K. Since the sun is far away and the Earth is much smaller than the sun, the sunlight arrives at the Earth's outer atmosphere as approximately parallel rays. The spectral distribution at this point has an incident power density of 1367 $\mathrm{W/m^2}$, is referred to as Air Mass Zero (AM0, see figure 2.1) and is used as a reference spectrum for space applications. The sunlight must then pass through the Earth's atmosphere in order to reach the Earth's surface. Various kinds of atoms and molecules in the atmosphere absorb, reflect and scatter (part of) the sunlight, therefore the spectrum that reaches the surface is strongly dependent on the distance the sunlight has travelled through the atmosphere. The Air Mass (AM) is a measure of how much the spectrum is affected by the atmosphere and it is given by:

$$\text{Air Mass} = \frac{1}{\cos\theta} \tag{2.2}$$

in which θ is the angle of incidence (when the sun is directly overhead, $\theta = 0$). The air mass depends on the location on Earth and the time of day and year. Therefore a standardized spectrum is used in order to allow comparison of solar cell characteristics measured at different research and quality control centres. This standardized spectrum is referred to as AM1.5 and is normalized to a total power density of 1000 W/m^2. The light that has been scattered and reflected in the atmosphere before reaching the surface of the Earth is no longer a parallel bundle and is therefore referred to as diffuse or indirect light. Up to 20% of the sunlight that reaches the surface of the Earth is indirect (this is the light observed on a cloudy day for example). Certain applications such as concentrator photovoltaics (CPV) utilize only the direct part of the sunlight, whereas others such as flat rooftop solar panels utilize both the direct and the indirect light. Therefore the characters G and D are sometimes added to the AM1.5 spectrum to indicate whether the diffuse component is included (global, G) or not (direct, D), both spectra are also shown in figure 2.1.

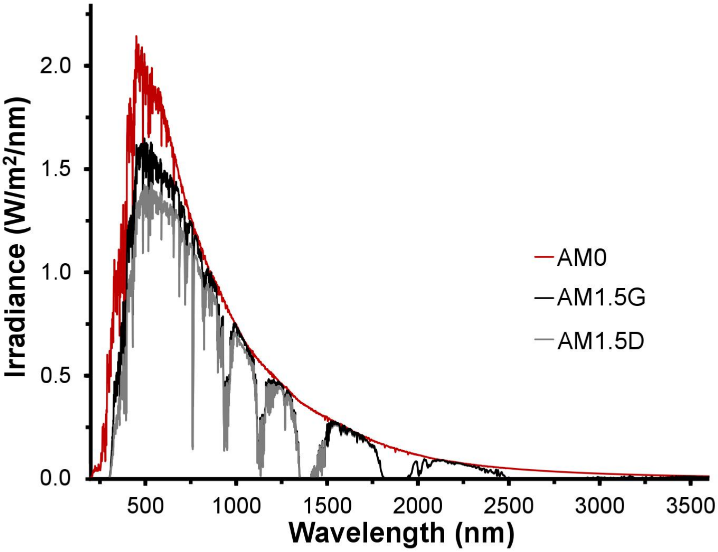

Figure 2.1: The AM0 (red), AM1.5G (black) and AM1.5D (gray) reference spectra for solar irradiation.

2.2 Semiconductors

Semiconductors are a class of materials with unique opto-electronic properties resulting from their electronic structure, which consists of a number of bands of allowed electron energies. For a pure semiconductor at low temperature all energy states in one of these bands (valence band) are occupied, while the next band of allowed energies (conduction band) is completely empty. These two bands are separated by a zone without any allowed energy levels, the so called band gap E_g. Plotted as a function of crystal momentum these bands typically have a parabolic shape. If the maximum energy of the valence band (E_v) and the minimum energy of the conduction band (E_c) are at the same value of crystal momentum the band gap is referred to as direct, and if they are at different values the band gap is indirect. Upon absorption of a photon with an energy $E_{ph} \geq E_g$, an electron can be excited from the valance band to the conduction band.

Both energy and momentum have to be conserved during this transition which requires that, in case of an indirect band gap material, the absorption of a photon is accompanied by emission or absorption of a phonon. One of the implications of this phonon assisted absorption process is the significantly larger absorption depth of indirect band gap semiconductors, which means that a much thicker layer (up to 100 times thicker) of semiconductor material is required to absorb all photons with energies $E_{ph} \geq E_g$. Once excited, an electron can now move freely between the empty energy states in the conduction band, while the electrons in the valence band can move to the empty state leaving behind a new empty state. These empty states in the valence band are generally treated as particles, referred to as holes, that have a positive charge and can move freely through the valence band.

The density of electrons and holes in the valence and conduction bands (and hence the conductivity) can be controlled by a process called doping. During this process specific foreign elements (dopants) are introduced in the semiconductor crystal lattice that either have additional or less binding electrons compared to the atoms they replace. In the case of doping with additional electrons the electrons will fill states in the conduction band, which results in n-type doping. In the case of doping with an element with less electrons some states in the valence band will remain empty, effectively creating holes and thus resulting in p-type material.

The electron and hole mobilities (μ_n and μ_p respectively) describe how easily these charged particles can move in the semiconductor material. The carrier mobility is directly affected by temperature and doping concentration [17]. The electron and hole diffusion coefficient, represented by D_n and D_p, respectively, are related to the carrier mobility by:

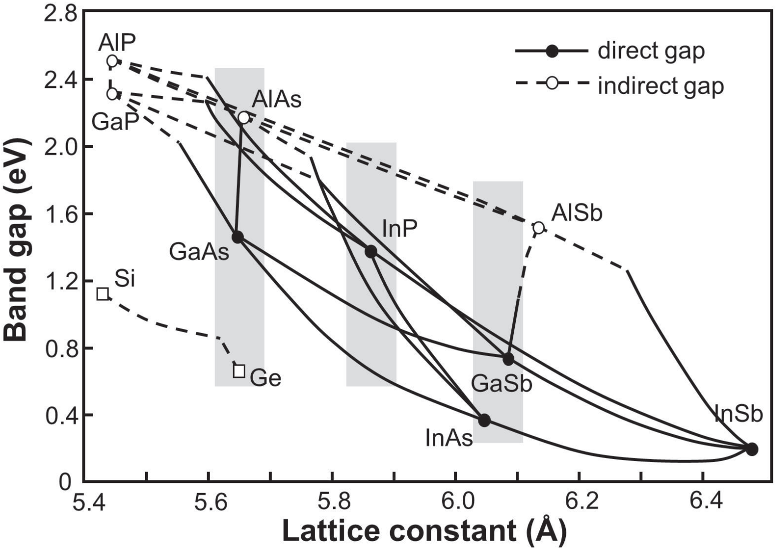

Figure 2.2: Semiconductor band gaps as a function of their lattice constant. Direct band gaps are indicated with solid lines and filled markers, while open markers and dashed lines indicate indirect bandgaps. The gray boxes indicate the range of materials that can be grown on Ge or GaAs, InP and GaSb substrates.

$$D_{p(n)} = \mu_{p(n)} \frac{k\mathrm{T}}{q}, \tag{2.3}$$

where k is the Boltzmann constant, T is the temperature and q is the elemental charge.

III-V semiconductors are materials consisting of a one-to-one ratio of elements from groups three (B, Al, Ga, In) and five (N, P, As, Sb) of the periodic table. The main advantage of these semiconductors is that, by changing the fraction of each element, many material properties can be tuned, and complex materials with a range of band gaps and lattice constants can be fabricated, as shown in figure 2.2.

Materials with similar lattice constants can be epitaxially grown on templates, usually commercially available 300-600 μm thick wafers of single or binary materials, or group IV semiconductors such as Si and Ge substrate. A few commonly used template wafers and materials that can be epitaxially grown on top of them are highlighted in figure 2.2. Another advantage of III-V semiconductor materials is that elements like zinc, carbon, silicon and tellurium can be easily added during the growth, resulting in highly controllable p- and n- type doping levels.

2.3 Solar cells

Typical semiconductor solar cells are based on a $p-n$ junction diode (see figure 2.3). When n- and p-type material are brought into contact, the concentration difference in electrons and holes at both sides of the $p-n$ junction causes free electrons to diffuse from the n-type material into the p-type, while holes diffuse in the opposite direction. Upon passing the $p-n$ junction the electrons recombine with the holes on the p-type side (and the holes with the free electrons on the n-type side). Therefore a zone of charged dopant ions (positively charged donors in the n-type material and negatively charged acceptors in the p-type material) remains near the $p-n$ junction. This zone is referred to as the depletion region (or space charge region, SCR) as it is effectively depleted of free electrons and holes. These immobile charged dopant atoms induce an electric field E across the $p-n$ junction. As a result of this electric field, holes will drift across the junction from the n-type side to the p-type side and free electrons from the p-type side to the n-type side. At thermal equilibrium conditions (e.g. in the dark) these diffusion and drift effects balance each other.

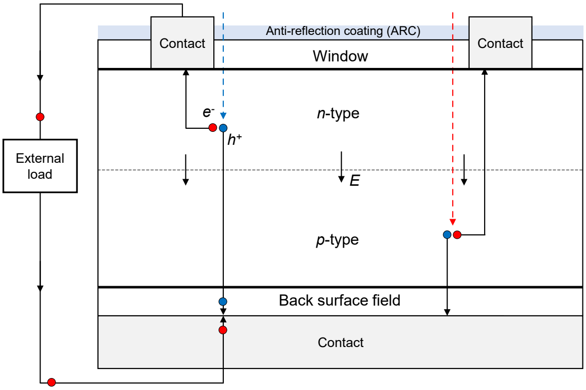

Figure 2.3: Schematic representation of a $p-n$ junction solar cell and its operation principle. Absorption of light creates electron-hole pairs, ideally the electrons reach the n-type front contact and the holes the p-type back contact. After passing through the external load the electrons recombine with holes at the back contact.

Upon illumination, the absorption of light creates additional free electron-hole pairs in the solar cell. In order to guarantee an efficient collection of light, a certain optical thickness of the solar cell is required, that is given by the wavelength dependant absorption coefficient (α) of the material. The photon flux inside the solar cell (Φ_{ph}) reduces after passing a distance x through the material, as depicted in figure 2.4 [18].

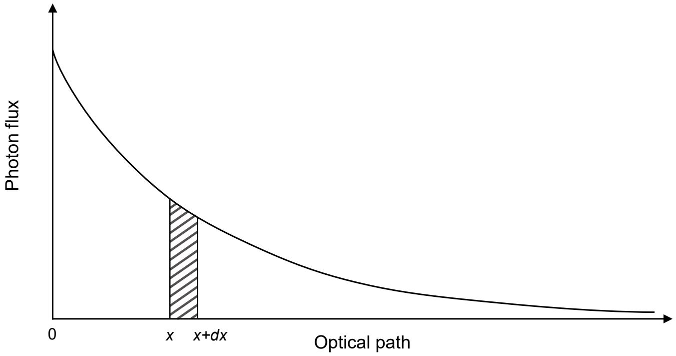

Figure 2.4: Reduction of the photon flux with increasing optical path.

The change in photon flux ($d\varPhi_{ph}(x)$) for normal incident light absorbed in a very thin layer with thickness dx at a position x is proportional to the photon flux at that position ($\varPhi_{ph}(x)$):

$$\frac{d\varPhi_{ph}(x)}{dx} = -\alpha\varPhi_{ph}(x). \tag{2.4}$$

The optical path and wavelength dependent photon flux at a point x in the solar cell is therefore expressed by:

$$\varPhi_{ph}(x,\lambda) = \varPhi_{ph}(0,\lambda)e^{-\alpha(\lambda)x}, \tag{2.5}$$

with $\varPhi_{ph}(0,\lambda)$ being the incident photon flux that is not reflected at the solar cell surface. In order to increase the incident photon flux, solar cells usually have an anti-reflection coating (ARC) applied at the top surface (represented in figure 2.3).

In the case of GaAs, which is a direct band gap material, only a few micrometers of thickness is sufficient in order to absorb virtually all the relevant incident light. Because the absorption coefficient is a function of λ, and it decreases with photon wavelength, high energy photons (blue part of the spectrum) are mostly absorbed close to the surface of the cells, while the low energy portion of light (red part of the spectrum) is absorbed further in the material.

2.3.1 Radiative and non-radiative recombination

The photo-generated carriers may recombine before reaching the electrical contacts. These recombination events are usually characterized as radiative or non-radiative. Radiative recombination is the opposite of absorption: an electron relaxes back from the conduction to the valence band, recombining with a hole, while emitting a photon with the band gap energy. The emitted photon can then be reabsorbed in the solar cell, constituting a mechanism called photon recycling. The most common non-radiative recombination mechanisms are recombination via trap levels, also known as Shockley-Read-Hall (SRH), and Auger recombination. A simplified schematic depiction of these three recombination mechanisms is represented in figure 2.5.

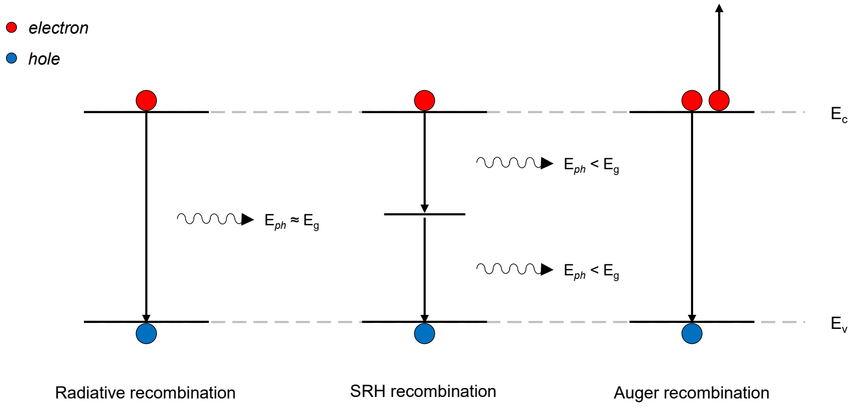

Figure 2.5: Schematic depiction of the most common types of recombination: radiative, SRH and Auger recombination.

SRH recombination is a two step process facilitated by impurities or lattice defects in the semiconductor, which introduce energy levels within the forbidden gap. The electron first relaxes to one of these trap states within the forbidden gap, partially releasing its energy by emitting a low energy photon (or multiple phonons), and then recombines with a hole from the valence band in the second step, emitting another low energy photon. These re-emited photons have $E_{ph} < E_g$, and therefore cannot be reused to excite another electron from the valence to the conduction band.

In near-perfect single-crystal materials, such as GaAs, these trap states do not exist, and are only introduced by irregularities and defects such as vacancies, ad-atoms and dislocations. Abrupt termination of the semi-conductor crystal can be seen as an extreme defect, as they typically have a large amount of interface states (created by, for example, dangling bonds) that facilitate recombination. As the density of these surface states increases, non-radiative recombination becomes more likely and the electrical performance of the entire solar cell is affected. The layer-by-layer deposition of GaAs solar cells, either by MOCVD or MBE, enables the formation of lattice-matched passivating layers on the top and bottom of the solar cell, called window and back surface field (BSF), respectively (also represented in figure 2.3). These layers have a higher bandgap than GaAs, creating an electric field that repels the carriers from surfaces, reducing the recombination rate at these regions. This process, however, does nothing to reduce surface states at the perimeter of the solar cell, which is defined by a MESA etch. Recombination at the perimeter becomes increasingly dominant at low-intensity illumination and small-area cells.

Finally, in the case of Auger recombination, an electron relaxes back to the ground state while transferring its excess energy to either another electron in the conduction band or another hole in the valence band. The excited electron or hole then loses its excess energy via phonons. This type of recombination is most important at high carrier concentrations caused by heavy doping or high level injection under concentrated sunlight, but mainly in indirect semiconductor materials, such as Si.

The minority carriers' lifetime, represented by τ_p in n-type materials and τ_n in p-type materials, is the average time between excitation and recombination of the photo-generated minority carriers. The diffusion length, determined by $L_p(n) = \sqrt{\tau_{p(n)} D}$, is the average distance the minority carriers travel during their lifetime. Recombination mechanisms directly affect the lifetime of the minority carriers, and therefore their diffusion length. For an efficient collection of the photo-generated carriers, the diffusion length must be sufficiently large so that the minority carriers can reach the depleted region and drift towards the right electrode.

2.3.2 Photon recycling

The photon emitted in a radiative recombination event can be reabsorbed, either in the active layers (emitter or base) or in the non-active layers of the solar cell, or alternatively escape through the front surface. When the emitted photon is absorbed in the active regions, it excites an electron from the valence to the conduction band, creating a new electron-hole pair. This photon is therefore considered recycled.

The spontaneous emission in a solar cell structure takes place isotropically. If the photon is emitted towards one of the interfaces and it is not absorbed before reaching it, the optical characteristics of this interface will dictate if the photon is either reflected back into the structure or lost by absorption or transmission. Figure 2.6 schematically represents the situation of an emitted photon being reflected in the top and bottom interfaces of a solar cell multiple times before being absorbed in the active layers.

Due to the large difference in refractive index between the semiconductor and air (or between semiconductor and ARC materials), the top interface reflectance (R_{top}) is usually high for incidence angles higher than the critical angle ($\approx 16°$ for GaAs). For substrate-based solar cells, the reflectance of the bottom interfaces (R_{bot}) is very

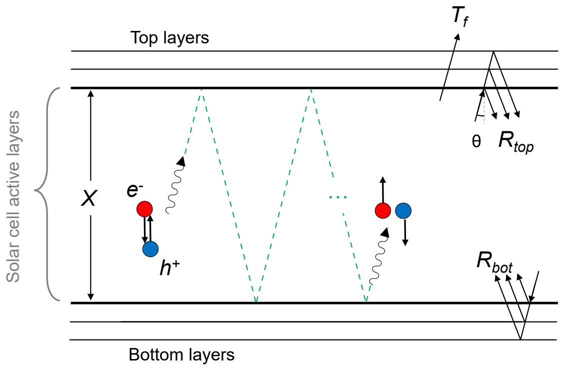

Figure 2.6: Schematic representation of a radiative recombination event taking place in the active layers of a solar cell, with the emitted photon being recycled after multiple reflections at the top and bottom interfaces. The probability of the emitted photon to be recycled is a function of the reflectance of the solar cell's interfaces (R_{top} and R_{bot}), the solar cell thickness (X) and the absorption coeficient of the material.

low, and therefore most of the photons that reach the rear layers are transmitted to the substrate where they are absorbed and lost. Genuine thin-film devices that allow for direct processing of the rear side can be equipped with layers or structures that, besides providing electrical contact, are designed to maximize the R_{bot}, which will increase the chances of photons to be recycled.

Aside from the optical interaction at the interfaces of the solar cell, the probability of a photon to be recycled is dependent of the probability that it is absorbed before reaching these interfaces. This is a function of the absorption coefficient of the material, the direction in which the photon is emitted and the device thickness. The photon recycling probability averaged for the photon energy of the material's spontaneous emission with emission angles (θ) ranging from 0 to 90°, either upwards or downwards is called the photon recycling factor (f_{PR}). In 2013, Steiner et al. [19] demonstrated that f_{PR} can be calculated by:

$$f_{PR} = 1 - \int_0^{\infty} \hat{S}(E) \int_0^{\pi/2} \frac{(1 - e^{\frac{-\alpha X}{cos\theta}})}{\alpha X} \left(1 - \frac{1}{2}(1 - e^{\frac{-\alpha X}{cos\theta}})\left(\frac{R_{top} + R_{bot} + 2R_{top}R_{bot}e^{\frac{-\alpha X}{cos\theta}}}{1 - R_{top}R_{bot}e^{\frac{-2\alpha X}{cos\theta}}}\right)\right) cos\theta sin\theta d\theta dE, \tag{2.6}$$

where $\hat{S}(E)$ represents the normalized spontaneous emission distribution of the material, α is the material's absorption coefficient and X is the sum of the emitter and base layers thicknesses (see figure 2.6). Similarly, the escape probability (f_{esc}) is the averaged probability that an emitted photon will eventually escape through the front surfaces of the cell. With T_f being the transmission at the front side of the cell, f_{esc} can be calculated by:

$$f_{esc} = \int_0^{\infty} \hat{S}(E) \int_0^{\pi/2} \frac{T_f}{2\alpha X} \frac{\left(1 - e^{\frac{-\alpha X}{cos\theta}}\right)\left(1 + R_{bot} e^{\frac{-\alpha X}{cos\theta}}\right)}{1 - R_{top} R_{bot} e^{\frac{-2\alpha X}{cos\theta}}} cos\theta sin\theta d\theta dE. \qquad (2.7)$$

A high f_{PR} increases the radiative lifetime of the minority carriers (τ_{rad}), which affects their total lifetime by [20]:

$$\frac{1}{\tau_{p(n)}} = \frac{1 - f_{PR}}{\tau_{p(n),rad}} + \frac{1}{\tau_{p(n),SRH}}, \qquad (2.8)$$

whith τ_{SRH} being the Shockley-Read-Hall recombination lifetimes. In high quality materials, such as GaAs, SRH recombination events are scarce, so that radiative recombination is the main loss mechanism in the solar cells. Therefore, cell design strategies to ensure a high f_{PR} in the device can be used to further increase the solar cell performances.

2.3.3 Solar cell operation and basic solar cell characterization

The electrical behavior of a solar cell under bias voltage V can be schematically described by the equivalent circuit diagram displayed in figure 2.7. The model includes a current source that generates the light induced current, I_L, and two diodes in parallel with different bias dependence, a series resistance R_s (ideally 0) and a parallel shunt resistance R_{sh} (ideally ∞). From a complex set of semiconductor equations an equation for the electrical behavior of a solar cell can be derived:

$$I = I_L - I_{01}\left(e^{\frac{q(V+IR_s)}{1kT}} - 1\right) + I_{02}\left(e^{\frac{q(V+IR_s)}{2kT}} - 1\right) - \frac{q(V + IR_s)}{R_{sh}} \qquad (2.9)$$

in which I_{01} and I_{02} represent the dark saturation currents through the diodes with ideality factors $n = 1$ and $n = 2$, respectively. For the sake of simplicity, the resistance effects are often neglected, setting R_s and R_{sh} to their ideal values of 0 and ∞. The two diode terms can also be combined, resulting in the simplified version of equation 2.9:

$$I = I_L - I_{0n}\left(e^{\frac{q(V+IR_s)}{nkT}}\right), \qquad (2.10)$$

where n is the device's ideality factor, ranging from 1 to 2. Furthermore, the current density J is commonly evaluated instead of the current I, as this allows for easy comparisons between solar cells of different sizes.

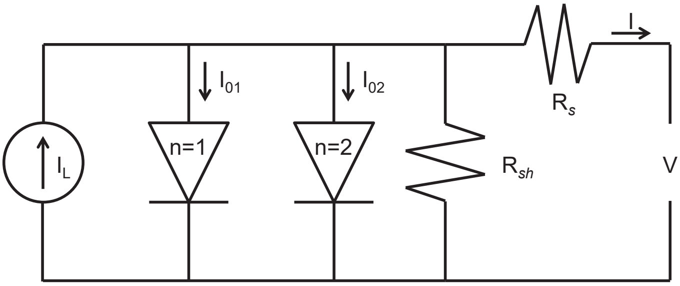

Figure 2.7: Schematic representation of the solar cell operation according to the two-diode model. The solar cell is depicted as a current source generating I_L, with two diodes in parallel. The model also includes parasitic series resistance R$_s$ (ideally 0) and parallel resistances R$_{sh}$ (ideally ∞).

An example of a typical illuminated $I-V$ curve is displayed in figure 2.8a. From this curve a number of important solar cell parameters can be obtained:

- Short-circuit current (I_{sc}): maximum current generated by a solar cell, which occurs when the voltage across the device is zero. I_{sc} is directly proportional to the available sunlight. Ideally, $I_{sc} = I_L$.
- Open circuit voltage (V_{oc}): the voltage at zero current. At I = 0, equation 2.10 can be written as:
$$V_{oc} = \frac{nkT}{q} ln\left(\frac{I_L}{I_{0n}} + 1\right), \tag{2.11}$$
- Maximum power point (MPP): the location on the $I-V$ curve where the output power P of the solar cell is at a maximum.
- Fill factor (FF): a measure for the squareness of the $I-V$ curve, given by:
$$FF = \frac{V_{mp}I_{mp}}{V_{oc}I_{sc}} \tag{2.12}$$
in which V_{mp} and I_{mp} are the voltage and current at the maximum power point (MPP).
- Efficiency (η): a measure for how much of the input power P$_{in}$ of the sunlight can maximally be converted into electricity. As the maximum output power is

obtained at the MPP, the efficiency is given by:

$$\eta = \frac{P_{mp}}{P_{in}} \times 100\% = \frac{V_{mp} I_{mp}}{P_{in}} \times 100\% = \frac{V_{oc} I_{sc} FF}{P_{in}} \times 100\%. \tag{2.13}$$

The shape of the $I-V$ curve can be affected by the presence of parasitic resistance effects in the solar cell, resulting in most cases in the reduction of the FF. The performance and efficiency of a cell are therefore reduced, as power is dissipated in the resistances. Low shunt resistance R_{sh} offers an alternate current path in the cell that reduces the amount of current extracted from the solar cell, and is typically caused by imperfections introduced during cell processing. On the other hand R_s is largely dependent on cell design and can be identified as the combination of three main resistances: the lateral resistance to the movement of current through the emitter and base towards the metal contact, contact resistances between the semiconductor and the metal, and the resistance of the metal contacts themselves.

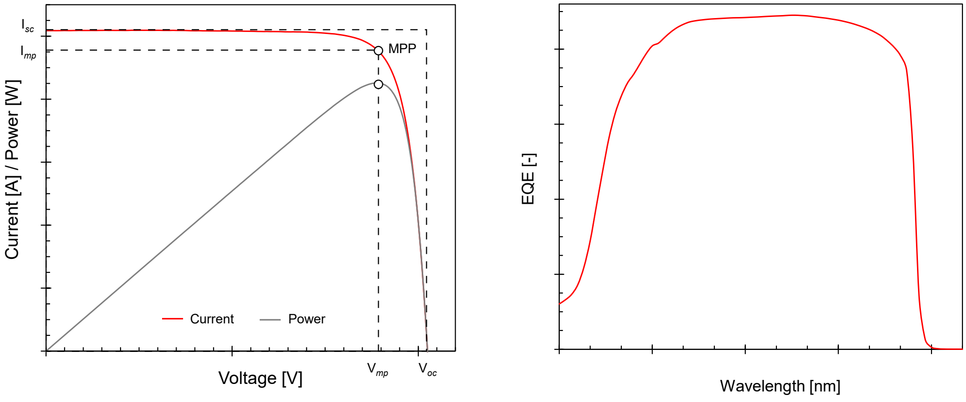

(a) **(b)**

Figure 2.8: Example of a) a typical illuminated current-voltage ($I-V$) and power output curves and b) a typical external quantum efficiency (EQE) curve.

Finally, the wavelength dependent solar cell performance can be deduced from quantum efficiency measurements. The external quantum efficiency (EQE) is defined as the charge collection rate of the generated free electrons at a wavelength λ divided by the incident photon flux Φ_{ph} at that wavelength:

$$\mathrm{EQE}(\lambda) = \frac{I_{sc}(\lambda)}{\Phi_{ph}(\lambda)} \;. \tag{2.14}$$

A typical EQE curve is depicted in figure 2.8b). By integrating the EQE over all wavelengths λ in the solar spectrum, I_{sc} can be calculated:

$$I_{sc} = \int_{\lambda} \mathrm{EQE}\,(\lambda)\,\Phi_{ph}\,(\lambda)\,\mathrm{d}\lambda\ . \tag{2.15}$$

The photon flux that is actually absorbed in the solar cell is lower than the photon flux incident on the solar cells surface, as the grid partially covers the front surface (shadowing losses) and the reflection of certain wavelengths from the surface (reflectance losses). Aside from the ARC, the front grid coverage also needs to be optimized in order to reduce shadowing losses as much as possible without increasing the series resistances. The internal quantum efficiency (IQE) is a measure for the generated free electron flux compared to the absorbed photon flux and it can be obtained from the EQE upon correction for shadowing and reflectance losses.

The dark characteristics of the solar cells (with $I_L = 0$) can be applied to retrieve information about the recombination mechanisms taking place in the structures. The cell dark curve with neglected resistance effects is generally comprised of a $1kT$ component, referent to the bias dependence of the n=1 portion of the curve, and a $2kT$ component, referent to the bias dependence of the n=2 portion of the curve. A typical solar cell dark curve is shown in figure 2.9, with the $1kT$ and $2kT$ components indicated.

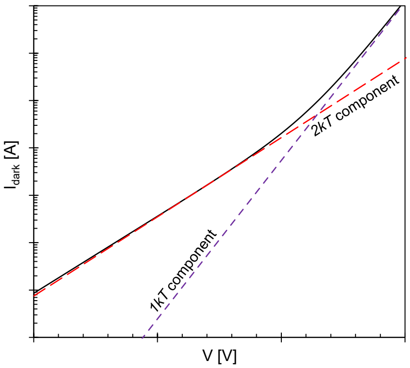

Figure 2.9: Example of a typical dark current-voltage ($I - V$) curve of a solar cell (solid black line), with the $1kT$ (dashed purple line) and $2kT$ (dashed red line) components indicated.

At lower voltages, I_{02}, representing the non-radiative recombination that takes place predominantely in the space charge region and the perimeter of the cell, dominates the dark current. At higher voltages, on the other hand, the dark curve is dominated by I_{01}, which represents the diffusion and radiative recombination currents at the quasi-neutral regions.

Chapter 3

Experimental techniques

3.1 Metal-Organic Chemical Vapor Deposition

The III-V solar cell structures described in this thesis are all grown by Metal-Organic Chemical Vapor Deposition (MOCVD), also known as Metal-Organic Vapor-Phase Epitaxy (MOVPE). Using this technique that was first described in 1968 by Manasevit [21], metal-organic and hydride source gases in a carrier gas are led over a crystalline growth substrate at high temperature in order to deposit semiconductor layers. MOCVD allows for lattice-matched (to the substrate) semiconductor growth, with monolayer sharp interfaces between different materials.

Figure 3.1 shows an Aixtron 200 low pressure MOCVD reactor, used at the Applied Materials Science (AMS) department of Radboud University for the growth of the solar cell structures. For the group III elements trimethyl-Aluminum (TMA, $Al(CH_3)_3$), trimethyl-Gallium (TMG, $Ga(CH_3)_3$) and trimethyl-Indium (TMI, $In(CH_3)_3$) are used as source gasses and for the group V elements Phosphine (PH_3) and Arsine (AsH_3) are used as source gasses. Disilane (Si_2H_6) and diethyltellurium ($Te(C_2H_5)_2$) are used for *n*-type doping and diethyl-zinc ($Zn(C_2H_5)_2$) and carbon (C) (auto-doping with the C from the methyl groups) are used for *p*-type doping. Chemical reactions occur as a result of the high temperature in the reactor, for example

$$\mathrm{Ga(CH_3)_3 + AsH_3 \longrightarrow GaAs + 3CH_4}$$

for the formation of solid GaAs, or

$$\mathrm{xIn(CH_3)_3 + (1-x)Ga(CH_3)_3 + PH_3 \longrightarrow In_xGa_{1-x}P + 3CH_4},$$

with 0≤ x≤ 1 for the formation of solid InGaP. Typical growth rates are in the order of 1 to 2 μm per hour. The required substrate temperatures are in the 600 to 750 °C range and are achieved by using infrared light to heat the graphite susceptor that holds the substrate. Layers grown with MOCVD can be grown lattice matched to the specific substrate used (typically GaAs, Ge or InP), depending on the applied gas composition. As long as the compound material has a lattice constant that does not differ too much from that of the substrate, an excellent single crystal structure can be obtained.

Figure 3.1: The Aixtron 200 MOCVD reactor used for the growth of III-V solar cell structures at the AMS department.

3.2 Solar cell processing

3.2.1 Substrate-based solar cells

A schematic depiction of a typical MOCVD grown solar cell structure is shown in figure 3.2a. The solar cell active layers are the *n*-type emitter and the *p*-type base layers, with thicknesses and doping concentrations that vary depending on the specific design of the solar cell. Lattice-matched window and BSF layers are grown on top and bottom of the emitter and base. The top most layer consists of highly doped *n*-GaAs contact layer, which allows a low series resistance Ohmic contact, without the need for annealing the metal contacts.

After deposition of the layers, the surface of the cell structures is thoroughly cleaned, typically using 2 x 30 s in acetone in ultrasonic bath, 6 x 30 s in water in ultrasonic bath, 1 x 30 s in a 1:1 H_2O:HCl (37%) solution in order to remove the oxide layer, 6 x 30 s in water in ultrasonic bath and 2 x 30 s in isopropanol. A metal front contact grid pattern is then defined by photo-lithography, which can be tuned for the solar cell's specific need. Front contacts with higher coverages are more easily probed, but generate more shadowing losses. For most of the solar cells described in this thesis, the initial layer of both the front and back contact consist of 100 to 200 nm e-beam evaporated Au. Subsequently, thicker electroplated layers of other metals (e.g. Cu) might be applied to minimize R_s.

The individual cells are created by a MESA etch, in which the epi-layers around the solar cell are etched away. The window layer (usually AlInP) is removed with a 37% HCl solution and the GaAs layers are removed with an NH_4OH:H_2O_2:H_2O solution. The GaAs contact layer between the grid fingers is also removed with an NH_4OH:H_2O_2:H_2O solution. A schematic depiction of a fully processed substrate-based solar cell with gold contacts is presented in figure 3.2b. Finally, a ZnS/MgF_2 anti-reflection coating (ARC) (typically with thickness of 44/94 nm for GaAs solar cells) can be applied by thermal evaporation to the top surfaces of the cells.

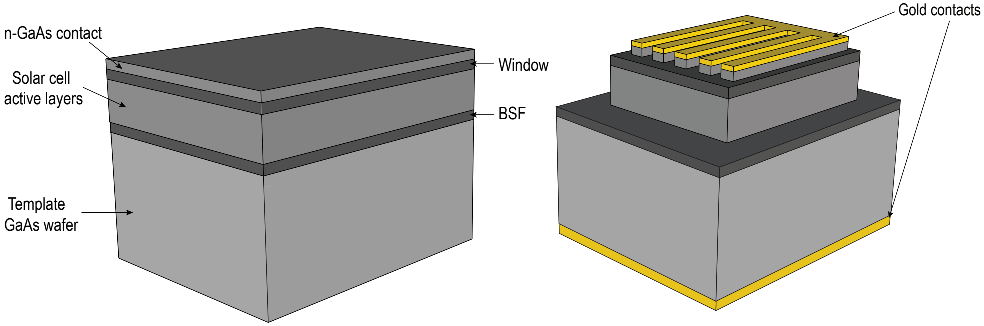

(a) **(b)**

Figure 3.2: Schematic depiction of a) the structure of a solar cell after deposition of the epitaxial layers and b) of the final device after processing into a substrate-based device. Images not to scale.

3.2.2 Thin-film solar cells

A schematic depiction of the most commonly used growth structure for thin-film devices is shown in figure 3.3a. In addition to the substrate-based solar cell structure, for the production of thin-film devices also a *p*-GaAs contact layer and a release and/or etch-stop layer must be grown before the BSF. For the studies reported in this thesis, the wafer is removed from the solar cell structures by chemical etching with an aqueous citric acid (50% by mass) and hydrogen peroxide solution (5:1 in volume), instead of using the more elaborative epitaxial lift-of method [22–32]. Therefore, the etch-stop layer consists only of a 100-150 nm thick AlInGaP layer, which is selective to the citric acid-hydrogen peroxide solution.

In order to control the fragile thin-film single crystal structures, after the cleaning of the wafer, the front surface of the solar cell structures is initially bonded to an etch-resistant temporary plastic carrier. After the removal of the wafer, the etch-stop layer is removed in a 37% HCl solution and the back contact is deposited by e-beam evaporation, usually consisting of a 200 nm Au layer. A thick Cu layer is then electroplated to the back of the structure, acting as a conductive stable carrier to the solar cells. Once the thin-film structure has a stable carrier applied to the back, the temporary plastic carrier can be removed from the front surface and the front contact grid is defined by photo-lithography.

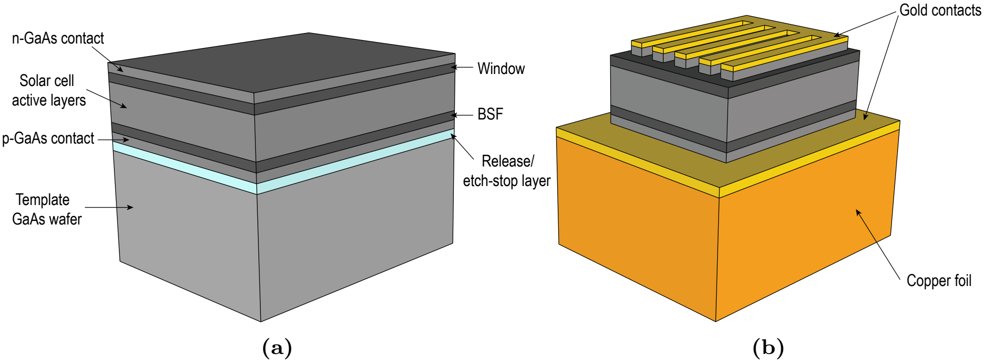

Figure 3.3: Schematic depiction of a) the structure of a solar cell after deposition of the epitaxial layers and b) of the final device after processing into an actual thin-film device. Images not to scale.

Similarly to the substrate based design, the n-contact layer is removed in between the metal contact areas using an NH_4OH: H_2O_2:H_2O solution and the solar cells are defined by a MESA etch, using a HBr:Br_2:H_2O solution for phosphide layers and an NH_4OH:H_2O_2:H_2O solution for GaAs layers. A schematic depiction of a fully processed thin-film solar cell is shown in figure 3.3b. Finally, an anti-reflection coating can also be deposited by thermal evaporation to the front surface of the cells.

Alternatively, the cell structure can be grown in the inverted direction, which simplifies the solar cell fabrication, since the structures don't need to be protected and mounted to a temporary plastic carrier. The interface quality of cells grown in this manner, however, is not yet optimized, and typically the resultant cells' efficiencies are lower. Therefore, all solar cells studied in this thesis are grown as shown in figure 3.3a.

3.3 Characterization methods

Current voltage characteristics:

Current-voltage ($I - V$) characterization of the solar cells (both in the dark and under illumination) is performed at the AMS department using an ABET Technologies Sun 2000 Class AAA solar simulator. This solar simulator provides a uniform illumination resembling the AM1.5G spectrum, over a 100 x 100 mm^2 area, with a maximum angular off set of 2°. The set-up is equipped with a Keithley 2601B source meter and data acquisition is performed using ReRa Tracer3 software. The solar cells are kept at 25 °C during measurement using a heating/cooling water thermostat and Pt100 temperature sensing.

By measuring the short current density of an NREL calibrated reference cell before each measurement series, the measured currents of the cells could be scaled to the corresponding values under exactly 1000 W/m^2. Using this approach, the cell parameters can be retrieved from the $I - V$ curves with a systematic error of ±3 mV in V_{oc}, ±0.8 mA/cm^2 in J_{sc} and ±0.005 in FF compared to an absolute reference. In mutual comparison the trends in the performance of cells as a consequence of deliberate changes in the cell geometry can be identified with an accuracy of ±2 mV in V_{oc}, ±0.06 mA/cm^2 in J_{sc} and ±0.003 in FF.

In the studies reported in chapter 6, a mobile set-up consisting of a Keithley 2401 multi-meter with a portable solar simulator was used for illuminated $I - V$ characterization. In this system, also an NREL calibrated GaAs reference cell is used for correction of the light intensity, which grants this characterization a similar measurement accuracy.

External quantum efficiency:

External Quantum Efficiency (EQE) measurements are performed with a ReRa SpeQuest Quantum Effciency system. The system uses both a Xenon and Halogen light source to address all wavelengths present in the solar spectrum. A monochromator is used to generate quasi-monochromatic light and a chopper for intensity modulation. This generates a test light of variable wavelength while a continuous bias light and bias voltage is used to put the cell under test in operating conditions. A calibration with a Silicon photodiode is made before the wavelength dependent short circuit current measurement of the solar cell.

Electroluminescence:

The electroluminescence analysis reverses the working mechanisms of the solar cell, making it act as a light emitting diode (LED), by applying a current so that the material radiatively recombines. Because radiative emissions are isotropic, imaging analysis can be only qualitative, but may provide important information with regards to the radiative emissions of the solar cell. Reduced overall luminescence or localized dark spots may indicate an increased non-radiative recombination rate in the cell structure.

In the used set up, two probes are connected to a power supply to provide a bias voltage (and therefore current) through the cells. A camera from which the infra-red filter is removed and with an applied filter for longer wavelengths is used to visualize the luminescence of the devices upon an applied current. For mutual comparison between solar cells to be possible, the measurements must be performed with fixed camera settings (lighting, exposure time etc.).

Reflectance measurements:

For the studies reported in this thesis, reflectance measurements are performed with a FilMetrics F30UVX thin-film monitor system, with light source ranging from 190 to 1700 nm perpendicular to the analyzed surfaces. For a quantitative analysis of the semiconductor layers, the system is calibrated using a reference Si wafer, and the software FILMeasure 8, by FilMetrics, is used for an approximated fit of the measured samples' thicknesses. For reflectance measurements of processed thin-film devices, which have a higher reflectance of the long wavelength portion of light than Si, an in-house fabricated gold mirror is used for calibration of the system.

3.4 Space application testing

Depending on the specific mission requirements, solar cells for space applications have to operate 10 to 15 years under extreme conditions. In order to simulate some of the challenges from the environment solar cells would face in space applications, three main aspects are studied in this thesis: electron irradiation, proton irradiation and temperature-induced degradation.

Electron irradiation

The electron irradiation of the cells is performed at the Reactor Institute Delft (RID) of the Delft University of Technology, using a Van der Graaf accelerator with a 1-MeV electron flux (Φ_e) of 5x10^{11} e^-/cm^2s. The time (t) of irradiation defines the total fluence (ϕ_e) to which the cells are exposed by $\phi_e = t \times \Phi_e$. For GEO missions, the generally associated equivalent dose is of 1x10^{15} e^{-}/cm^{2}, or a total irradiation time of 33 minutes and 20 seconds.

Proton irradiation

The proton irradiation of the cells is performed at the Center of Natural Sciences and Materials Science (CSNSM) from the Paris-Sud University, using the tandem type accelerator ARAMIS [33]. The proton beam is produced in the accelerator by a Penning positive ion source generating H^{+} ions. The utilized proton flux ($\mathit{\Phi}_p$) was either 1x10^{9} or 1x10^{10} H^{+}/cm^{2}s, and similarly to electron irradiation, the total proton fluences (ϕ_p) to which the cells are exposed are defined by $\phi_p = t \times \mathit{\Phi}_p$.

Temperature-induced degradation

For temperature dependent degradation processes (such as metal diffusion into the semiconductor) an accelerated ageing testing (AAT) method can be used. Assuming that long-term operation (10+ years) at a (relatively) low temperature (max 100 °C) is equivalent to a short period of time (several hours or days) at a higher temperature (for example 200 °C). This can mathematically be described with an Arrhenius equation [34]:

$$\frac{t_{op}}{t_{acc}} = \exp\left[\frac{E_a}{k}\left(\frac{1}{\mathrm{T}_{op}} - \frac{1}{\mathrm{T}_{acc}}\right)\right], \tag{3.1}$$

in which T_{op} is the operational temperature at which the device will be used, T_{acc} is the temperature of the accelerated life test, t_{op} and t_{acc} are the operational time at T_{op} and the ALT time at T_{acc} respectively. The activation energy of the process, E_a, is considered 0.70 eV, according to the advised by the European Cooperation for Space Standardization (ECSS) standard for photovoltaic assemblies and components (ECSS-EST-20-08C) [35].

For the study presented in this thesis, a vacuum oven is used to bring the solar cells at the required T_{acc}. The oven consists of two heating mats (maximum temperature 225 °C) wrapped around a quartz cylinder inside a cylindrical vacuum chamber, equipped with a temperature sensor connected to a Shimaden SR22 temperature controller.

Chapter 4

Increased photon recycling in thin-film solar cells with patterned rear mirror[1]

Abstract

Current thin-film GaAs solar cells typically have a completely metal covered rear side that functions as back contact, rear mirror and stable carrier to the solar cell. However, the bottom contact layer, that typically remains whole in these configuration, absorbs a large amount of photons that would otherwise be reflected back into the cell structure. This work identifies and quantifies the performance limits by non-optimal rear contact reflectance in the standard configuration of thin-film GaAs solar cells and proposes a design solution. In this study we show that the total reflectance at the back of the solar cell is increased from 63.5% to 93.2% by partially etching the absorbing GaAs contact layer and applying a dielectric material in the etched regions. Both shallow junction and deep junction cells were produced, and for deep junction solar cells the patterning resulted in a more than linear increase in the open circuit voltage and a linear increase in the short circuit current, which is in good agreement with previously reported theoretical models.

---

[1] The work presented in this section is based on ”Increased performance of thin-film GaAs solar cells by rear contact/mirror patterning”, by N. Gruginskie, S.C.W. van Laar, G. Bauhuis, P. Mulder, M. van Eerden, E. Vlieg and J.J. Schermer in Thin Solid Films 660 (2018) 10-18.

4.1 Introduction

Most III-V materials used for solar cells, such as GaAs and InGaP, are semiconductors with direct bandgap and high absorption coefficients, therefore only few micrometers thick devices are required to absorb all the incident light. However, in order to obtain good quality single crystal solar cell structures, the materials have to be grown epitaxialy on top of a GaAs or Ge wafer, with thicknesses that typically vary from 100 μm to 650 μm. After the growth, the wafer is of no value for the cell performance and it can be removed from the growth structure without any detrimental effect on the efficiency.

Methods to remove the growth template wafer of GaAs solar cells, such as epitaxial lift-off (ELO), produce as final result thin-film devices that can be semitransparent or, more commonly, mounted on a metal foil that works as stable flexible handler and rear contact [22–32]. In the latter configuration, the rear contact also acts as mirror to the incident light, enabling cells to have even smaller thicknesses (of around 2μm). This thin-film geometry is superior to those of cells processed on the native wafer and have reached higher world record efficiencies [36].

It has been demonstrated that GaAs solar cells can potentially operate close the Shockley-Queisser efficiency limit [9, 37–39] mainly by optimizing the optical advantages of the thin-film geometry. These advantages hold large promises for the applicability of these devices in space applications [40], concentrating solar systems and in combination with third generation photovoltaics.

In thin film-configurations, the production costs can be reduced with wafer reuse. Another major contribution to the cost is the growth of epitaxial structures, and this can be diminished with the production of thinner devices. For ultrathin cells (with few hundred nanometers of thickness), however, not all the incident light can be absorbed and even though these devices can be rapidly grown, it requires the application of nanostructures in the front and rear side. But to date the efficiencies achieved with solar cells of a few hundred nanometers in thickness are still relatively low (below 17%) [41–44]. This indicates that the effective increase in the optical path length of the light captured by the use of gratings and nanostructures has not yet been sufficiently implemented to compensate for drastic reductions in thickness.

The standard design of GaAs solar cells consists of a thin n-doped emitter and thicker p-doped base, here called a shallow junction (SJ) solar cell. With high quality materials, however, the minority carrier diffusion length of the emitter is improved. This allows the production of deep junction (DJ) devices, with thick emitter and thin base, that are able to achieve higher performances, as they operate mainly in the radiative recombination regime at the maximum power point [45]. As the current world-record efficiency of 28.8% for a single junction thin-film GaAs solar cell was achieved in 2012 [36] and has not been surpassed to date, these cells are clearly approaching the limit in material quality. In these cases, radiative recombination becomes the dominant loss mechanism [20, 46, 47], and photon recycling has been indicated to be the most important process in order to achieve higher V_{oc} values in previous world record cells [48]. Therefore, confining reemitted photons inside the active layers of the cell becomes fundamental in order to achieve efficiencies closer to the theoretical limit [9, 19, 39, 49, 50].

In the present study we evaluate the behavior of emitted photons in the rear layers of GaAs thin-film solar cells and the role of the rear contact design on the reflectance and photon recycling. Devices with both shallow junction and deep junction configuration were produced with increased reflectance of the rear surfaces, and the effects on the cell key parameters from these changes in the rear contact layout were evaluated.

4.2 Methods

The solar cells used in this study were grown using low-pressure MOCVD on 2 inch diameter GaAs wafers with (1 0 0) 2^o off to (1 1 0) orientation. The grown cell structures are shown in figure 4.1. In this study the wafer was removed by chemical etching with an aqueous citric acid and hydrogen peroxide solution (5:1 in volume), instead of using the more elaborative epitaxial lift-of method. In order to control the fragile thin-film single crystal structures, the front surface of the solar cells were mount to a etch-resistant temporary plastic carrier. To stop the process after etching of the wafer, a thin AlInGaP etch-stop layer was grown before the solar cell structure. Subsequently, the etch-stop layer was removed in a 37% HCl solution.

Using photolithography a pattern of disk-shaped contact areas was created in the GaAs rear contact layer. In between these contact areas with diameters ranging from 260 μm to 580 μm the p-GaAs contact layer was etched away using an NH_4:H_2O_2:H_2O (1:2:10) solution, resulting in cells with four different rear surface contact area coverages (C_r) of 100%, 50%, 30% and 10%. Next, a 60 nm thick ZnS insulating layer was deposited by thermal evaporation before removal of the photoresist, so that finally the ZnS covers only the etched regions. Then a 200 nm Au layer was deposited by e-beam evaporation throughout the entire rear surface to promote ohmic contact at the contact areas and simultaneously act as a high quality reflector at the rest of the area, followed by a thick electroplated Cu layer, to facilitate handling of the sample.

The temporary plastic carrier was removed from the front surface and a 200 nm thick Au front grid contact was deposit by e-beam evaporation. For convenience during processing and cell analysis, a grid pattern with a relatively large front surface

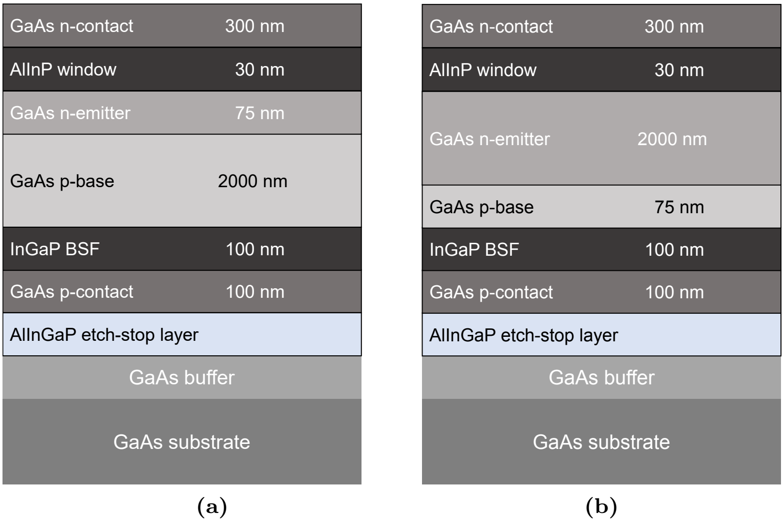

Figure 4.1: Schematic representation of the a) shallow junction (SJ) and b) deep junction (DJ) solar cells processed in this study (not to scale).

coverage (C_f) of 16.6% was applied for most cells. One or two cells in each configuration were created with a square frame-like contact pattern and without grid fingers, which is ideal for optical analysis. The *n*-contact layer was removed in between the metal contact areas using an NH_4:H_2O_2:H_2O (2:1:10) solution and the 25 mm^2 cells were defined by a mesa-etch with a HBr:Br_2:H_2O (100:1:200) solution for phosphide layers and an NH_4:H_2O_2:H_2O (1:2:10) solution for GaAs layers. Finally, an anti-reflection coating consisting of 94 nm of ZnS and 44 nm of MgF_2 was deposited by thermal evaporation. The resulting thin-film with multiple solar cells as well as a schematic depiction of the pattern applied to the contact layer are shown in figure 4.2. In contrast to the processing of wafer based cells, the processing of thin-film geometry is less well developed, but for each C_r value (i.e. from each quarter of the thin-film) 3 to 5 operating cells were obtained.

I-V characterization of the solar cells is performed using an ABET Technologies Sun 2000 Class AAA solar simulator, which provides a uniform illumination resembling the AM1.5G spectrum, over a 100 x 100 mm^2 area, with a maximum angular off set of 2^o. The setup is equipped with a Keithley 2601B source meter and data acquisition is performed using ReRa Tracer3 software. The solar cells are kept at 25^oC during measurement using a heating/cooling water thermostat and Pt100 temperature sensing.

The setup is calibrated using an NREL calibrated reference cell before each mea-

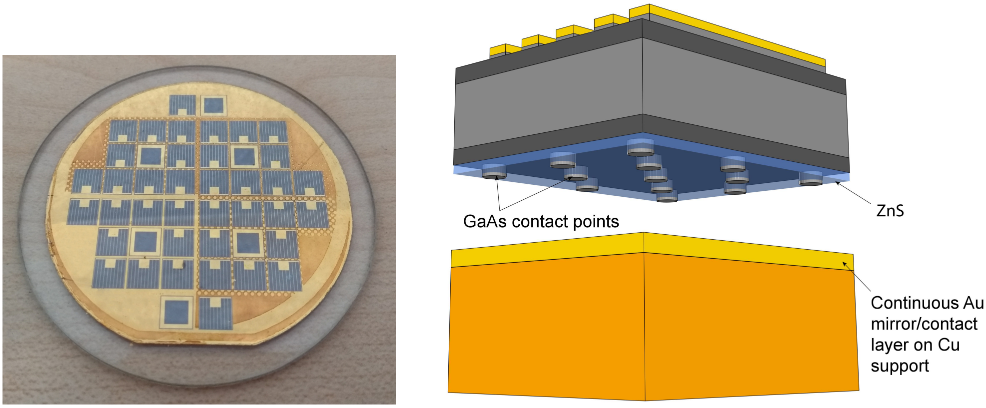

(a) (b)

Figure 4.2: a) Completely processed 2” diameter thin-film GaAs cell structure containing multiple 5x5 mm^2 solar cells with a different rear contact coverage in each quadrant. Note that each quadrant also has one or two devices with a frame-like front contact without grid fingers to facilitate optical measurements. b) Schematic representation of the rear contact pattern design (not to scale).

surement series. Using this approach the cell parameters can be retrieved from the I-V curves with a systematic error of ±3 mV in V_{oc}, ±0.8 mA/cm^2 in J_{sc} and ±0.005 in FF compared to an absolute reference. In mutual comparison the trends in the performance of cells as a consequence of deliberate changes in the cell geometry can be identified with an accuracy of ±2 mV in V_{oc}, ±0.06 mA/cm^2 in J_{sc} and ±0.003 in FF.

External Quantum Efficiency (EQE) measurements are performed with a ReRa SpeQuest Quantum Effciency system. The system uses both a Xenon and Halogen light source to address all wavelengths present in the solar spectrum. A monochromator is used to generate quasi-monochromatic light and a chopper for intensity modulation. This generates a test light of variable wavelength while a continuous bias light and bias voltage is used to put the cell under test in operating conditions.

The reflectance calculations were made using the transfer matrix method considering only normal incidence of photons. The required n and k values for GaAs and Au were retrieved from the SOPRA database [51]. For ZnS, MgF$_2$ and InGaP these data were retrieved from elipsometry analyses of test samples (typically 100 nm of the material on a GaAs substrate) that were prepared under the same conditions as the corresponding layers in our solar cell structures. Reflectance measurements were performed with a FilMetrics spectrophotometer perpendicular to the analyzed surfaces, using a gold mirror for calibration.

4.3 Results and Discussion

4.3.1 Photon absorption in the GaAs back contact layer

In order to create good ohmic contacts, the first and last grown layers in thin-film GaAs solar cells are usually highly doped GaAs contact layers. At the front side of the cell this layer is removed in between the grid fingers, but for the rear contact, it typically remains whole. Even though the contact layer is relatively thin (100 nm), a relevant fraction of available photons is absorbed in it. This is because photons emitted in the active layers of the cell as a result of band-to-band recombination are repeatedly reflected inside the cell structure and pass through the contact layer several times. Figure 4.3 depicts the calculated reflectance at the rear side interfaces of the thin film cell ($R_{GaAs/Au}$) considering normal incidence of photons. At room temperature, band-to-band emissions from GaAs peak at around 870 nm (the band gap wavelength), and the full-width at half maximum (FWHM) of the emission line is 28 nm. The emissions from GaAs cease at the band gap, so the reflectance should be maximized in the region between 870 nm and 840 nm [52]. At these wavelengths, the calculations show a large absorption (>30%) of generated photons, with an average reflectance of 63.5% in this region. In a structure without a GaAs contact layer, the reflectance (R_{Au}) could be increased to approximately 94%.

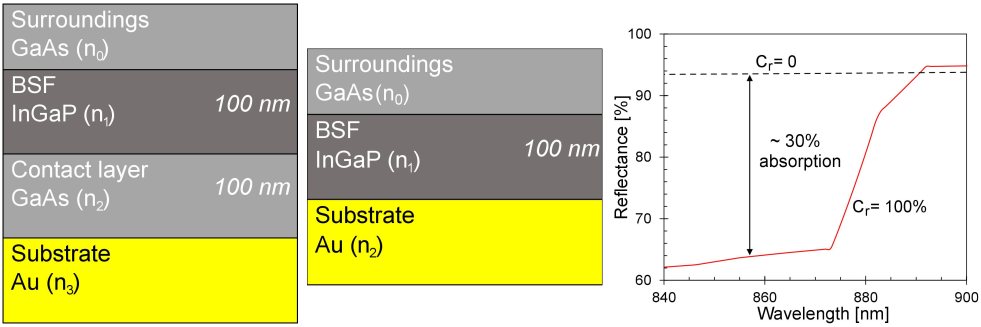

(a) (b) (c)

Figure 4.3: Relevant structure used to simulate the reflectance of photons emitted from the active GaAs layer (n_0) at the rear surface of a) a standard thin-film GaAs solar cell structure ($C_r = 100\%$), b) the same structure without the contact layer ($C_r = 0$), and c) the calculated wavelength dependent reflectance at these structures, considering normal incidence of photons.

Absorbed photons in the non-active layers of the cell are lost as they do not contribute to the cell performance. Therefore, it will be beneficial to partially remove the rear contact layer, analogous to the procedure applied at the front side. If a transparent insulator material is deposited in the areas where the contact layer is removed and Au remains deposited continuously at the rear surface, at the etched regions the Au layer will function only as a mirror. The benefit of the intermediate layer is that a certain fraction of the light is already reflected at the semiconductor-dielectric interface before reaching the gold interface that because of its higher extinction coefficient does represent some absorption losses. The thickness of the dielectric layer can be tuned in such a way that in the relevant wavelength range corresponding to the GaAs bandgap in the fraction reflected at the gold interface is minimal due to destructive interference.

The materials considered for the transparent insulator layers were ZnS and MgF_2, both with a refractive index in between that of InGaP (n=3.2) and gold (n=0.2) at the 870 nm wavelength region. Figures 4.4b) and 4.4c) show the wavelength dependent reflectance following from simulations performed using the layer structure in figure 4.4a, with the dielectric materials instead of the contact layer. The simulations show an increase in reflectance if either ZnS or MgF_2 is applied before the Au layer as compared to Au directly applied to the back surface field. According to these simulations, the use of MgF_2 will result in the highest reflectance. In practice, however, the adhesion from the thermally evaporated MgF_2 to the semiconductor material was found to be problematic, as it easily delaminates. Therefore, ZnS was the chosen material for further studies.

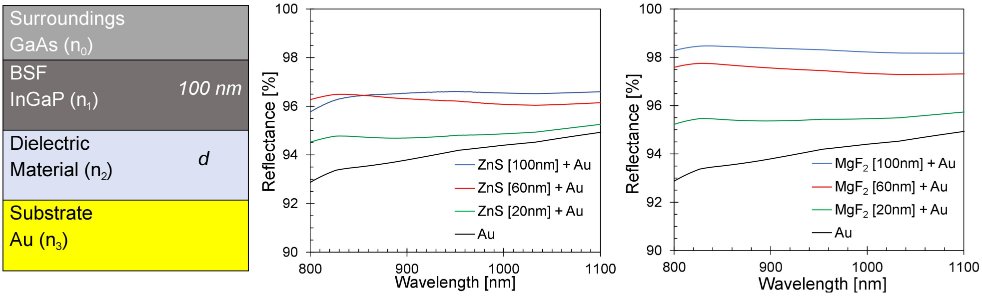

(a) **(b)** **(c)**

Figure 4.4: a) Structure used to simulate the reflectance of photons emitted from the active GaAs layer (n_0) at the rear surface of thin-film GaAs solar cells with dielectric materials replacing the normally applied GaAs contact layer, and the calculated wavelength dependent reflectance at these structures considering b)ZnS and c)MgF_2 as the dielectric materials.

In the first place the role of the rear mirror in thin-film solar cells is to reflect the incident light that is not absorbed in the first pass. This enhances overall absorption and increases the short-circuit current density (J_{sc}) or alternatively allows to reduce the active cell layer thickness without loss in J_{sc}. GaAs is a good absorbing material, and in the produced 2 μm thick solar cells most of short wavelength light is absorbed in the first pass through the active layers, and the rear mirror reflectance is particularly important for wavelengths above 700 nm. In the second place the rear mirror is important to confine photons that are emitted upon radiative carrier recombination with wavelengths between 840 nm and 870 nm, so they can be reabsorbed in the active layers of the structure. This increase in the photon recycling will result in an increase in the open circuit voltage (V_{oc}) [9,38].

Experimental measurements were made to confirm the increase in reflectance obtained by the deposition of ZnS. For this purpose, 650 μm thick GaAs wafers polished on both sides were used. An ARC optimized for longer wavelengths was deposited on the front surface and different thicknesses of ZnS ranging from 0 to 100 nm were evaporated on the rear surface, which were subsequently covered with 200 nm of Au. These structures and the obtained reflectance curves are depicted in figure 4.5. Because of the long optical path that the light has to travel in the GaAs wafer, it is not possible to measure the reflectance mechanisms in the bandgap region. However, a comparative analysis of the different interfaces can be done by observing the reflectances at slightly longer wavelengths. Even though parasitic sub-bandgap absorption in the 650 μm thick GaAs substrate cause the absolute reflectance values to be different from the simulations, at around 1050 nm both simulated and measured curves show similar patterns, confirming the increase in reflectance caused by the deposition of ZnS.

The deposition of 100 nm of ZnS would result in highest reflectance at wavelengths above the bandgap, but the calculated average reflectance between 840 nm and 870 nm (R_{ZnS}) is equal to 96.5% for both 60nm and 100nm of ZnS. For shorter wavelengths (important to avoid J_{sc} losses), however, the reflectance of 60 nm of ZnS is higher than for 100 nm. Therefore, 60 nm was the thickness of ZnS applied to the produced devices.

4.3.2 Rear contact patterning to improve the reflectance

From the previous evaluation it is clear that, compared to the p-GaAs/Au structure, the ZnS/Au structure has an improved reflectance of photons in the relevant wavelength range (840-870 nm) to the active layers cells (approximately 63.5% compared to 96.5%). Therefore the reflectance at the rear side of thin-film GaAs solar cells can be improved by reducing C_r and with the application of an intermediate ZnS

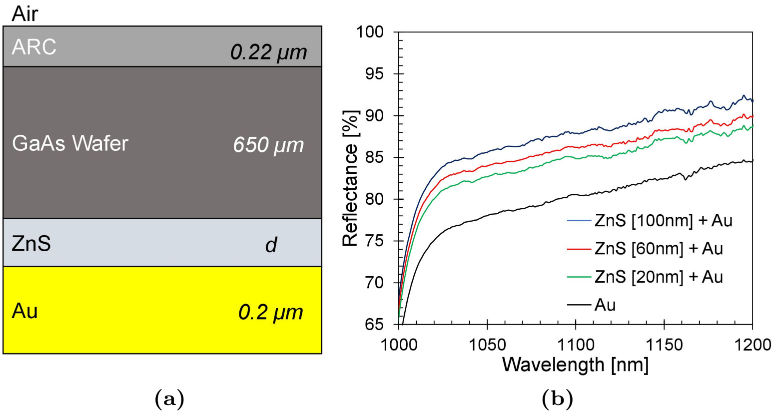

(a) **(b)**

Figure 4.5: a) Schematic depiction of the structure used for reflectance measurements and b) measured reflectance curves for samples with different thicknesses of ZnS.

layer. To evaluate this experimentally, cells with four different rear contact geometries (C_r = 100%, 50%, 30% and 10%) were produced simultaneously from a single wafer (see figure 4.2). In this way, any performance variation observed between the solar cells can unambiguously be assigned to the rear side patterning, rather than eventual small run to run differences in wafer processing. The electroluminescence images of the thin-film cells, shown in figure 4.6, clearly reflect the rear side contact geometry of the devices, as this technique injects current in the solar cells through the contacts, leading to radiative recombination in the active area. Because the current density is highest in the direct vicinity of the contact areas, these are brighter due to higher recombination rates. The obtained contact pattern is well defined and there is no apparent defect formation resulting from the patterning.

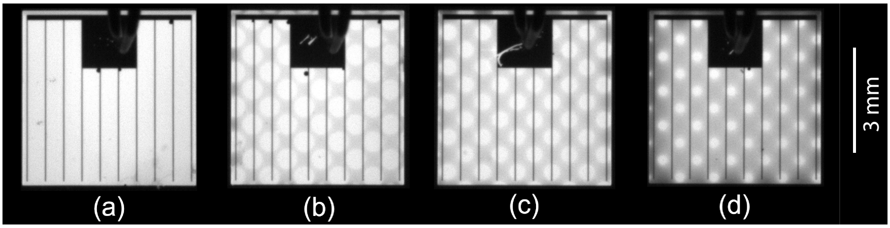

Figure 4.6: Electroluminescence images of the cells with C_r equals to a)100%, b)50%, c)30% and d)10%. The camera parameters and the applied current were kept constant for all measurements.

As first order approximation, the average rear side reflectance in the wavelength range from 840 to 870 nm of the cells with different C_r values can be determined by

$R_{cell} = C_r.R_{GaAs/Au} + (1 - C_r).R_{ZnS/Au}$. This approximation yields values of 63.5%, 80.0%, 86.6% and 93.2% for C$_r$ = 100%, 50%, 30% and 10% respectively. The total reflectance of the processed DJ cell structures without grid fingers, measured using a spectrophotometer perpendicular to the cell front surface, are shown in figure 4.7. Similar as calculated above for the photons in the 840-870 nm range, photons with wavelengths above this range show enhanced reflectance as C$_r$ is reduced and the area covered with ZnS, beneficial to the reflectance, is increased. However, the absolute value of the reflectance for these photons is higher because they do not suffer from absorption in the GaAs rear contact layer. Unfortunately, the solar cell without grid fingers with C$_r$ = 50% was damaged, and therefore there is no reflectance spectrum for this configuration.

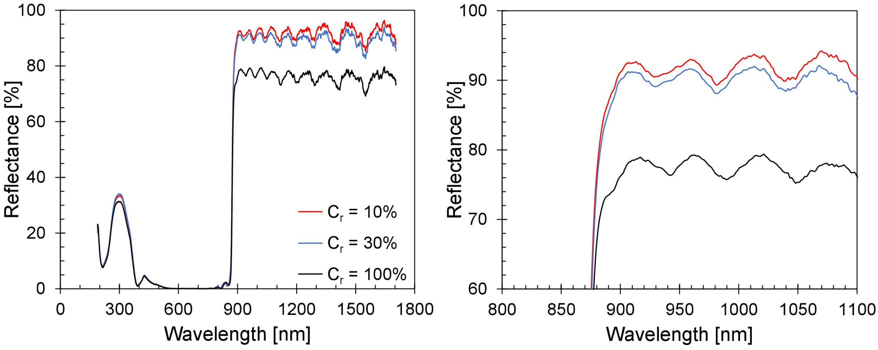

(a) **(b)**

Figure 4.7: a) Reflectance curves obtained from the front surface of fully processed DJ solar cells without front grid fingers. b) Detail of the reflectance around the bandgap wavelength.

The illuminated IV parameters under 1 sun conditions of the best performing cells in both the SJ and DJ set of devices with different C$_r$ values are shown in table 4.1. For the SJ devices, C$_r$ = 50% was not applied and there are no results for this geometry. In the SJ devices, the J_{sc} remained constant, but both the V_{oc} and the FF values decrease as C$_r$ decreases, and no advantages were observed with the patterning. In the DJ configuration, both J_{sc} and V_{oc} increase for lower C$_r$ values. The FF of the cells essentially stays constant only to drop suddenly by more than 3% for C$_r$ = 10%, most probably by an increase in series resistances related to the strongly reduced rear contact area. In these samples, the thick and continuous rear contact reduces metal contact resistances to a negligible value, indicating that the main loss mechanism is the lateral resistance that carriers encounter from the position they are generated to the contact points. An optimized design with more evenly dispersed smaller contact points for the rear contact is expected to reduce the fill factor losses considerably, thus allowing for the production of devices with even lower C$_r$.

Table 4.1: Illuminated IV parameters of both SJ and DJ solar cells with different rear surface contact fractions.

	SJ devices			DJ devices		
	J_{sc}	V_{oc}	FF	J_{sc}	V_{oc}	FF
C$_r$ [%]	±0.06 [$\frac{mA}{cm^2}$]	±2 [mV]	±0.3 [%]	±0.06 [$\frac{mA}{cm^2}$]	±2 [mV]	±0.3 [%]
100	24.17	1006	85.0	24.34	1050	85.8
50	–	–	–	24.23	1053	85.6
30	24.14	1000	84.4	24.43	1055	85.5
10	24.15	0992	83.6	24.46	1058	82.1

The differences in performances between SJ and DJ devices are explained with the analysis of the dark curve. The diode recombination current density is described by [48]:

$$J_{rec} = J_{01}\left(e^{\frac{qV}{kT}} - 1\right) + J_{02}\left(e^{\frac{qV}{2kT}} - 1\right) \tag{4.1}$$

with $n = 1$ the radiative and n=2 the non-radiative recombination ideality factors. The non-radiative recombination is known to predominantly take place in the depletion zone and the perimeter of the cell, while the radiative recombination is dominant in the neutral regions of the cell. For DJ cells at operating voltage, the contribution of non-radiative recombination is lower than for SJ cells [45]. The ratio between the recombination currents is voltage dependent, with non-radiative recombination dominating J_{rec} at low voltages and radiative recombination at higher voltages. In the analysis of the dark current at lower voltages of the produced samples with C$_r$ = 100% we find that the non-radiative saturation current density (J_{02}) is one order of magnitude higher for the SJ devices ($3x10^{-11}A/cm^2$) compared to the DJ geometry ($4.8x10^{-12}A/cm^2$). At the operating voltage, J_{rec} of the SJ cell is therefore mostly non-radiative and consequently the application of an improved geometry for photon recycling in these cells has no noticeable effect on the cell performance.

A $J_{sc} - V_{oc}$ curve composed of data points of I-V curves measured under different light intensities represents the ideal diode dark characteristics, as the series resistance is excluded under these conditions [53]. At higher voltages (the n = 1 region) it is possible to determine the radiative saturation current density (J_{01}), and these results are shown in figure 4.8. For the produced DJ cells, with the decrease of C$_r$ (and the increase in reflectance) the J_{01} values also decrease. This irrefutably shows an improvement in re-absorbtion of emitted photons generated by band-to-band recombination [20, 45].

The external quantum efficiencies (EQE) of these devices, shown in figure 4.9, confirm that the mild increase in the J_{sc} in the DJ devices is due to the increased

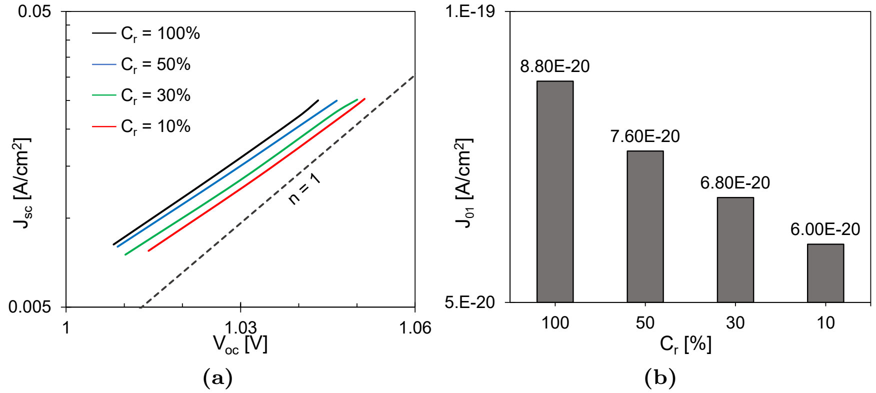

(a) **(b)**

Figure 4.8: a)$J_{sc} - V_{oc}$ curves measured at different light intensities of the DJ devices with different C$_r$ and b) the calculated J_{01} of each device.

reflectance of the incident light. Most of the incident light with shorter wavelengths is absorbed before reaching the rear layers and no differences in the spectrum are expected in this region, but for wavelengths above 700 nm, the EQE of the cells clearly increases.

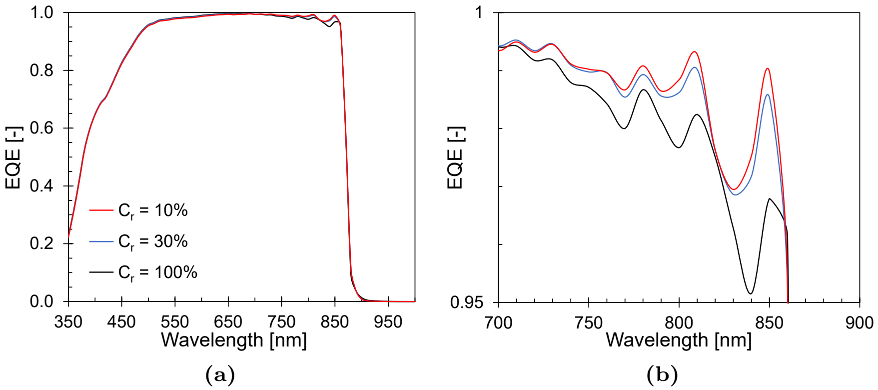

(a) **(b)**

Figure 4.9: a) External quantum efficiency of the DJ samples with different C$_r$. b) Detail of the curve at the longer wavelength region.

Miller et al. [9] have modeled the effect that the rear mirror reflectance has on the cell parameters of a 3 μm thick GaAs solar cell in the absence of non-radiative recombination. The model predicts a more than linear increase in V_{oc} and a linear increase in J_{sc} as the reflectance approaches 90%. In order to facilitate the comparison between the results from the model and those from solar cells produced in this study, the earlier approximated R_{cell} value for each configuration is related to its V_{oc} and J_{sc} in figure 4.10. For easy comparison, the curves from the literature are (on a different scale) also depicted in the same graphs. The obvious differences in the absolute V_{oc} and J_{sc} values derived from the model reported in literature and the values obtained in the here reported experiments are due to the fact that the model represents a simplification of the actual situation. The model, for example, neglects the reflection of light at the ARC and grid contacts of the cell and assumes the total absence of non-radiative recombination. Nevertheless, the obtained trends for the produced cells are similar to those following from numerical simulations, providing experimental proof of concept of this relationship.

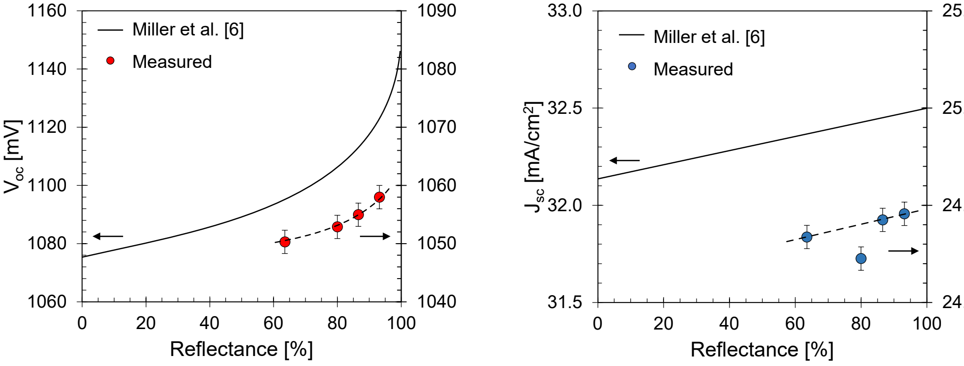

(a) **(b)**

Figure 4.10: Measured a) V_{oc} and b) J_{sc} of the DJ solar cells related to the respective average reflectance of the processed cell (R_{device}). The obtained trend in both parameters is similar to that predicted in the literature.

4.4 Conclusions

Reemitted photons by band-to-band recombination in GaAs solar cells have a wavelength that varies from 840 to 870 nm. In this region, the rear contact layer in thin-film GaAs solar cells absorbs a relevant fraction of photons, that therefore do not contribute to the solar cell performance. Both theoretical and experimental results show that compared to the use of a Au mirror directly on the BSF of the cell a further improved reflectance can be obtained by the application of an intermediate ZnS or MgF_2 layer. Based on these results an approach comprising partial removal of the *p*-GaAs contact layer and replacement by deposition of ZnS was developed and tested in both shallow junction and deep junction solar cell geometries. The calculated total reflectance at the active layers of these cells increases from 63.5% in the original structure ($C_r = 100\%$), up to 93.2% with the new design ($C_r = 10\%$).

In thin-film SJ devices the non-radiative saturation current density (J_{02}) is higher and no positive effects on the cell performance are apparent by this approach. However, with the obtained increase in reflectance, the illuminated IV parameters of DJ solar cells improve, and the radiative saturation current density (J_{01}) decreases. This demonstrates an increase in photon recycling and reaffirms the importance of the rear mirror reflectance in the design of thin-film GaAs solar cells.

The results of this study experimentally confirm previously reported theoretical calculations that relate the reflectance of the rear mirror and the solar cell parameters. Furthermore, the technique developed in this work provides a clear reduction of J_{01} without any required changes to the growth structures of the solar cell. Therefore, with further reduction of the non-radiative losses and an optimized rear and front contact geometries, patterning the rear contact represents a viable approach to achieve efficiencies closer to the theoretical limit.

Acknowledgements

The authors acknowledge financial support from the Brazilian National Council for Scientific and Technological Development, under the program Science Without Border, project 233259/2014-7, and from the European Union's Horizon 2020 research and motivation program, under grant agreement 687253 TFQD (http://tfqd.eu).

Chapter 5

Performance limiting mechanisms for photon recycling in thin-film solar cells[1]

Abstract

Photon recycling mechanisms in single junction thin-film GaAs solar cells are studied. An approach of theoretical modeling supported by experimentally obtained results is used in order to correlate the reflectance of the cell's rear layers, the photon recycling probability and the solar cell performance. Solar cells with different top and bottom metallization configurations are produced and their performance is optically and electrically analyzed. It is shown that the photon recycling probability increases with the rear mirror reflectance and solar cell thickness, which results in the increase of the devices open circuit voltage. However, the front grid coverage, usually disregarded in rear mirror focused studies, strongly reduces the photon recycling probability. Furthermore, perimeter and interface recombination obstruct the internal radiative efficiency of the solar cells, preventing further increase of the devices' open circuit voltage as a result of improvements to the rear mirror of the cells. In order to achieve a significant benefit of increased photon recycling probability to the solar cell performance, these limiting mechanisms need to be properly addressed.

---

[1] The work presented in this section is based on "Performance limiting mechanisms for photon recycling in thin-film GaAs solar cells", by N. Gruginskie, F.Capelluti, G. Bauhuis, P. Mulder, E. Vlieg and J.J. Schermer. *In preparation.*

5.1 Introduction

In the last decade, thin-film single junction GaAs solar cells have surpassed the performance of similar structures processed on the growth substrate, and their world record efficiencies presented an absolute increase of 3% [4,8]. When comparing single junction GaAs solar cells in the thin-film or wafer-based designs, the advantages of the wafer-based architecture are mainly the more mature and quick processing route. The thin-film architecture presents as main advantages the reduced weight and potential of reduced costs with the removal and reuse of the wafer [25, 29, 54], possibility of utilizing thinner epilayers with the application of a back reflector that increases the light optical path [26, 40, 55]; increased resilience to particle irradiation for space application due to the reduced thickness [56,57], bendability [31,58–60] and increased photon recycling due to reflectance of emitted photons [9,19,20,50,61].

In 2012, Miller et al. [9] showed that, with the application of a high quality back reflector, thin-film GaAs solar cells have the potential to reach efficiencies close to the theoretical limit. In the same study, it was shown that the rear reflectance has a direct impact on the solar cell parameters, most drastically affecting the open circuit voltage (V_{oc}), due to a more efficient re-absorption of radiatively emitted photons. Since then, multiple studies have been conducted towards increasing photon recycling in thin-film solar cells, most of which present high quality crystal structures and efficiencies close to 25% [19,50,57,61–66]. The main direction is to increase the reflectance at the rear side, generally resulting in an increase of the devices' V_{oc}. In most of these studies, however, the achieved V_{oc} values are well below the expected, often not surpassing 1080 mV.

Initially reported thin-film III-V solar cells typically had highly doped GaAs rear contact layers and fully metallized rear sides [6, 8, 28, 41, 67]. However, in recent studies [61, 64] it has been demonstrated that the reflectance at the rear side of the cells can be significantly increased if the GaAs contact layers are partially removed and replaced by a suitable dielectric layer (such as ZnS) before the final rear side metallization is applied. In this approach, the locally remaining rear-contact areas guarantee a low series resistance contact of the device. The reflectance increases if the rear contact coverage (C_r) is reduced and replaced by a superior mirror structure. As a result, the photon recycling increases, showing the onset of the theoretically predicted more than linear increase in V_{oc} [9,64]. However, for $C_r = 10\%$ and below, multiple studies reported a strong decrease in the Fill Factor (FF) of the cells due to an increased lateral resistance [61,64], limiting the possibilities for further gains in efficiency with this approach.

In the present study, the technique to apply a pattern to the rear contact was further elaborated, and working devices with rear side coverage as low as 1.5% were produced. Furthermore, we identify the cause for the open circuit voltage shortfall by evaluating design strategies for photon recycling based on theoretical modeling supported by experimentally obtained results. Using this approach, we demonstrate that for high quality GaAs, it is typically the perimeter and hetero-interface recombination that obstruct the theoretically predicted increase in the open circuit voltage of the cells. If not properly addressed, these limiting mechanisms will prevent the benefits of an optimized rear contact and consequently increased photon recycling probability to be fully obtained.

5.2 Methods

In order to determine the relation between the reflectance of the rear layers of the cells, total photon recycling and device performance, an approach using model simulations combined with experimental analysis of various cell geometries is applied. Firstly, the optical performance of solar cells with different back mirror reflectances are studied and the probability of photon recycling in these cells is calculated. For that, two solar cell structures with a standard deep-junction (DJ) geometry and GaAs as contact layer are processed into thin-film cells with differently patterned rear contacts. Several aspects are optimized in a third structure, aiming to pair the model predictions with the experimental results. Subsequently, an electrical model is used in order to determine which recombination mechanisms are dominating the operation of the solar cells.

5.2.1 Experimental procedures

All solar cell structures used in this study were grown by low-pressure MOCVD on 2 inch diameter GaAs wafers with (1 0 0) 2^o off to (1 1 0) orientation. Three epi-structures, here called structures A, B and C, were grown and processed. All structures have a thick n-doped emitter (x_E = 1685 nm for A and B, and 2000 nm for C) and a thin p-doped base (x_B = 100 nm for all). Two passivating layers, a 20 nm AlInP window and a 100 nm InGaP back surface field (BSF), were grown enclosing the active layers, in order to repel the minority carriers and reduce surface recombination. The outer top and bottom layers of the devices consist of highly doped contact layers that provide low resistance ohmic contact to the metallized parts of the cell. For all structures, the top contact layer consists of 300 nm n-GaAs. For the bottom contact layer, 100 nm GaAs was applied for structures A and B, and 150 nm $\text{Al}_x\text{Ga}_{1-x}\text{As}$ was used for C, with the fraction of Al x being 0.1 for the outer 20 nm and 0.3 for the remaining 130 nm. For convenience, this material will be simply referred to as AlGaAs. An AlInGaP etch-stop layer is grown before all solar cell structures in order to stop the etching during the removal of the substrate.

For all structures, the substrate was removed with an aqueous citric acid and hydrogen peroxide solution (5:1 in volume) and the etch-stop layer was removed with HCl 37%. Using photolithography and e-beam evaporation, the rear side of the resulting 2-inch diameter thin-films were Au metallized with 4 different patterns, one for each quadrant for structures A and B, and two different patterns, one for each half of structure C. At each film, one section was fully metallized, i.e. the rear surface coverage (C_r) is 100%, while the other sections were partly metallized using a regular array of 20 μm radius disc-shaped contact points. By varying the pitch distance between the contact points, rear surface coverages between 20% and 1.5% were realized for the different segments of the thin-film samples. Subsequently, for structures A and B the rear contact layer in between the contact points was etched away using an ammonia:hydrogen peroxide solution and 60 nm of ZnS was thermally evaporated in the etched areas. For structure C, the patterning was applied and ZnS was deposited without the removal of the AlGaAs contact layer. The rear side processing of the structures was completed by evaporation of a 200 nm thick Au rear contact / mirror layer over the entire surface of all structures and application of copper foils that acts as conductive foreign carriers. Further details of this rear side processing approach are described in previous work [64].

Using e-beam evaporation, the front side of the thin films were equipped with either 200 nm (structures A and B) or 100 nm (structure C) thick Au grid contacts. Subsequently, individual cells were defined by a MESA etch using an ammonia:hydrogen peroxide solution for the GaAs layers and an $HBr:Br_2:H_2O$ solution for the phosphide layers. The cells from structure A and B are 0.5x0.5 cm^2 with a front grid coverage (C_f) of 16.6 %, and the cells from structure C are 1.0x1.0 cm^2 with C_f = 8%. For all cells, the top *n*-GaAs contact layer in between the grid fingers was removed also using an ammonia:hydrogen peroxide solution. Finally, a thermally evaporated ZnS/MgF_2 (44/94 nm) anti-reflection coating (ARC) was applied to all cells.

Illuminated and dark $J - V$ characterization of the solar cells were performed using an ABET Technologies Sun 2000 Class AAA solar simulator set-up, equipped with a Keithley 2601B source meter, and ReRa Tracer3 software for data acquisition. The solar cells were kept at 25^{o}C during measurement using a heating/cooling water thermostat and a Pt100 temperature sensor. The light intensity was set and corrected using an NREL calibrated reference cell before each measurement series. Because at higher voltages the series resistances cause the dark curve to bend downwards, a set of $J_{sc} - V_{oc}$ data points measured under different light intensities was used in the dark characteristics analysis, as the series resistance is excluded under these conditions [45]. External Quantum Efficiency (EQE) measurements were performed with a ReRa SpeQuest Quantum Effciency system. The system uses both a Xenon and Halogen light source to address all wavelengths present in the solar spectrum, a monochromator to generate quasi-monochromatic light and a chopper for intensity modulation.

The required n-k values for the theoretical analysis for ZnS, MgF_2, AlInP and InGaP were retrieved from ellipsometry analyses of test samples (typically 100 nm of the material on a GaAs substrate) that were prepared under the same conditions as the corresponding layers in our solar cell structures. Reflectance measurements were performed with a FilMetrics spectrophotometer perpendicular to the analyzed surfaces, using a gold mirror for calibration. A camera with short infra-red detection was used in order to obtain electroluminescence images of the solar cells under externally applied current. The same camera was used to capture images of the solar cells under an inclined angle to visualize the rear contact patterns (no current applied).

5.2.2 Device modeling

A combination of models reported in the literature [19, 20, 68, 69] was used in order to simulate different optical and electronic mechanisms of the solar cells. A general schematic depiction of the used solar cell structures and main parameters is shown in figure 5.1a, and the various interfaces studied are represented in figure 5.1b. The reflectances at the emitter-window (R_{top}) and at the base-BSF (R_{bot}) interfaces of different structures were calculated as a function of photon wavelength (from 300 to 1200 nm) and angle of incidence (from 0° to 90°). The optical data of the materials that were not retrieved from elipsometry measurements were taken from the literature [51, 70–72].

The probability that a photon resulting from radiative recombination is reabsorbed in the active layers of the solar cells is called the photon recycling factor (f_{PR}). In the model reported by Steiner et al. [19], f_{PR} is averaged for photons emitted spontaneously with emission angles (θ) ranging from 0 to 90°, either upwards or downwards. The model calculates the probability of these photons to reach the interfaces and then be reflected back into the solar cell structure multiple times, with the expression:

$$f_{PR} = 1 - \int_0^\infty \hat{S}(E) \int_0^{\pi/2} \frac{(1 - e^{\frac{-\alpha X}{cos\theta}})}{\alpha X} \left(1 - \frac{1}{2}(1 - e^{\frac{-\alpha X}{cos\theta}}) \left(\frac{R_{top} + R_{bot} + 2R_{top}R_{bot}e^{\frac{-\alpha X}{cos\theta}}}{1 - R_{top}R_{bot}e^{\frac{-2\alpha X}{cos\theta}}}\right)\right) cos\theta sin\theta d\theta dE, \tag{5.1}$$

where $\hat{S}(E)$ represents the normalized spontaneous emission distribution of GaAs, α is the material's absorption coefficient and X is the sum of the emitter and base layers thicknesses ($x_E + x_B$). A similar formulation is also applied to calculate the probability of a radiatively emitted photon to escape through the front surface (f_{esc}). By using the optical characteristics of all layers in the solar cell structure, this model implicitly includes the parasitic losses, such as absorption at the non-active layers.

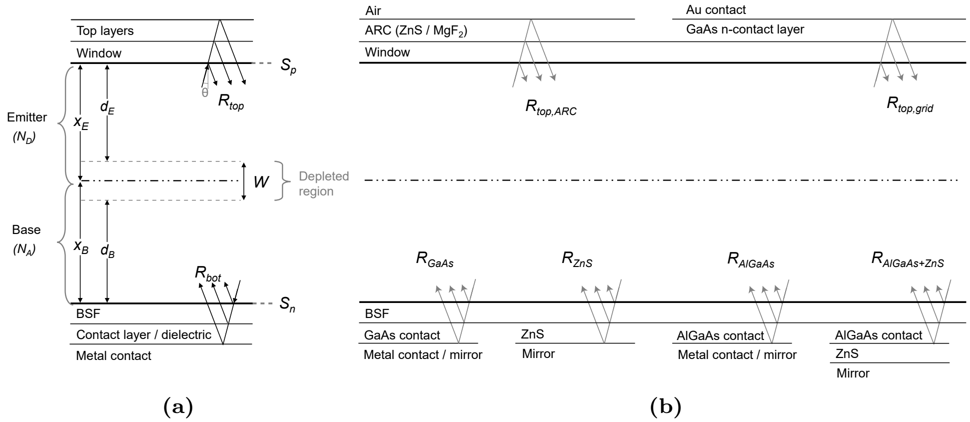

Figure 5.1: Schematic representation of a) the solar cell structure and main parameters, and b) the different top an bottom layer structures evaluated in this study.

For the electrical analysis of the solar cells, the minority carriers mobility ($\mu_{p(n)}$) and diffusion coefficient $D_{p(n)}$ of the devices were calculated according to the empirical model described by Sotoodeh et al. [68], and the minority carriers' lifetimes τ_p and τ_p were theoretically defined as in the study of Lumb et al. [20] by:

$$\frac{1}{\tau_{p(n)}} = \frac{1 - f_{PR}}{\tau_{p(n),rad}} + \frac{1}{\tau_{p(n),SRH}}, \tag{5.2}$$

where the subscripts *rad* and *SRH* indicate the radiative and Shockley-Read-Hall recombination lifetimes, respectively. The diffusion length is determined by $L_{p(n)} = \sqrt{D_{p(n)}\tau_{p(n)}}$. For thermodynamic consistency, the radiative recombination rate coefficient B was calculated by integrating the spontaneous emission rate associated with the GaAs optical data used in the other calculations, and is found to be 6.22x10^{-10} cm^3/s.

5.3 Results and Discussion

5.3.1 Optical analysis of the solar cell performance

In order to circumvent the limitation of previously reported rear contact patterning approaches [61, 64], a smaller pattern for the rear contact consisting of 20 μm radius discs was developed and applied to the rear of solar cells from epi-structures A and B. In this manner, the distance between contact spots was reduced significantly, as shown in the photographs of figure 5.2, allowing the production of cells with very low C$_r$. In the photographs taken under inclined illumination (top row of figure 5.2) it is possible to visualize the contact spots, which are hard to be observed in the electroluminescence images (bottom row of figure 5.2) due to the small distance between them. The illuminated $J-V$ parameters of the best performing cells from structures A and B as shown in table 5.1 indicate that by applying these small radius contact points the FF of the cells does not show a sudden large drop at C$_r$ = 10% [61, 64]. Even for cells with C$_r$ as low as 3%, the FF is only less than 1% point lower than reference cells (C$_r$ = 100%), while for the more extreme case of C$_r$ = 1.5% the FF is less than 3% points lower.

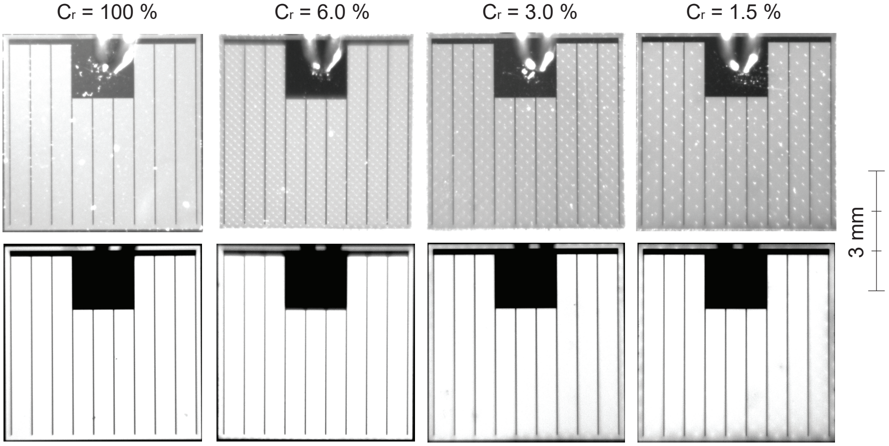

Figure 5.2: Inclined illumination (top row) and electroluminescence (bottom row) images of the solar cells from structure B with different C$_r$. The applied current for the electroluminescence images and camera settings were kept the same for each series of measurement.

The simulations in figure 5.3 show the wavelength (λ) and angle of incidence (θ) dependent reflectance at the interface structures that represent parts of the top (R_{top}) and at the bottom (R_{bot}) of the cells studied in this work (see schematic representation in figure 5.1b). For reference, the calculated spontaneous radiative emission

Table 5.1: Illuminated $J-V$ parameters of the best cells of each configuration.

	C_r [%]	V_{oc} [mV]	J_{sc} [mA/cm^2]	FF [%]	η [%]
Structure A	100	1058.8	23.1	85.0	21.0
	20	1063.5	23.1	84.4	20.8
	15	1068.4	23.6	84.3	21.3
	10	1069.7	23.4	84.6	21.3
Structure B	100	1062.2	23.0	84.5	20.6
	6.0	1067.3	23.3	84.1	20.7
	3.0	1069.5	23.2	84.0	20.8
	1.5	1071.0	23.7	82.2	20.8
Structure C	100	1078.0	28.0	72.6	21.9
	10	1076.7	28.0	75.4	22.8

distribution of GaAs is highlighted in the reflectance maps. For the wavelength range of interest, the top reflectance of the open cell areas ($R_{top,ARC}$, figure 5.3a) is high (>95%) for angles of incidence larger than the escape cone ($\approx 16^o$), and the low reflectance of light with wavelength below 500 nm is associated with absorption in the window layer. Underneath the grid contacts, on the other hand, the top reflectance ($R_{top,grid}$, figure 5.3b) is considerably lower, due to the high absorption of the n-GaAs contact layer.

Four different structures for the bottom interfaces were simulated: a structure containing a 100 nm GaAs contact layer (R_{GaAs}, figure 5.3c), representative of C_r = 100%, a structure from which the contact layer was removed and 60 nm ZnS deposited in its place (R_{ZnS}, figure 5.3d), representative of $C_r = 0$, a structure with a 150 nm AlGaAs as contact layer (R_{AlGaAs}, figure 5.3e) and a structure with a 150 nm AlGaAs and 60 nm ZnS deposited on top ($R_{AlGaAs+ZnS}$, figure 5.3f). All simulated structures have Au as rear contact and/or mirror. For photons in the wavelength range associated with the emissions from GaAs, R_{ZnS}, R_{AlGaAs} and $R_{AlGaAs+ZnS}$ are higher than R_{GaAs} for virtually all angles of incidence. AlGaAs is a material with higher bandgap than GaAs, and therefore does not absorb photons with wavelengths close to that of the GaAs emissions. However, the fabrication of AlGaAs layers with doping levels high enough to provide a low ohmic contact resistance, similar to that of GaAs, is difficult, and therefore not always applied.

The calculated f_{PR} using equation 5.1 for solar cells as a function of R_{bot} for a range of thicknesses are presented in figure 5.4a. In these calculations, R_{top} is taken as shown in figure 5.3a (disregarding losses in the front contact), and R_{bot} is considered to be an absolute value, independent of photon energy or angle of incidence. For cells with a perfect mirror (R_{bot}= 100%), all radiative losses represent photons being

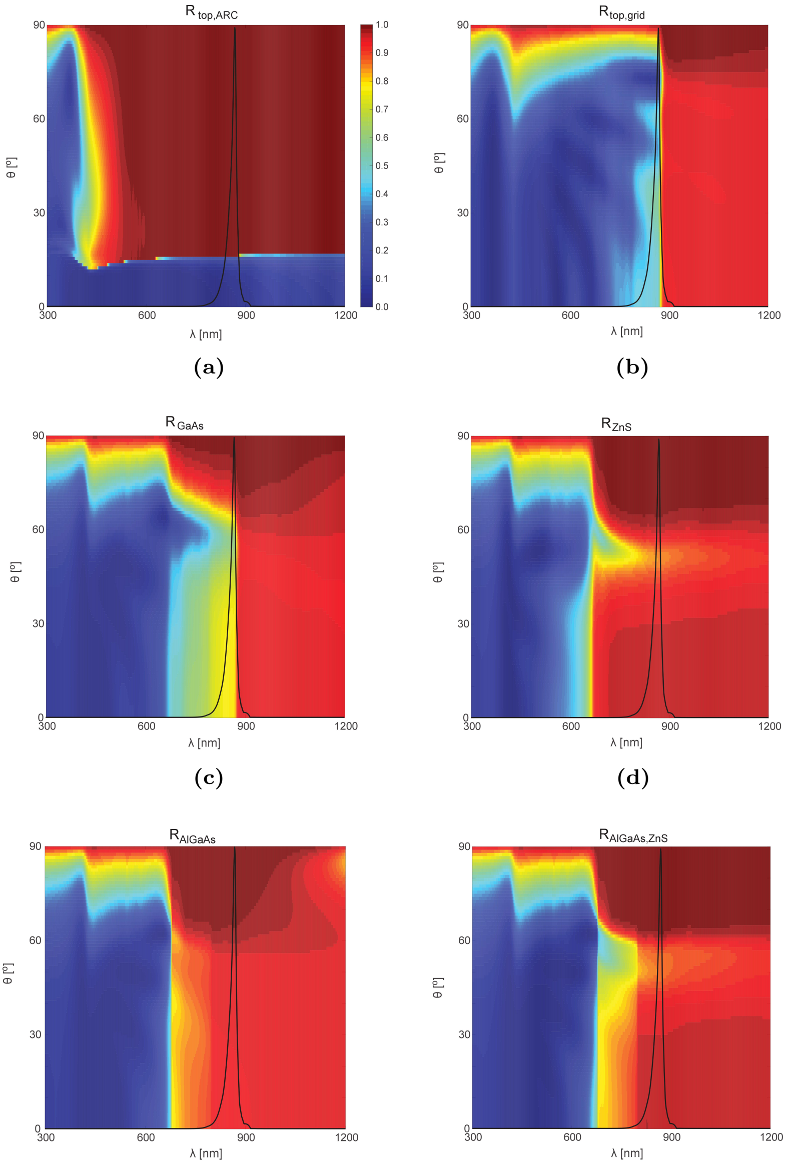

(a) **(b)**

(c) **(d)**

(e) **(f)**

Figure 5.3: Reflectance maps of the different interfaces evaluated: (a) the internal top reflectance of a region with ARC, (b) the internal top reflectance of a region underneath the metal contacts, and the internal bottom reflectance in solar cells with (c) a 100 nm GaAs contact layer, (d) contact layer replaced with a 60 nm ZnS layer, (e) a 150 nm AlGaAs contact layer and (f) a 150 nm AlGaAs contact layer with 60 nm ZnS. The reflectance intensity scale is valid for all maps and the black peak represents the calculated GaAs emission distribution.

absorbed in or escaping through the front layers. Thicker devices are less dependent on the reflectances of the interfaces, denoted by their less steep curve slope. This highlights the importance of an optimized optical design in the development of thin and ultra-thin solar cells [41, 55, 56].

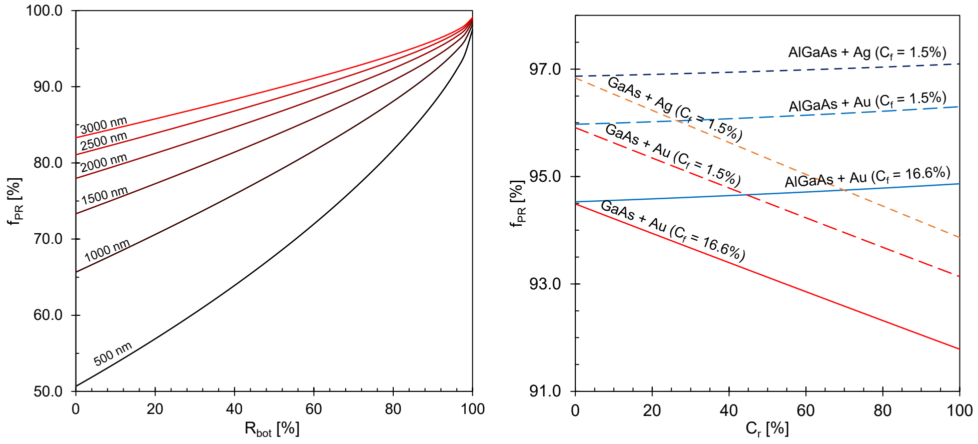

(a) **(b)**

Figure 5.4: Photon recycling factor as a function of a) the rear contact reflectance for solar cells with different active layer thicknesses and b) the rear contact coverage of solar cells with different materials for *p*-contact layer and mirror.

In order to calculate the photon recycling factor of the patterned solar cells, the resulting R_{top} and R_{bot} of each cell configuration needs to be determined. Because the horizontal dimensions of the applied front grid contacts and rear contact spots are large in comparison to the incident light wavelength, we consider R_{top} and R_{bot} to be the average reflectance of the different regions making up the surfaces of the cells. Therefore:

$$R_{top}(\theta,\lambda) = \mathrm{C}_f \times R_{top,grid}(\theta,\lambda) + (1-\mathrm{C}_f) \times R_{top,ARC}(\theta,\lambda), \tag{5.3}$$

for all solar cells structures, and

$$R_{bot}(\theta,\lambda) = \mathrm{C}_r \times R_{GaAs}(\theta,\lambda) + (1-\mathrm{C}_r) \times R_{ZnS}(\theta,\lambda), \tag{5.4a}$$

for cells from epi-structures A and B, or

$$R_{bot}(\theta,\lambda) = \mathrm{C}_r \times R_{AlGaAs}(\theta,\lambda) + (1-\mathrm{C}_r) \times R_{AlGaAs+ZnS}(\theta,\lambda), \tag{5.4b}$$

for cells from epi-structure C.

Figure 5.4b depicts f_{PR} as a function of C$_r$, calculated considering the R_{bot} as in equation 5.4a and the thickness of epi-structures A and B. Two different front configurations are considered for the determination of R_{top}: the applied grid with C$_f$ = 16.6% (solid lines) and an optimized low front contact coverage of C$_f$ = 1.5% (dashed lines). It is shown that, for the epi-structures A and B (red lines), the maximum f_{PR} to be reached with low coverage front contacts is close to 96%, approximately 2.8 % absolute increase as compared to the non-patterned cells. For the cells with C$_f$ = 16.6%, there is an overall reduction in photon recycling of 1.4% absolute, identifying the front contact grid coverage as an important limiting factor to the cells optical quality. Furthermore, higher photon recycling values can theoretically be obtained by applying other metals or contact layer materials, as is also depicted in the picture for the case of AlGaAs as contact layer (blue lines) and Ag as rear contact and/or mirror.

Interestingly, according to these calculations, the patterning does not improve the photon recycling factor of solar cells with AlGaAs as contact layer, and in fact it decreases up to ≈ 0.4% points for C$_r$ = 0 as compared to C$_r$ = 100%. The main reason for that is that ZnS is moderately absorbing at higher angles of incidence, as can be seen on the reflectance map of figure 5.3c, and in more detail for λ = 870 nm in figure 5.5. Although R_{ZnS} and $R_{AlGaAs+ZnS}$ are higher than R_{AlGaAs} for normal incident photons, they are lower when averaged for all angles of incidence, and therefore f_{PR} decreases with the patterning.

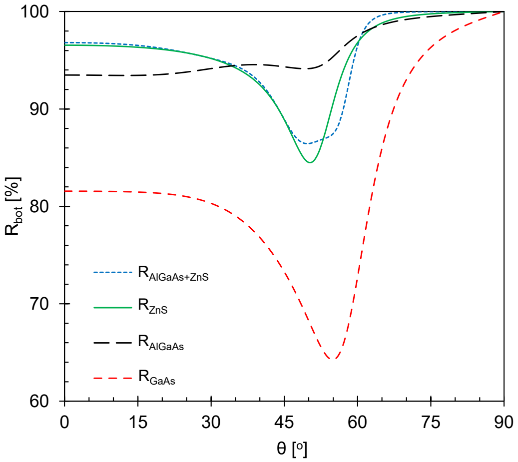

Figure 5.5: Calculated angle-dependent reflectance of the four studied bottom layer structures for λ = 870 nm.

Since the simulations show negligible difference between R_{ZnS} and $R_{AlGaAs+ZnS}$ at the wavelength range of GaAs emissions, the produced solar cells from epi-structure C had ZnS locally deposited on top of the contact layer, as opposed to replacing it, in order to avoid an unnecessary etching step. The experimentally measured specular reflectance of the two cells processed from structure C are shown in figure 5.6. For the light with wavelength just above the GaAs band cut-off, the patterning in fact increases the reflectance at normal incidence. However, the illuminated $J-V$ parameters from these cells, depicted in table 5.1, show that, as expected from the photon recycling calculations, the J_{sc} and V_{oc} values of both cells are similar, denoting that there is no optical benefit in applying a pattern to the rear contact. Note that the devices present a much lower fill factor (FF) than the cells produced from structures A and B, because the applied metal grid contacts are thinner (100 nm vs 200 nm), whereas they should be thicker in order to compensate for the lower front grid coverage.

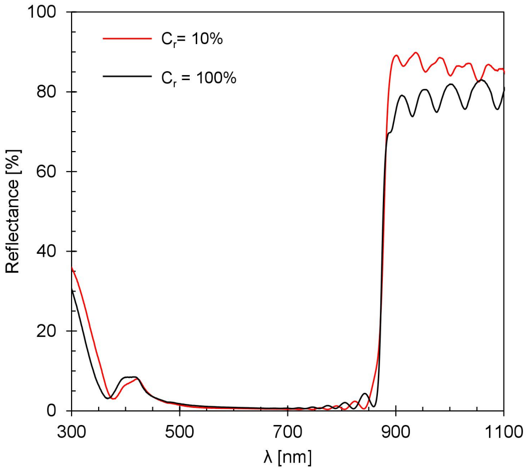

Figure 5.6: Measured reflectance at normal incidence for solar cells produced from epi-structure C.

The expected open circuit voltage of the produced cells can be calculated by [9]:

$$V_{oc} = V_{db} + \frac{kT}{q} ln(\eta_{ext}) \tag{5.5}$$

where V_{db} is the detailed balance limit voltage, and η_{ext} is the external radiative efficiency. In order to predict the open circuit voltage of the solar cells due to deliberate changes in the rear mirror design, the external radiation efficiency is calculated by [19]:

$$\eta_{ext} = \frac{\eta_{int} f_{esc}}{1 - \eta_{int} f_{PR}}, \tag{5.6}$$

where η_{int} is the internal radiative efficiency, defined as the fraction of all recombination events in the solar cell that takes place radiatively. While f_{PR} and f_{esc} can be easily calculated using the optical data of the applied materials in the device, η_{int} is related to the overall quality of the solar cells and varies greatly depending on growth and processing conditions. Using constant values for $V_{db} = 1.145$ V [19, 65] and for $f_{esc} = 1.08\%$ (which is the average of the cells from structure A and B), V_{oc} as a function of f_{PR} is calculated for a range of η_{int} values, and shown in figure 5.7.

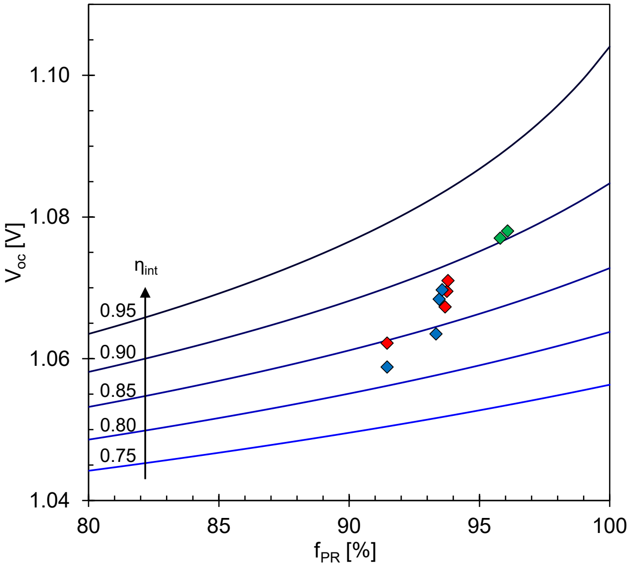

Figure 5.7: Open circuit voltage as a function of the photon recycling factor for different internal radiative efficiency values. The markers represent the V_{oc} values related to their calculated f_{PR}, for cells from structure A (blue), B (red) and C (green).

For comparison, the experimental V_{oc} values of cells fabricated from the epi-structures A, B and C together with their calculated f_{PR} values are also included in figure 5.7. Even though the assumptions used in the calculations do not apply for the different structures, they are a good indication of the range of the devices internal radiative efficiency. Most of these cells have η_{int} values in between 80 and 90%, which means that, aside from rear mirror reflectance, there are other aspects limiting the photon recycling efficiency of the cells.

5.3.2 Electrical analysis of the solar cell performance

The analysis of the solar cells dark curves allows us to gauge the overall quality of the devices. Solar cells in the dark under forward bias are generally analyzed as two diodes in parallel, expressed by:

$$J_{dark} = J_{01}\left(e^{\frac{q(V+JR_s)}{k\mathrm{T}}}-1\right)+J_{02}\left(e^{\frac{q(V+JR_s)}{2k\mathrm{T}}}-1\right)+\frac{V+JR_s}{R_{sh}}, \tag{5.7}$$

where J_{01} and J_{02} are the saturation current densities at the $1kT$ and $2kT$ components, respectively. In this equation, q is the electron charge, k is the Boltzmann constant, T is the temperature and R_{sh} and R_s are the parasitic shunt and series resistances, respectively. The here evaluated solar cells all have sufficiently large R_{sh} (at least 1x10^8 Ωcm^2) so there is no visible effect in the dark curves, and possible effects of R_s in the curves are circumvented by the use of $J_{sc}-V_{oc}$ data under different light intensities. The extracted dark parameters from the fit of equation 5.7 for the different cell geometries are shown in table 5.2.

Table 5.2: Dark $J-V$ parameters of the best cells of each configuration.

	C$_r$ [%]	J_{01} [A/cm^2]	J_{02} [A/cm^2]
Structure A	100	3.8x10^{-20}	8.5x10^{-12}
	20	3.2x10^{-20}	9.0x10^{-12}
	15	3.0x10^{-20}	9.9x10^{-12}
	10	2.5x10^{-20}	6.5x10^{-12}
Structure B	100	4.5x10^{-20}	1.1x10^{-11}
	6.0	2.3x10^{-20}	5.4x10^{-12}
	3.0	1.9x10^{-20}	1.3x10^{-11}
	1.5	2.0x10^{-20}	6.4x10^{-12}
Structure C	100	2.6x10^{-20}	2.1x10^{-12}
	10	2.7x10^{-20}	1.8x10^{-12}

J_{02} represents the non-radiative recombination that takes place predominantely in the space charge region ($J_{SCR,0}$) and the perimeter ($J_{perim,0}$) of the cell, dominating the dark current of the cells at lower voltages. At higher voltages, on the other hand, the dark curve is dominated by J_{01}, which is composed by the sum of the diffusion ($J_{diff,0}$) and radiative ($J_{rad,0}$) recombination current densities [73, 74]. Therefore we can define J_{01} and J_{02} by:

$$J_{01} = J_{diff,0} + J_{rad,0} \tag{5.8a}$$

and

$$J_{02} = J_{SCR,0} + J_{perim,0}, \tag{5.8b}$$

from which $J_{SCR,0}$, $J_{diff,0}$ and $J_{rad,0}$ can be calculated using the method described by

Sun et al. [69] for cells with $L_{p(n)} \gg d_{E(B)}$. In this model, the theoretically calculated values for the required input parameters ($D_{p(n)}$ and $\tau_{p(n),SRH}$) can be used [20, 68], and the top and bottom interface recombination velocities (S_p and S_n, respectively) are fitted for $J_{diff,0}$. For cells with the DJ geometry, the dark current is found to be largely influenced by small changes in S_p, while it is less sensitive to changes in S_n. Therefore, S_n is considered to be of similar order of magnitude as S_p, and the values used in the model for both recombination velocities are taken to be the same.

The perimeter recombination fraction is generally not computed in dark curve analysis as in equation 5.8b. However, it can account for a large fraction of the dark current of small solar cells, such as the cells applied in CPV systems and the here studied 0.5 x 0.5 cm^2 devices, for which the perimeter-to-area ratio (P/A) is large [53, 74]. In contrast to the other saturation current densities, $J_{perim,0}$ is difficult to predict, since it can vary strongly as a function of the quality of the technique that defines the solar cell area (such as the used MESA etchants). In large cells, however, J_{02} is likely to be mostly limited by $J_{SCR,0}$.

The expected increase in photon recycling due to the increased reflectance of the rear layers of the solar cells will only reduce $J_{rad,0}$ (and therefore reduce J_{01}), whereas $J_{diff,0}$ is limited by the quality of the hetero-interfaces [57,69]. In order to fully benefit from the increase in photon recycling, it is important that $J_{rad,0}$ dominates the dark curve at $V \approx V_{oc}$, and therefore $J_{diff,0}$ and $J_{perim,0}$ should be as low as possible.

The dark characteristics composition of the studied solar cells with $\text{C}_r = 100\%$ (epi-structure B) is shown in figure 5.8a, which shows that $J_{perim,0}$ is much higher than $J_{SCR,0}$, limiting the dark curve at lower voltages. Furthermore, $J_{diff,0}$ is larger than $J_{rad,0}$ even for the cells with $\text{C}_r = 100\%$, due to S_p and S_n values in the order of magnitude of $\approx$ 4x10^3 cm/s. This indicates that the interface quality, together with perimeter recombination, are the main limiting elements determining the η_{int} value of these solar cells, and need to be addressed for a successful production of high efficiency devices.

In order to verify the model identifying these limits in photon recycling improvement, cells from epi-structure C were fabricated with a thicker emitter and using AlGaAs as contact layer. In an attempt to increase η_{int} by reducing the perimeter recombination, the optimized devices measure 1.0x1.0 cm^2, with $\text{C}_f = 8\%$. The increased cell size reduces the number of cells that can be produced from this epi-structure, and therefore only two rear contact patterns were applied to the structure, either with $\text{C}_r = 100\%$ or $\text{C}_r = 10\%$. The experimentally obtained V_{oc} together with the calculated f_{PR} values of these cells, included in figure 5.7 (green markers), clearly indicate that the η_{int} of the 1x1 cm^2 devices is higher than that of the 0.5x0.5 cm^2 cells.

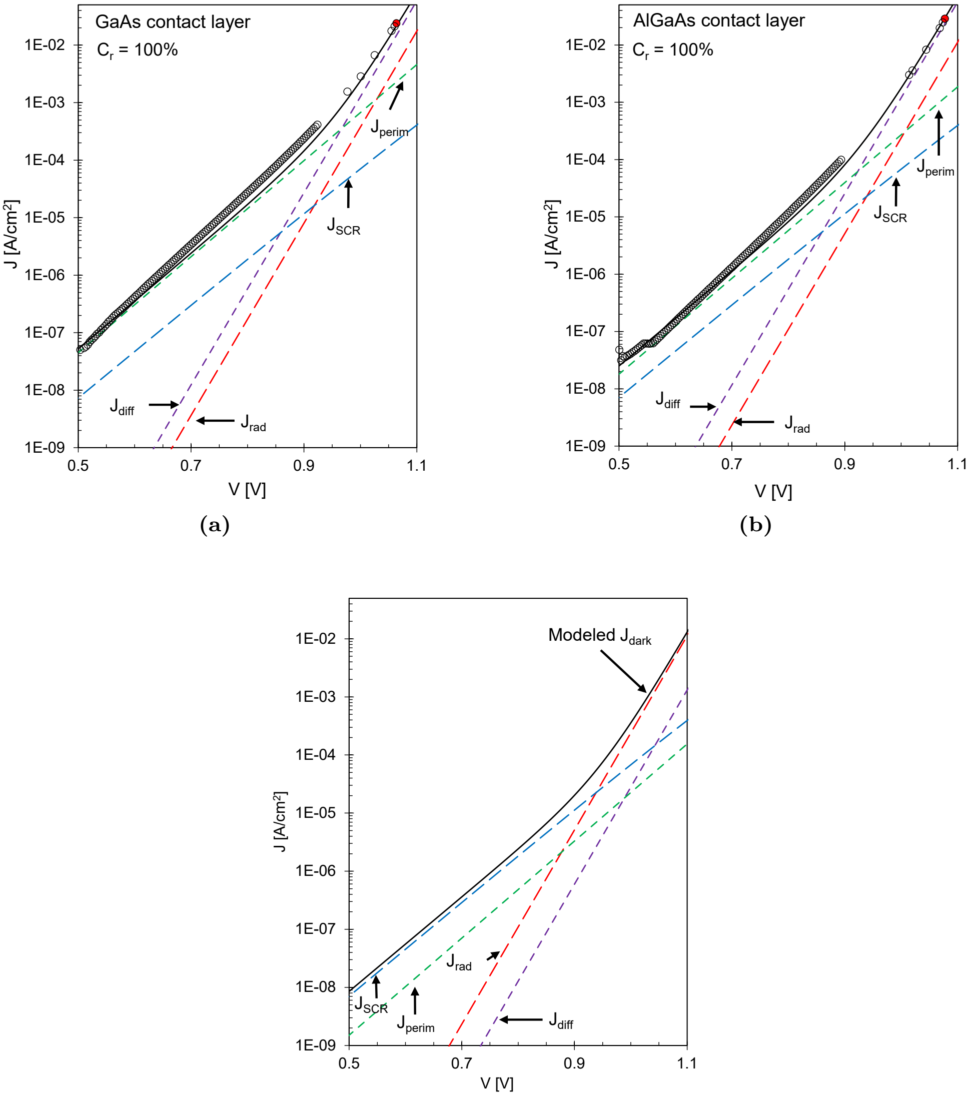

(a) **(b)**

(c)

Figure 5.8: Experimental (markers) and modeled (solid line) dark characteristics of a) a thin-film solar cell with GaAs as contact layer (C_r = 100%), b) a thin-film solar cell with AlGaAs as contact layer (C_r = 100%) and c) an example of dark curve representative of a thin-film solar cell with high quality hetero-interfaces and small P/A. The curves are modeled as the sum of the diffusion (J_{diff}, purple), radiative (J_{rad}, red), perimeter (J_{perim}, green) and space charge region (J_{SCR}, blue) recombination current densities. The red marker in a) and b) represent the J_{sc} and V_{oc} values under AM1.5G illumination.

The dark parameters of the AlGaAs cells extracted by the fitting the measurements to equation 2.9 are also depicted in table 5.2, and the modeled dark curve of the AlGaAs cell with $C_r = 100\%$ is shown in figure 5.8b. There is no significant difference between the dark parameters of the two configurations from structure C, indicating a small variation in f_{PR}. The J_{02} values are lower for these cells than for the 0.5x0.5 cm^2 cells, as a result of the lower impact of the perimeter recombination on the device performance, which is clearly visible in figure 5.8b. Though lower, also for the 1.0x1.0 cm^2 cells $J_{perim,0}$ is higher than $J_{SCR,0}$, indicating that the performance of the devices would benefit from either producing larger cells or applying a passivation technique [75, 76].

Also for the cells from structure C, $J_{diff,0} > J_{rad,0}$, but $J_{rad,0}$ is slightly lower than for the previous cells. The fact that $S_{p(n)}$ is of the same order of magnitude ($\approx$ 4x10^3 cm/s) as for the cells from structures A and B causes both structures to have similar $J_{diff,0}$, and therefore the decrease in J_{01} is small. The non-negligible $S_{p(n)}$ values indicate a sub-optimal passivation from the window and BSF layers, most likely due to a lower epi-layer quality at the hetero-interfaces, as recently has been addressed in the literature [77–80]. A meticulous control of chemical composition, material interdiffusion and surface segregation is necessary in order to prevent the formation of mixed compounds that reduce the abruptness of the interfaces.

A theoretical example of dark curve from a thin-film solar cell in which J_{perim} and J_{diff} are not limiting the dark characteristics is shown in figure 5.8c. This curve demonstrates the potential performance of cells from epi-structure C processed with very low P/A and with an effective passivation provided by the window and BSF layers. In this example, $J_{perim,0}$ is set to 1x10^{-13} A/cm^2 and $S_{p(n)} = 100$ cm/s, resulting in an approximated J_{01} of 5x10^{-21} A/cm^2. The expected $J_{diff,0}$ for this structure is much lower than $J_{rad,0}$, which results in a larger sensitivity of the dark curve to changes in the photon recycling factor. Therefore, it becomes clear that fine tuning the growth conditions of the hetero-interfaces, and therefore achieving high quality interface passivation, is one of the most important guidelines towards the fabrication of solar cells that can fully benefit from an efficient photon recycling. Furthermore, for applications such as concentration systems, in which cells are often required to have small dimensions, the use of a perimeter passivation technique must be considered in order to overcome the limitations imposed by perimeter recombination.

5.4 Conclusions

The present study further develops a technique of patterning the bottom contact layer of single junction thin-film GaAs solar cells previously shown in the literature, and the reported sudden decrease in FF for rear coverages lower than 10% is no longer observed. The production of functional devices with rear contact coverages as low as 1.5% was achieved, and the produced cells show a direct correlation between total bottom reflectance and the solar cell performance.

A combination of optical and electrical models reported in the literature was used in order to pinpoint the performance limiting mechanisms of these solar cells. Using this approach it was demonstrated that the front grid coverage, usually disregarded in rear mirror focused studies, reduces the photon recycling probability, and therefore limits the maximum open circuit voltage that the devices can achieve. Furthermore, perimeter and interface recombination were identified to obstruct the internal radiative efficiency of the solar cells, preventing further increase of the devices' open circuit voltage as a result of improvements to the rear mirror of the cells.

The perimeter recombination contribution to the solar cells dark characteristics can be reduced by the production of large area cells, but for the devices with P/A = 4 cm^{-1} evaluated in this study, J_{perim} is still limiting the dark curve at lower voltages. In addition, the reduction of at least one order of magnitude in the interface recombination velocities is required in order to sufficiently decrease the diffusion fraction of the solar cells dark currents, and therefore allow a significant benefit of increased photon recycling probability to the solar cell performance.

Acknowledgements

The authors acknowledge financial support from the Brazilian National Council for Scientific and Technological Development (CNPq), under the program Science Without Border, project number 233259/2014-7, and funding under grant agreement 17043 REGENERATION from the European institute for Innovation and technology (EIT), a body supported by the European Union's Horizon 2020 research and innovation program.

Chapter 6

Electron radiation induced degradation of GaAs solar cells[1]

Abstract

The effects of electron irradiation on the performance of GaAs solar cells with a range of architectures is studied. Solar cells with shallow and deep junction designs processed on the native wafer as well as into a thin-film were irradiated by 1-MeV electrons with fluence up to 1x10^{15} e^{-}/cm^{2}. The degradation of the cell performance due to irradiation was studied experimentally and theoretically using model simulations, and a coherent set of minority carriers' lifetime damage constants was derived. The solar cell performance degradation primarily depends on the junction depth and the thickness of the active layers, whereas the material damage shows to be insensitive to the cell architecture and fabrication steps. The modeling study has pointed out that besides the reduction of carriers lifetime, the electron irradiation strongly affects the quality of hetero-interfaces, an effect scarcely addressed in the literature. It is demonstrated that linear increase with the electron fluence of the surface recombination velocity at the front and rear hetero-interfaces of the solar cell accurately describes the degradation of the spectral response and dark current characteristic upon irradiation. A shallow junction solar cell processed into a thin-film device has the lowest sensitivity to electron radiation, showing an efficiency at the end of life equivalent to 82% of the beginning-of-life efficiency.

---

[1] The work presented in this section is based on "Electron radiation induced degradation of GaAs solar cells with different architectures", by N. Gruginskie, F. Cappelluti, G. Bauhuis, P. Mulder, E.J. Haverkamp, E. Vlieg and J.J. Schermer in Progress in Photovoltaics: Research and Application (2019).

6.1 Introduction

A standard space solar cell array consists of triple junction III-V cells on Ge wafer. These devices provide efficiencies well above 30% [81], but they are rigid devices with relatively large weight. These cells are generally mounted on stabilizing panels consisting of an aluminum honeycomb structure sandwiched by carbon fiber reinforced polymer (CFRP) sheets, and a Ce-doped protective cover glass is applied on top of the system. The resulting array in these configurations can present specific mass around 2.6 kg/m^2 [58]. In order to reduce the power-to-weight ratio of these systems, and therefore considerably reducing launching costs, the thickness of the Ge wafer used for epitaxial growth can be reduced [82, 83], which results in lighter yet rigid devices. By removing the growth substrate completely, the resultant solar cells consist of lightweight and flexible thin-film devices. These cells no longer require to be mounted on rigid panels for application, and when combined with new technologies for flexible front cover-glasses and mounting and deployment systems, have the potential to reach specific mass of 0.6 kg/m^2 [11, 58, 60]. With some substrate removal techniques such as the epitaxial lift-off (ELO) process [22–24], the expensive wafer can be applied to produce multiple cell structures [25, 29, 84], further reducing the price of the solar cells.

By removing the Ge wafer, structures such as the tandem thin-film InGaP/GaAs solar cells appear to be promising for space solar arrays. The removal of the substrate also allows access to the rear contact, resulting in the development of new architectures [31, 40, 56]. Owing to the possibility of applying a back reflector, thin-film devices require smaller active layer thicknesses, further reducing costs related to both the weight and the growth of the epitaxial layers. The reflectance of the rear mirror in high quality materials has also been proven important to maximize photon recycling, which in turn increases the open circuit voltage and therefore the efficiency of the devices [9, 19, 20, 26, 48, 64].

In these structures, the bottom sub-cell consists of thin-film GaAs, which has demonstrated the highest conversion efficiency among all types of single junction solar cells [81]. Additionally to back contact design strategies [85–87], the position of the junction in GaAs cells has been identified as an important parameter, showing that a device with the junction closer to the bottom of *n*-on-*p* cells allows for operation in the radiative recombination regime [20, 45, 88]. This type of cell, therefore, has a higher open circuit voltage and is preferred over the standard structure with a junction located closer to the front. But even though the deep junction design allows for better performance at the beginning-of-life, its resilience in the space environment is expected to be lower than that of the conventional shallow junction design [89, 90].

The most challenging aspects for solar cells in space are the exposure to particle irradiation and the temperature cycling. Because of the copper commonly applied as the flexible carrier for thin-film GaAs cells, degradation related to copper diffusion is a potential problem for devices with this architecture. It has been shown that the effects of copper-diffusion are temperature dependent, and for temperatures below 200^oC it does not reduce the cell performance in drastic degrees, provided the absence of damages induced by thermal stress, such as cracks or bends [91].

The level of irradiation that cells would face throughout their entire lifetime in space depends on the type of mission. Based on the hypothesis that the permanent displacement damage produced by the incidence of charged particles is the main aspect that degrades the device performance in space, the mission equivalent damage from electrons, protons, ions and neutrons of different energies can be averaged by a certain electron fluence [92–95]. Geostationary orbit missions (GEO) usually last for 15 years and the damage created by the irradiation environment is equivalent to that obtained by a fluence of $1\text{x}10^{15}$ 1-MeV electrons/cm^2. For low Earth orbit missions (LEO), that last for approximate 10 years at a lower altitude, the equivalent fluences are 5 to 10 times lower.

The recombination centers formed in GaAs solar cells under irradiation have been studied in depth [28, 92, 93, 95–97] and the implications of the junction position with lifetime degradation have been discussed [89, 90]. It is generally understood that irradiation reduces the minority carriers' diffusion length, and therefore the average distance that these carriers have to travel before reaching the $p-n$ junction directly affect the cells resilience to the space environment. A systematic study of different architectures, however, has not yet been reported, and there is a lack of consistency between the previously reported minority carriers' lifetime degradation constants. Furthermore, in view of the current trend of developing thin and ultra-thin radiation-hard solar cells [56], knowledge of the possible impact of irradiation on emitter-window and base-BSF hetero-interfaces surface recombination velocities is becoming increasingly important. For silicon cells, Imaizumi et al. already suggested, based on EQE analysis, that irradiation has increased the surface recombination velocity [98].

In the current study, the possible influence of electron irradiation on hetero-interfaces of GaAs solar cells is systematically investigated. For this purpose, GaAs cells with different junction depths with respect to the hetero-interfaces both on their native substrates and processed into genuine thin-film devices subjected to 1-MeV electron radiation. Consistent modeling to simulate the experimental results from all the different cell geometries simultaneously is applied to derive a coherent set of minority carriers' lifetime damage constants. At the same time, the actual relations between the electron fluence and resulting surface recombination velocities of the front and rear hetero-interfaces of the cells are determined.

6.2 Methods

6.2.1 Experimental details

Solar cells with different structures were subjected to a total electron fluence of $1\text{x}10^{15}$ e^-/cm^2 of 1-MeV radiation, which corresponds to a 15 years GEO mission [94]. The irradiation was performed at the Reactor Institute Delft (RID) of the Delft University of Technology, using a Van der Graaf accelerator with an electron flux of $5\text{x}10^{11}$ e^-/cm^2s. The available structures for this study consisted of two substrate based (SB) and three thin-film (TF) GaAs solar cells, with either a thin *n*-doped emitter and a thick *p*-doped base, here called a shallow junction (SJ) geometry, or a thick *n*-doped emitter and a thin *p*-doped base, here called a deep junction (DJ) geometry, as depicted in figure 6.1.

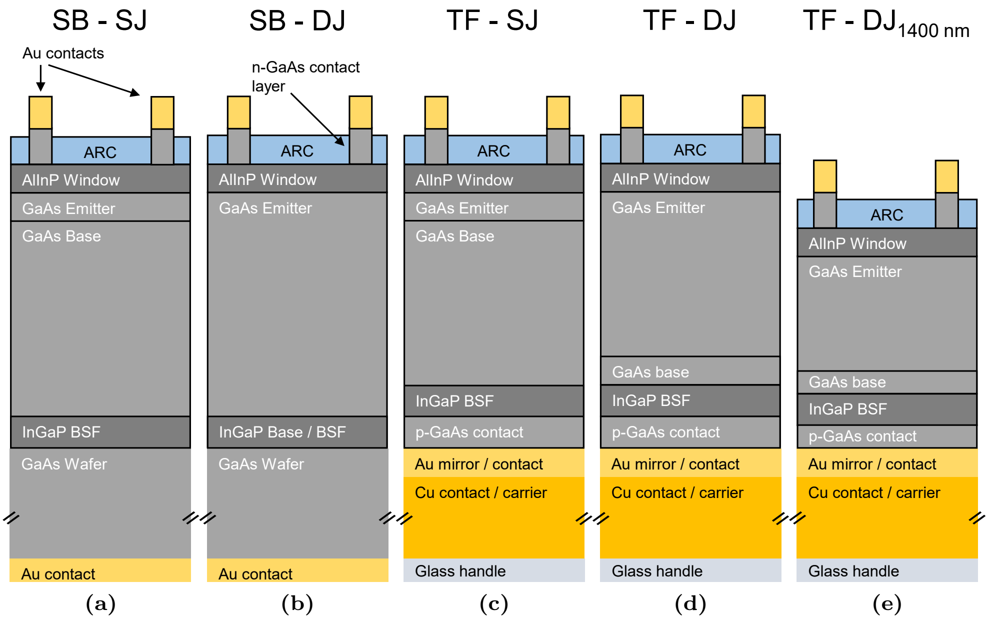

Figure 6.1: Device schematic of the five different GaAs cell geometries under study: a) substrate based shallow junction, b) substrate based deep junction, c) thin-film shallow junction, d) thin-film deep junction and e) thinner thin-film deep junction.

The thickness and doping levels of the layers, as obtained by MOCVD growth on

2-inch (100) GaAs wafers 2^o off to (110) orientation, are summarized in table 6.1. It is important to notice that the SB - DJ solar cells have a heterojunction, meaning that an InGaP layer functions both as base and as back surface field (BSF). Because we expect the thickness to have an impact on the degradation [96], most of the structures have comparable GaAs thickness, and one of the thin-film cell structures has a significantly thinner (1400 nm) active layer, that will be referenced as TF - DJ_{1400nm}.

Table 6.1: Summary of solar cell structures used in this study

Solar cell reference	SB-SJ	SB-DJ	TF-SJ	TF-DJ	TF-DJ_{1400nm}
Emitter thickness [nm]	100	2200	75	2000	1320
Base thickness [nm]	2100	100	2000	75	80
Emittted n-doping [cm^{-3}]	$3x10^{18}$	$5x10^{16}$	$3x10^{18}$	$5x10^{16}$	$5x10^{16}$
Base p-doping [cm^{-3}]	$3x10^{16}$	$5x10^{17}$	$3x10^{16}$	$1x10^{18}$	$1x10^{18}$

The cells all have e-beam evaporated metal contacts and thermally evaporated MgF_2/ZnS ARC coatings. Their cell areas were defined by a MESA etch using an ammonia:hydrogen peroxide solution for the GaAs layers and either HCl 37% or a $HBr:Br_2:H_2O$ solution for the phosphide layers. The top n-GaAs contact layer between the grid fingers was removed also using an ammonia:hydrogen peroxide solution. The substrate based solar cells measure 1x1 cm^2 and have a frontal metal grid consisting of 100 nm thick Au and 6000 nm Cu, covering 1.2% of the total area. After processing, the substrate based cells were diced and individually mounted on a chip carrier (see figure 6.2a).

The thin-film cells measure 0.5 x 0.5 cm^2 and have 200 nm thick Au front contact that covers 16.6% of the cell area. The substrates were simply removed by etching with an aqueous citric acid and hydrogen peroxide solution. Subsequently a 200 nm thick full Au contact/mirror was evaporated onto the rear side of the cell and the structures were mounted on a copper foil that acts as a conductive foreign carrier. The foils consisting of multiple cells and several dedicated structures without grid for EQE analysis, were glued as a whole on a glass handling carrier (see figure 6.2b).

For each configuration, 3 to 9 individual solar cells were irradiated and characterized. The irradiation was interrupted five times in the interval between $1x10^{13}$ and $1x10^{15}$ e^-/cm^2 to allow for intermediate on-site $J-V$ measurements under approximately 1000 W/m^2 AM1.5G conditions at a temperature of approximately 25^oC. For this purpose, a mobile set-up consisting of a Keithley 2401 multimeter with a portable solar simulator was used while ReRa Tracer3 was applied for data acquisition. By measuring the short current density of an NREL calibrated reference cell before each

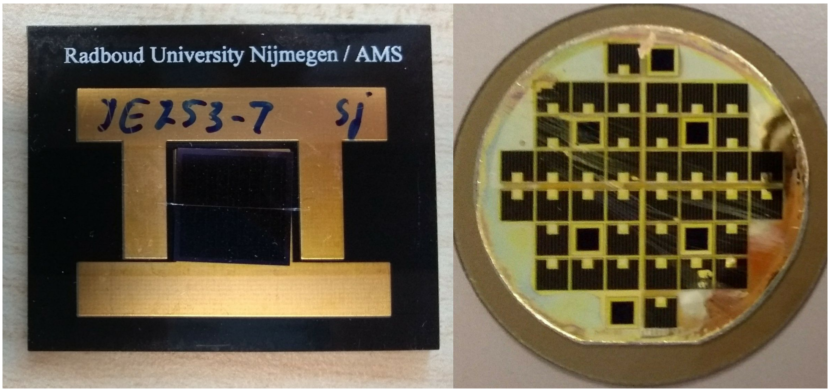

(a) (b)

Figure 6.2: Photograph of a) an individual 1 x 1 cm^2 substrate based solar cell mounted on a PCB board and b) a set of multiple 0.5 x 0.5 cm^2 thin-film solar cells on a copper foil, mounted on a glass plate for safe handling. The latter also shows a darkening of the glass plate after irradiation.

measurement series, the measured currents of the cells could be scaled to the corresponding values under exactly 1000 W/m^2. With this approach, mutual comparison between different cell geometries can be identified with an accuracy of ±2 mV in V_{oc}, ±0.06 mA/cm^2 in J_{sc} and ±0.003 in FF. The on-site characterization allowed for a minimal interval in between measurements, which dependent on the irradiation time ranged from 10 to 60 minutes.

The external quantum efficiency (EQE) and dark $J-V$ characteristics were measured at the Radboud University before and after all irradiation experiments performed at the RID. The EQE measurements were obtained with a ReRa SpeQuest Quantum Efficiency system, and dark $J-V$ characteristics were obtained using a Keithley 2601B source meter and a heating/cooling water thermostat with a Pt100 temperature sensor to keep the solar cells at a temperature of 25 ^{o}C. Because the series resistance bends the dark curve downwards at higher voltages, a curve composed of short-circuit current (J_{sc}) and open circuit voltage (V_{oc}) values measured under different light intensities represents the ideal diode dark characteristics, as the series resistance is excluded under these conditions [99]. From each configuration, one cell was removed before subjecting the cells to the last irradiation dose in order to obtain EQE and dark $J-V$ curves of cells subjected to intermediate irradiation levels, with the exception of the TF-SJ and TF-DJ$_{1400}$.

6.2.2 Device model

The solar cells subjected to 1-MeV irradiation have been analyzed based on the 1D analytical Hovel model [100] and its extended version for thin-film solar cells with back-side reflector [101]. The model formulation is rather general and well suited to describe different solar cell designs provided that material and geometry parameters are changed accordingly. A schematic depiction of the modeled structure and corresponding variables used in this study are shown in figure 6.3, where X_E and X_B denote the thickness of the emitter and base layers and W denotes the width of the depleted region across the junction.

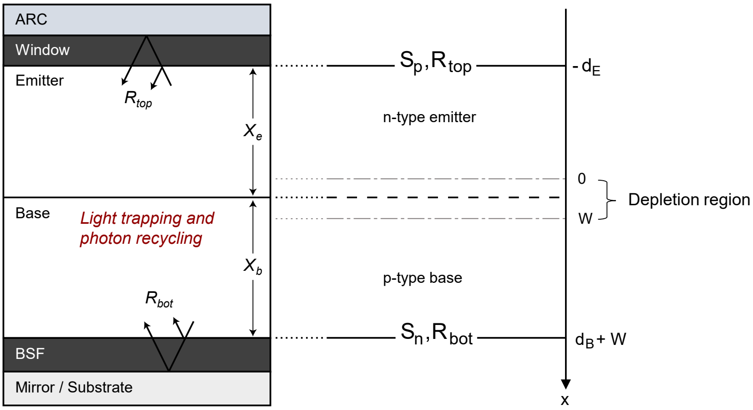

Figure 6.3: Schematic representation of the modeled solar cell structure with the 1D cut-line and parameters definition used in the analytical model (adapted from Lumb et al. [101]).

Under monochromatic illumination, and assuming negligible electrical field and constant material parameters, carrier transport in the quasi neutral regions is modelled by the diffusion equation of minority carriers, including the distributed optical generation term. The effect of window and back surface field layers is phenomenologically described by the interface recombination velocity of p-type minority carriers at the emitter-window interface (S_p) and of n-type minority carriers at the base-BSF interface (S_n), which set the boundary conditions for the diffusion equations in the emitter and base QNRs. At the edge of the depletion-QNR regions the excess minority carrier density is determined by the junction law. Such formulation yields a closed form analytical expression for the optical- and voltage-dependent current contributions associated to the two QNRs. The total spectral photocurrent and the associated EQE results as the sum of the emitter and base QNR contributions and the contribution from the depletion region (where collection efficiency is assumed to be unitary) computed under monochromatic excitation and short-circuit condition. The short circuit current density is calculated by integrating the specific illumination spectrum weighted by the EQE over the wavelength. Concerning the optical generation rate, the distribution of the optical field is calculated based on multiple reflections between the window-emitter interface and the base-BSF interface, characterized by the top reflectance (R_{top}) and by the bottom reflectance (R_{bot}), respectively. The wavelength dependent R_{top} and R_{bot} are derived from 1D electromagnetic simulations for coherent multilayers, using material optical data taken from the literature [71] for GaAs, and from ellipsometry measurements for the other materials. Further model details and the resulting analytical expressions can be found in [100, 101].

The transport and collection of minority carriers are determined by the diffusion length, given by $L_\alpha = \sqrt{D_\alpha \tau_\alpha}$, where the subscript α identifies electrons (n) in the base and holes (p) in the emitter. D_α is the diffusion coefficient and τ_α is the minority carrier lifetime. The doping dependent parameters D_n and D_p were defined according to the model described by Sotoodeh et al. [68], and τ_α is calculated under low injection conditions considering both radiative and Shockley-Read-Hall (SRH) recombination as:

$$\frac{1}{\tau_\alpha} = \frac{1 - f_{PR}}{\tau_{\alpha,rad}} + \frac{1}{\tau_{\alpha,SRH}} \tag{6.1}$$

where the radiative lifetime is given as $\tau_{\alpha,rad} = 1/BN_{AB(DE)}$, B being the microscopic radiative recombination rate of the semiconductor, and N_{AB}, N_{DE} the acceptor and donor doping density in the base and emitter. For the sake of thermodynamic consistency, the coefficient B is calculated by integrating the spontaneous emission rate associated with the GaAs absorption profile used in the CPS and is found to be $6.22\text{x}10^{-10}$ cm^3/s. Photon recycling is modeled through the photon recycling factor f_{PR}, calculated according to the model reported by Steiner et al. [19]. For the solar cells in this study the calculated f_{PR} ranges from approximately 0.78 for the substrate based cells to 0.93 for the thin-film devices. Finally, $\tau_{\alpha,SRH}$ characterizes the non-radiative recombination lifetime.

After de-embedding the possible influence of the parasitic series and shunt resistances, the dark $J-V$ characteristic (J_{dark}) of the solar cell can be modeled by two diodes in parallel [45]:

$$J_{dark} = J_{01}\left(e^{\frac{qV}{k\mathrm{T}}} - 1\right) + J_{02}\left(e^{\frac{qV}{2k\mathrm{T}}} - 1\right) \tag{6.2}$$

where J_{01} and J_{02} are the reverse saturation current densities of the $1kT$ and $2kT$ components, respectively, and q, k, and T the electron charge, Boltzmann constant and temperature. The ratio between the two components of the dark current is voltage dependent, with non-radiative recombination in the perimeter of the cell and in the space-charge region dominating at low voltages (the $2kT$ region) and recombination in the quasi-neutral regions (QNR) dominating at higher voltages (the $1kT$ region). According to the junction diffusion theory, J_{01} arises from the bulk and interface recombination of minority carriers in the base and emitter QNR regions [100] and is given by:

$$J_{01} = J_{01,E} + J_{01,B} \tag{6.3a}$$

with each component given by:

$$J_{01,E} = \frac{qD_p n_{i,E}^2}{L_p N_{DE}} \times \frac{\sinh\frac{d_E}{L_p} + \frac{S_p L_p}{D_p}\cosh\frac{d_E}{L_p}}{\cosh\frac{d_E}{L_p} + \frac{S_p L_p}{D_p}\sinh\frac{d_E}{L_p}} \tag{6.3b}$$

and

$$J_{01,B} = \frac{qD_n n_{i,B}^2}{L_n N_{AB}} \times \frac{\sinh\frac{d_B}{L_n} + \frac{S_n L_n}{D_n}\cosh\frac{d_B}{L_n}}{\cosh\frac{d_B}{L_n} + \frac{S_n L_n}{D_n}\sinh\frac{d_B}{L_n}}, \tag{6.3c}$$

where d_B and d_E are the thickness of the QNR of the base and emitter with intrinsic carrier density $n_{i,B}^2$ and $n_{i,E}^2$, respectively. The intrinsic carrier density is computed taking into account the bandgap narrowing effect in the highly doped regions. In particular, the bandgap narrowing significantly affects the QNR recombination current in the highly doped base and emitter layer of the DJ and SJ cells, respectively. We have assumed bandgap shrinkage $\Delta E_g \approx 2\text{x}10^{-11} N_{AB}^{1/2}$ eV for p-type GaAs [102] and $\Delta E_g \approx 2\text{x}10^{-8} N_{DE}^{1/3}$ for n-type GaAs [103]. The J_{02} dark current component involves non radiative recombination mechanisms in the space charge region that can usually be modelled according to the Shockley-Read-Hall theory [101, 104], with analytical or semi-analytical formulations available under the assumption of a single mid-gap defect level [104] and for the more realistic case of multiple trap levels [95].

6.3 Results and Discussion

6.3.1 Overview of the performance at BOL and upon irradiation

The average photovoltaic cell parameters measured at BOL for the different device architectures are reported in table 6.2 and compared with the simulated values. When corrected to the active area, the solar cells present efficiencies close to 25% under AM1.5G, and close to 21.5 % under AM0 (1367 W/m^2 at 28^{o}C). The produced thin-film solar cells mounted on a metal foil present a specific power above 1200 W/kg, and when combined with light weight mounting systems and flexible protective coatings for space application they show the potential to reach a module specific power above 400 W/kg [58].

Table 6.2: Measured and simulated BOL values for J_{sc} and V_{oc} of the different solar cell geometries.

Solar cell	J_{sc} [mA/cm^2]		V_{oc} [V]	
geometry	Measured	Simulated	Measured	Simulated
SB-SJ	28.1	28.1	1.053	1.053
SB-DJ	27.3	28.3	1.070	1.058
TF-SJ	24.5	24.5	0.996	0.996
TF-DJ	24.3	25.1	1.043	1.042
TF-DJ$_{1400nm}$	24.3	24.1	1.035	1.035

In order to identify the four model parameters S_p, S_n, τ_p, and τ_n before and after irradiation, EQE spectra, illuminated and dark $J-V$ parameters at BOL and upon irradiation were considered. The parameter extraction procedure emphasizes the fitting of the average photovoltaic parameters ensuring at the same time a good correlation with the measured EQE spectra and dark $J-V$ of single representative samples. The modeled BOL values of both the short circuit current (J_{sc}) and the open circuit voltage (V_{oc}) reported in table 6.2 are very representative of the measured values and indicate a good quality of the epitaxial layers. The measured V_{oc} values are all within 1% of the simulated values, and a slightly larger variation is seen for the J_{sc}, probably due to a non-perfect deposition of the ARC layers, that can directly affect the experimentally obtained current. Note that the J_{sc} values of the TF cells are significantly lower than that of the SB cells because their grid coverage is much higher. When J_{sc} is corrected for the effective exposed area, the values are comparable.

The effect that the electron irradiation has on the illuminated $J-V$ parameters is expressed in terms of the remaining factor with respect to the BOL values, defined as $Parameter/Parameter_{BOL}$. The average experimentally determined remaining factors from J_{sc} and Voc are shown in figures 6.4a and 6.4b, respectively. It is clear that the J_{sc} of both thin-film and substrate based devices with a SJ geometry show relatively small sensitivity to electron radiation damage, with EOL remaining factors above 90%. On the other hand, the cells with the DJ geometry are severely affected by the irradiation, showing EOL J_{sc} remaining factors of approximately 15% for substrate based cells, 25% for the thin-film cells and 55% for the thinner thin-film sample. The V_{oc} of the solar cells is in general less sensitive to electron radiation, presenting EOL remaining factors above 75% for all samples and above 85% for all cells with the exception of the SB - DJ cells. For fluences up to 3x10^{14} e$^-$/cm^2, usually associated with LEO missions [94], both SJ and DJ cells in the thin-film architecture clearly show less degradation of V_{oc} than the substrate-based cells.

The lines in figure 6.4 represent the CPS model fit to the experimental remaining factors. The simulated J_{sc} values agree closely with the measurements, while there is a slightly larger deviation (maximum of 2% absolute) between the simulated and measured V_{oc} remaining factor values. This can be related to the fact that illuminated $J-V$ measurements were performed with a portable solar simulator that has a less precise temperature control (with variations from 25^{o}C up to $\pm$2.5^{o}C), which will most strongly affect the V_{oc}.

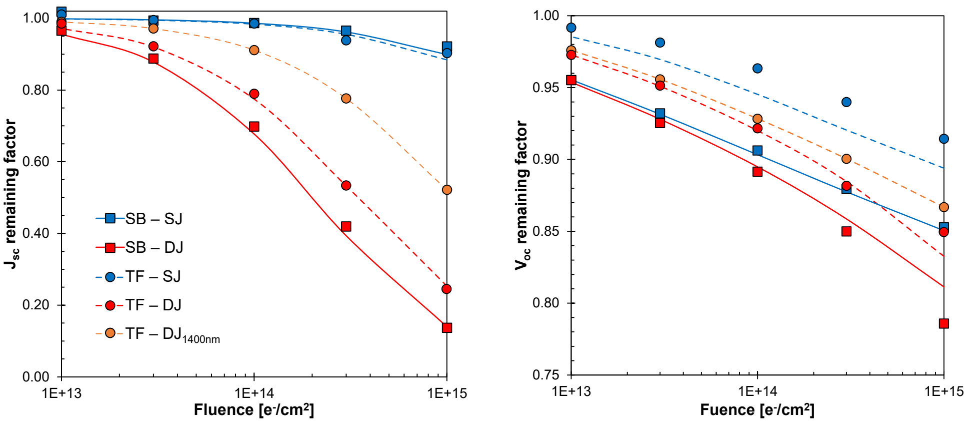

(a) **(b)**

Figure 6.4: Remaining factors of a) the J_{sc} and b) the V_{oc} of the solar cells subjected to different fluences of 1-MeV electron radiation. The markers represent the average of the measured values and the lines are the best fit of the CPS model to the experiments.

The modeled efficiency remaining factors match the measured values within 5% relative, as shown in table 6.3. The remaining efficiencies are clearly higher for SJ than for DJ cells, and are higher for both geometries in a thin-film design than when they are substrate based, since the thin-film devices are thinner. The thinner DJ sample presents an intermediate EOL efficiency remaining factor, indicating a strong influence of the solar cell thickness on the performance under electron radiation.

Table 6.4 summarizes the BOL and EOL values for the minority carriers lifetime, the diffusion length, and the surface recombination velocity at the window and BSF interfaces, as derived from the best fit of the CPS model to the average experimental BOL and the average remaining factors *vs.* fluence. As discussed in the following, the performance at BOL is well reproduced by the CPS model assuming the nominal minority carrier lifetimes calculated from equation 6.1 and accounting - whenever needed

Table 6.3: Efficiency remaining factors of the solar cells at at EOL.

Solar cell geometry	**η remaining factors:** Measured	Simulated
SB-SJ	0.79	0.75
SB-DJ	0.10	0.10
TF-SJ	0.82	0.78
TF-DJ	0.19	0.20
TF-DJ$_{1400nm}$	0.45	0.44

- for an imperfect passivation at the window and BSF interfaces. Following this approach specifically clarifies that the V_{oc} of the thin-film cells turns out to be limited by the surface recombination velocity at the base-BSF interface (S_n). Upon exposure to radiation, the minority carriers lifetime reduces (most likely due to radiation displacement defects [92–96]). Furthermore, in all solar cell structures a degradation of the emitter-window (GaAs/AlInP) and base-BSF (GaAs/InGaP) hetero-interfaces quality is identified, characterized by an increase in surface recombination velocity.

6.3.2 Analysis at BOL

The window and BSF layers are high bandgap materials that have the function of repelling minority carriers away from the surfaces of the cell, which are areas of high SRH recombination probabilities. Based on previous results of cells grown under the same conditions as in this study [45], a good quality in the growth of the hetero-interfaces GaAs/AlInP and GaAs/InGaP is assumed. Consequently, an effective surface passivation by the window and BSF layers is expected, and therefore S_p and S_n are initially considered to be negligible.

The emitter and base lifetimes were estimated at beginning of life (BOL) from equation 6.1, with SRH lifetimes given by the empirical model in Lumb et al. [20]. Under these assumptions, it turns out that at BOL the carrier lifetimes are dominated by radiative recombination in all the layers, except for the highly doped base of the deep-junction cells, where SRH and radiative recombination lifetimes are similar.

For layers with similar doping levels, such as the emitter in the DJ cells and the base in the SJ cells, L_p is smaller than L_n because the hole mobility is markedly lower than the electron mobility. The higher lifetimes observed in the TF cells with respect to the corresponding SB devices are explained by the higher photon recycling factor, and therefore higher radiative lifetime, of the TF cells. For a high collection efficiency the devices should present $d_E \ll L_p$ and $d_B \ll L_n$, and this is the case for

Table 6.4: Minority carrier lifetimes, diffusion lengths and surface recombination velocities for each solar cell configuration at BOL and EOL, as deduced from the best fits of the model to the average measured photovoltaic parameters at BOL and upon irradiation. At BOL, the values of $\tau_n(p)$ and $L_n(p)$ are the nominal ones and only S_n and S_p are used as fitting parameters. At EOL, both lifetime and surface recombination velocity are used as fitting parameters. The values presented in parentheses may be affected by a large error.

Solar cell	**BOL**						**EOL**					
geometry	τ_p [ns]	L_p [μm]	S_p [cm/s]	τ_n [ns]	L_n [μm]	S_n [cm/s]	τ_p [ns]	L_p [μm]	S_p [cm/s]	τ_n [ns]	L_n [μm]	S_n [cm/s]
SB-SJ	1.90	0.81	<100	133	43.6	360	0.71	0.50	1.7x10^4	0.19	1.65	(360)
SB-DJ	138	10.4	1.3x10^3	8.5	8.4	<100	0.57	0.67	3.6x10^4	(0.19)	(1.13)	1.3x10^7
TF-SJ	3.8	1.14	2.0x10^4	203	54.0	1.2x10^4	0.88	0.55	5.4x10^4	0.19	1.65	(1.2x10^4)
TF-DJ	346	16.5	<100	6.8	6.9	2.6x10^4	1.14	0.95	6.7x10^4	(0.19)	(2.8)	4.6x10^6
TF-DJ$_{1400nm}$	346	16.5	3x10^3	6.8	6.9	1.2x10^4	1.14	0.95	4.9x10^4	(0.19)	(1.13)	6.5x10^6

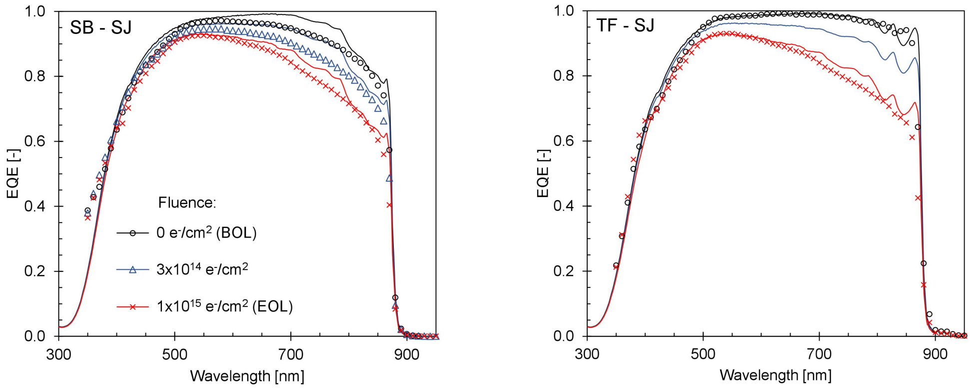

(a) **(b)**

Figure 6.5: External quantum efficiency of a) substrate based and b) thin-film solar cells with a shallow junction geometry under different levels of irradiation. The markers represent the measured data and the lines the simulation results.

all the structures, as demonstrated by the high EQE at BOL seen in figures 6.5 and 6.6 for the SJ and DJ cells, respectively. Hence, the calculated lifetimes used in the model, which are approximations for high quality materials, are justified by the high BOL efficiency of the studied devices, and in fact provide a very good fitting of the measured EQE.

In the DJ solar cells, the base is responsible for the absorption of approximately 0.2% of the photons only [45], and therefore the EQE is dominated by the emitter collection efficiency, i.e. by S_p and τ_p. From the EQE fitting, τ_p is found consistent with the expected theoretical value for all the three DJ samples, while a non negligible S_p explains the slightly lower EQE of the thinner DJ cell. On the other hand, the values of τ_n and S_n do not significantly affect the collection efficiency in the thin base and cannot be extracted from the EQE spectra. Some insight on the base parameters and on the V_{oc} degradation can be instead derived from the measured dark $J-V$ characteristics reported in figure 6.7, and in particular from the analysis of the $1kT$ dark current component. The J_{01} and J_{02} values extracted from fitting the two-diode model (equation 6.2) to the measured dark $J-V$ curves of the different cells are summarized in table 6.5.

Figure 6.8 shows the calculated values for $J_{01,B}$ and $J_{01,E}$ as a function of the minority carriers lifetime and for values of S_p and S_n varying logarithmically from 10^0 to 10^7 cm/s, for cells with a GaAs emitter-base homo-junction and layers thickness of the actual TF - SJ and DJ designs. The effect of the interface recombination velocity

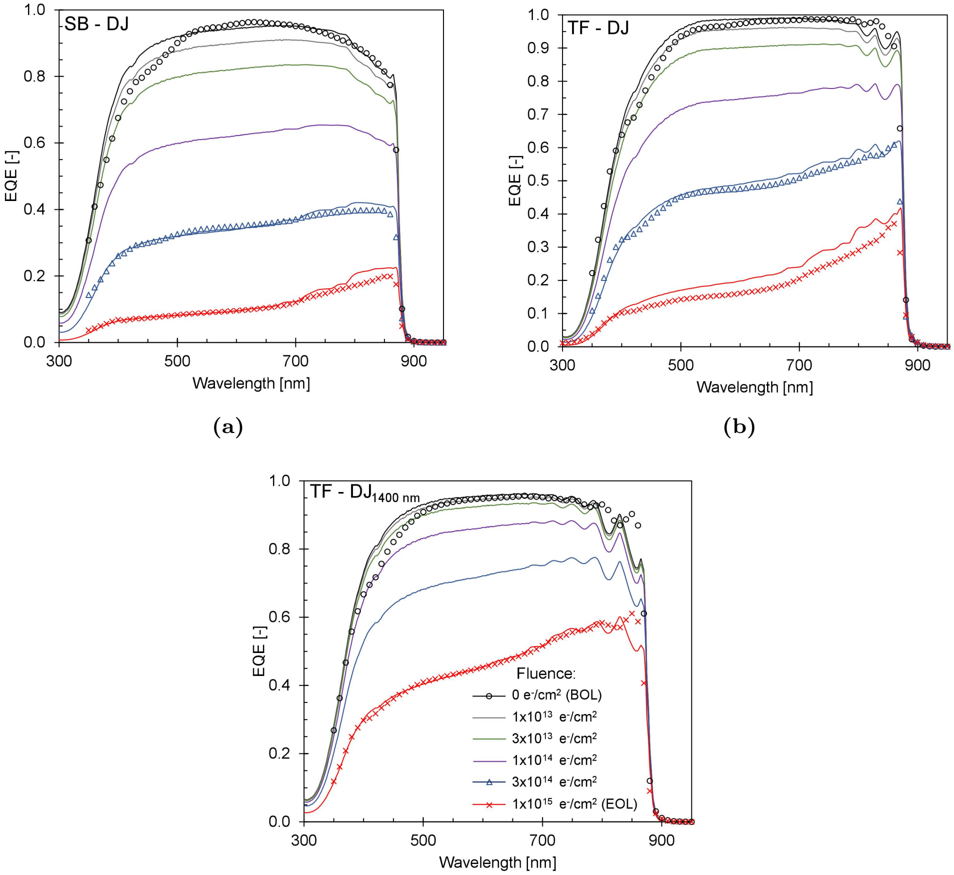

(a)

(b)

(c)

Figure 6.6: External quantum efficiency of a) the substrate based, b) the thin-film and c) the thinner thin-film solar cells with a deep junction geometry under different levels of irradiation. The markers represent the measured data and the lines the simulation results.

on J_{01} increases with the probability of carriers to reach the hetero-interfaces, being almost irrelevant in case of short lifetimes and more pronounced for thin layers. In the limit of thick QNR ($L_{p(n)} \ll d_{E(B)}$), J_{01} is dominated by bulk recombination and equations 6.3a-6.3c reduce to the classical Shockley equation:

$$J_{01} = J_{01,E} + J_{01,B} = \frac{qD_p n_{i,E}^2}{L_p N_{DE}} + \frac{qD_n n_{i,B}^2}{L_n N_{AB}} \tag{6.4}$$

whereas for thin QNR ($L_{p(n)} \gg d_{E(B)}$), J_{01} is dominated by surface recombination and equations 6.3a–6.3c reduce to

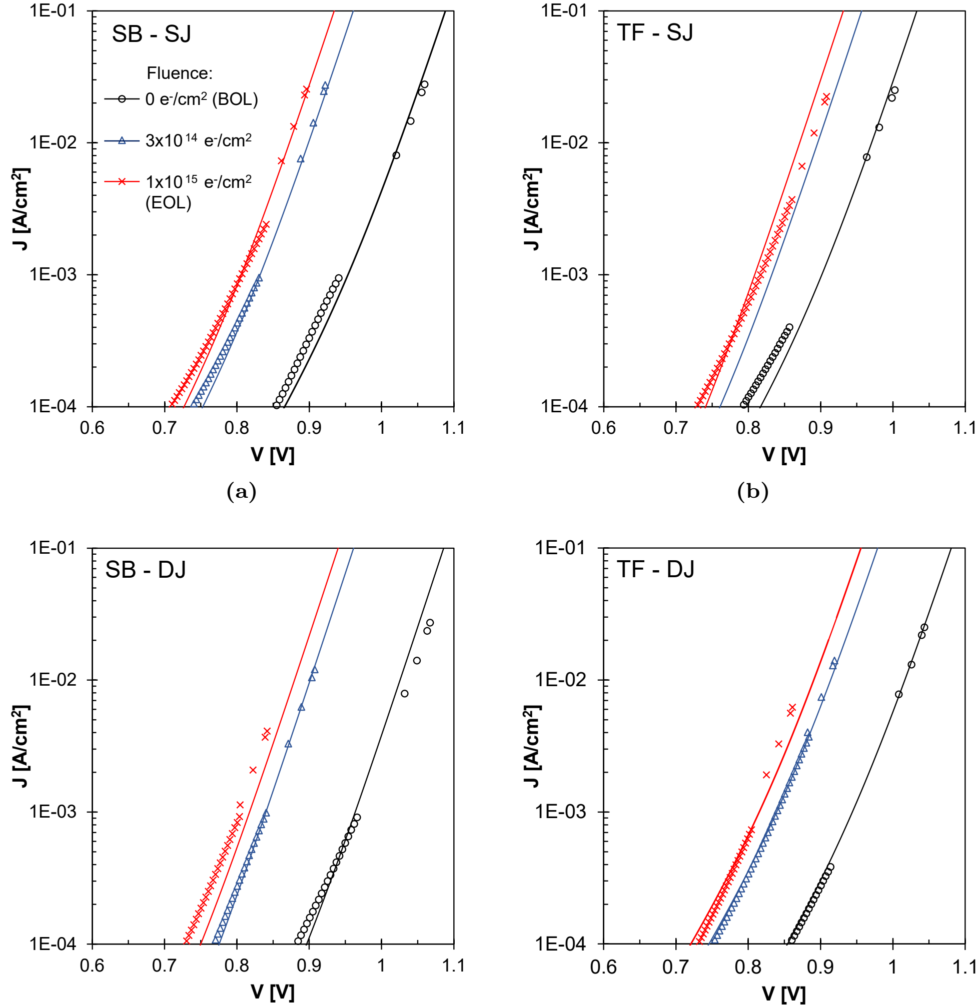

(a) (b)

(c) (d)

Figure 6.7: Dark current-voltage characteristics of a) the substrate based shallow junction, b) the thin-film shallow junction, c) the substrate based deep junction and d) the thin-film deep junction solar cells after different levels of 1-MeV electron irradiation. Note that the upper four data points were obtained using J_{sc} - V_{oc} pairs at different illumination intensities. The markers represent the measured data and the solid lines the two-diode model with J_{01} calculated from the CPS model.

Table 6.5: Saturation current densities J_{01} and J_{02} deduced from the dark $J-V$ curves of the various cell geometries using the two-diode model.

Fluence [e$^-$/cm^2]		SB-SJ	SB-DJ	TF-SJ	TF-DJ	TF-DJ$_{1400nm}$
0	J_{01} [A/cm^2]	4.0x10^{-20}	3.5x10^{-20}	3.0x10^{-19}	7.0x10^{-20}	–
(BOL)	J_{02} [A/cm^2]	3.0x10^{-12}	1.1x10^{-12}	1.2x10^{-11}	4.0x10^{-12}	–
3x10^{14}	J_{01} [A/cm^2]	8.0x10^{-18}	6.9x10^{-18}	–	5.0x10^{-18}	–
	J_{02} [A/cm^2]	2.5x10^{-11}	8.8x10^{-12}	–	3.8x10^{-11}	–
1x10^{15}	J_{01} [A/cm^2]	2.3x10^{-17}	2.7x10^{-17}	1.2x10^{-17}	2.6x10^{-17}	2.0x10^{-17}
(EOL)	J_{02} [A/cm^2]	4.2x10^{-11}	2.1x10^{-11}	2.6x10^{-11}	5.3x10^{-11}	6.4x10^{-11}

$$J_{01} = J_{01,E} + J_{01,B} = \frac{qn_{i,E}^2 D_p}{N_{DE}} \frac{S_p}{D_p + S_p d_E} + \frac{qn_{i,B}^2 D_n}{N_{AB}} \frac{S_n}{D_n + S_n d_B}. \tag{6.5}$$

The SJ design presents a strongly asymmetric doping ($N_{DE}/N_{AB} = 100$), and therefore the base dark current component tends to be highly dominant (figure 6.8a). On the other hand, in the DJ design ($N_{AB}/N_{DE} = 20$) the emitter and base dark current components provide more similar contributions (figure 6.8b).

Using the values of τ_p and S_p deduced from the EQE measurements of the DJ solar cells, the $J_{01,E}$ component (equation 6.3b) is about one fifth of the J_{01} value extracted from the two-diode fitting (equation 6.2, table 6.5). This indicates a significant contribution to J_{01} from the base layer. In fact, as can be verified in figure 6.8b, matching the measured value requires the assumption of a very short lifetime of electrons in the base ($\tau_n \approx 0.3$ ns if $S_n \leq 10^3$ cm/s) or, the more realistic alternative adopted here, a non-negligible surface recombination S_n on the order of 3×10^4 cm/s if one considers for τ_n the nominal BOL value of a few ns.

It is worth noticing that in the case of the SB - DJ cells, which have an InGaP ($E_g \approx 1.8$ eV) base layer, the dark current contribution from the base QNR is expected to be negligible with respect to that of the emitter QNR, regardless of the electron lifetime and surface recombination velocity. On the other hand, the measured data indicate, already at BOL, an unexpected high recombination current with unitary ideality factor. In the context of this work, such high current has been accounted for by modeling the InGaP base layer with a fictitiously high intrinsic carrier density, of the same order of that of GaAs. In this respect, further investigation on the GaAs-InGaP emitter-base heterojunction and the associated interface recombination mechanisms is needed.

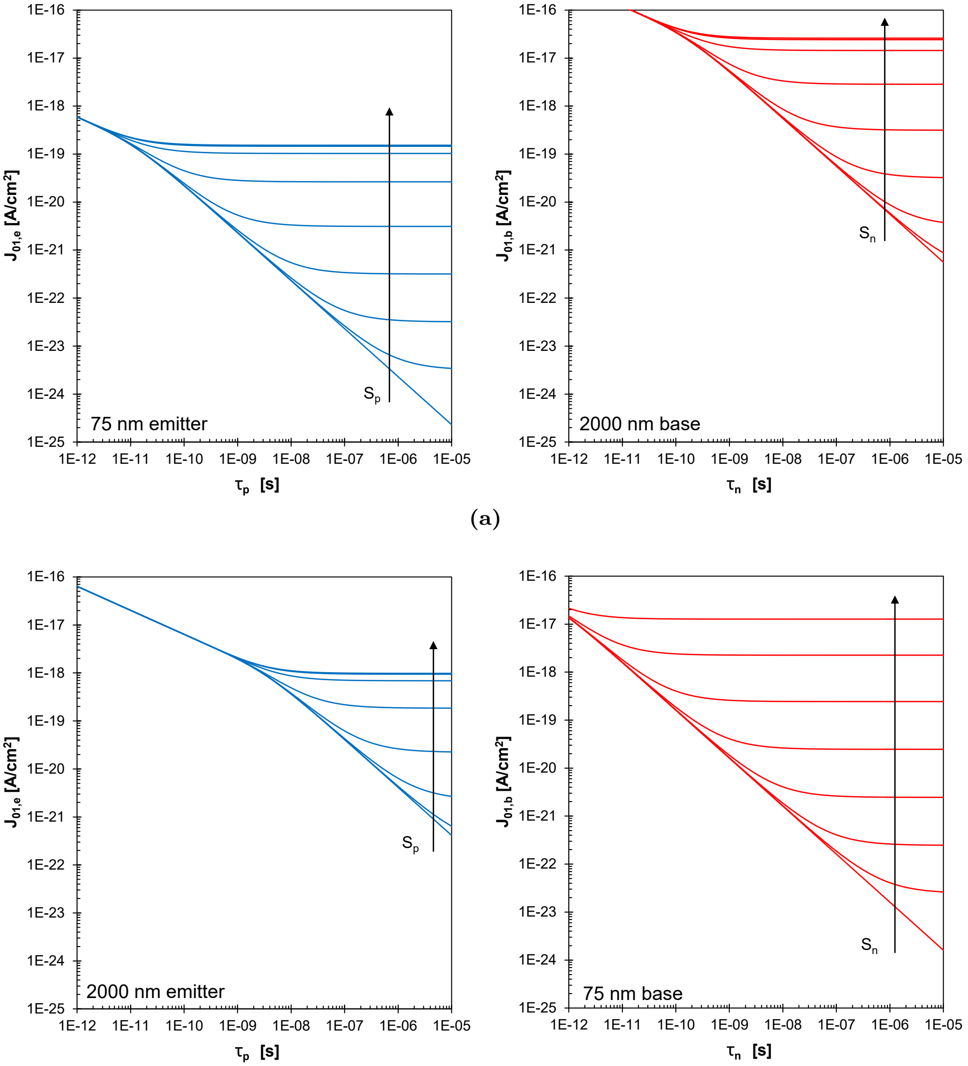

(a)

(b)

Figure 6.8: Analysis of the dependence of the saturation current density components in the emitter (left) and base (right) for a) a thin-film shallow junction cell and b) a thin-film deep junction cell as a function of minority carrier lifetime for different values of interface recombination velocities. S_p and S_n scale logarithmically from 10^0 to 10^7 cm/s in the direction of the arrow.

Concerning the SJ cells, both the QNRs and the depletion region give substantial contribution to the spectral photocurrent, which shows a large resilience to low carrier lifetimes and high interface recombination velocities. In particular, the EQE in the region around 650 nm is hardly affected by τ_α and S_α, being sustained by the depletion region. Based on the applied theoretical emitter minority carrier lifetimes reported in table 6.4, there is a good match between the modeled and experimental EQE in the short wavelength range. On the other hand, however, solely based on EQE, it is not possible to accurately determine τ_n and S_n. As in the DJ case, this can be resolved to some extent by studying the J_{01} component around V_{oc}, which is dominated by recombination in the base QNR. The SB - SJ cells show a low J_{01} ($\approx 4\times10^{-20}$ A/cm^2), coherently with the high theoretical τ_n value of about 100 ns and a low S_n on the order of few hundreds of cm/s. In contrast, the TF - SJ cells show a significantly higher J_{01} ($\approx 3 \times 10^{-19}$ A/cm^2) that is attributed to an S_n comparatively higher than that of the SB structure, as also observed for the DJ cells.

Overall, it turns out that in both DJ and SJ geometries τ_p and S_p are the predominant factors affecting the EQE at BOL, while τ_n and S_n mainly influence the V_{oc} through the recombination current in the p-type QNR region.

6.3.3 Analysis of bulk and interface radiation damage

In order to simulate the cell performance after intermediate electron irradiation doses, the decrease of the SRH lifetime $\tau_{\alpha,SRH}$ with radiation is modeled as:

$$\frac{1}{\tau_{\alpha,SRH}} = \frac{1}{\tau_{\alpha,SRH0}} + K_{\tau_\alpha}\phi, \tag{6.6}$$

where $\tau_{\alpha,SRH0}$ is the SRH lifetime at BOL, K_{τ_α} is the minority carrier lifetime damage constant and ϕ is the 1-MeV electron fluence. The lifetime damage constant K_{τ_α} is expected to be material dependent and is fitted in the model within a range of values consistent with those reported in the literature [89, 105]. In order to explain the observed changes in the spectral response and dark I-V upon irradiation, we had to postulate an increase of the surface recombination velocity at the window and BSF hetero-interfaces. This points out a degradation of the interface quality possibly due to radiation induced defect states. The degradation of S_p and S_n is considered to be linearly dependent on the fluence, and expressed by:

$$S_\alpha = S_{\alpha(BOL)} + K_{S_\alpha}\phi \tag{6.7}$$

where $S_{\alpha(BOL)}$ is the value of S_α at BOL and K_{S_α} is the interface damage rate, deduced from the best CPS model fit to the experimental data. The EQE, illuminated and dark $J - V$ measurements from the five studied structures are simultaneously taken in consideration in order to obtain a consistent fit value for K_{τ_α} and K_{S_α}.

The degradation mechanism of the J_{sc} of the solar cells under irradiation can be understood from the analysis of the measured EQE curves, shown in figures 6.5 and 6.6 together with the simulated curves for different irradiation doses. Upon irradiation, the displacement damage creates electron and hole traps throughout the solar cell structure, increasing SRH recombination rates and therefore reducing the average lifetime and diffusion length of the minority carriers [92–96]. The difference in degradation behavior between the SJ and DJ cells is related to the fact that the transmission of light into the cell decreases exponentially, so that by far the largest fraction of light is absorbed at the upper part of the cell.

In the SJ cells, most of the photogenerated free carriers, therefore, only have to diffuse over a short distance to the $p - n$ junction to be drifted towards the right electrode and be collected. This is particularly true for carriers generated by short wavelength light. For longer wavelengths a smaller fraction of the light is able to penetrate deeper into the cell and consequently generates some minority carriers deeper in the base, which have to travel further before reaching the $p-n$ junction. Therefore, the short wavelength photocurrent is mostly sustained by the thin emitter, whereas most of the long wavelength photocurrent is supported by the thick base. Electrons generated deeper in the thick base of SJ devices suffer more from the enhanced SRH recombination probability, as shown by the reduced EQE at longer wavelengths (see figure 6.5). Based on the EQE analysis, the modelled degradation of τ_p and S_p is well correlated to the penalty observed in the short wavelength region, while the degradation of τ_n explains the penalty observed in the long wavelength region. Finally, the correlation between the simulations and measured EQE show that after irradiation there is a decrease in the contribution from the depletion region to the EQE, which might indicate a reduction of the depletion region thickness. This can be related, for example, to a strong change of the equilibrium carrier density in the base [106], but a more detailed investigation to verify this assumption is required.

Differently from the SJ cells, in DJ cells all the minority carriers photogenerated in the emitter (except for the small fraction generated deeper in the cell) have to diffuse over a long distance before reaching the $p - n$ junction. Therefore, the degradation of τ_p and S_p in the emitter reduces the collection efficiency over the entire wavelength range in the DJ cell (see figure 6.6), resulting in a significant reduction of J_{sc}, whereas the impact of the base parameters is restricted to the longer wavelength region and turns out to be completely marginal. In fact, the significant asymmetry of the spectral response between the short and the long wavelength ranges observed for the DJ cells after irradiation can only be correctly modeled if an increased S_p is assumed, supporting the approach described in equation 6.7.

In summary, the EQE upon irradiation is influenced mainly by the lifetime in the emitter for DJ cells and by the lifetime in both emitter and base for SJ cells. Moreover, the observed increase in S_p in both SJ and DJ cells upon irradiation indicates a degradation in the emitter-window hetero-interface quality.

The study of the dark $J-V$ characteristics upon irradiation (see figure 6.7) provides further insight especially for the base parameters in the DJ cells. In fact, the observed increase of J_{01} in the DJ cells can only be explained by a significant increase of the recombination current component in the thin base. This in turn calls for an unusually high damage rate (K_{τ_n}), about two orders of magnitude higher than what is commonly reported in the literature [89, 105]. Considering a more realistic value of K_{τ_n} (in the 10^{-6} cm^2/s range) implies that the base surface recombination velocity S_n has also a non-negligible value that increases with irradiation. For all the DJ configurations, the extracted J_{01} values could be explained by S_n values higher than 10^6 cm/s at EOL, suggesting a significant degradation at the base-BSF interface. Such a high S_n also implies that $J_{01,B}$ is dominated by S_n for cells with the DJ geometry, as can be observed in figure 6.8, and is quite insensitive to τ_n as long as the L_n/d_B ratio remains higher than one. Therefore the electron lifetime cannot be reliably extracted.

In order to determine the damage rates, an approach was taken in which initially K_{τ_p} and K_{τ_n} were assumed to be the same for all configurations and then adjusted by closely fitting the model outcomes to the measured EQE, average illuminated $J-V$ parameters and dark $J-V$ curves. The fitted EOL values for τ_α, L_α and S_α resulting from this approach are depicted in the right portion of table 6.4. Because the depletion region in the DJ solar cells is much closer to the base-BSF hetero-interface, the increase in S_n is the limiting mechanism to the performance for this geometry, rather than the decrease in τ_n, and the values for K_{τ_n} cannot be deduced. Therefore, the τ_n values shown in table 6.4 for the DJ cell are set equal to those extracted from the analysis of the SJ cells. Conversely, in the SJ solar cells the junction distance to the rear interface is so large that the increase in S_n is hardly relevant to the performance, and therefore the values for K_{S_n} cannot be determined. The extracted values of K_{τ_p}, K_{τ_n}, K_{S_p} and K_{S_n} for the various cell geometries under study are stated in table 6.6.

The hypothesis of a linear dependence of the recombination velocities with irradiation fluence provides a very good agreement between measured and simulated values of J_{sc}, V_{oc} and η for the whole fluence range, as seen from the detailed comparison of measured and simulated data in figure 6.4 and in table 6.3. Overall, the observed degradation of the solar cells performance upon irradiation is satisfactorily simulated

Table 6.6: Values for the radiation induced damage rates deduced from the $J-V$ and EQE measurements of the cells.

Solar cell geometry	**Damage rates**			
	K_{τ_p} [cm^2/s]	K_{τ_n} [cm^2/s]	K_{S_p} [cm^3/s]	K_{S_n} [cm^3/s]
SB - SJ	8.75x10^{-7}	5.25x10^{-6}	1.7x10^{-11}	–
SB - DJ	1.75x10^{-6}	–	3.5x10^{-11}	1.3x10^{-8}
TF - SJ	8.75x10^{-7}	5.25x10^{-6}	3.4x10^{-11}	–
TF - DJ	8.75x10^{-7}	–	6.7x10^{-11}	4.6x10^{-9}
TF - DJ$_{1400nm}$	8.75x10^{-7}	–	4.6x10^{-11}	6.6x10^{-9}

assuming similar lifetime damage rates for electrons and holes for all the solar cells architectures, indicating that the material radiation damage is probably not affected by the device geometry or the fabrication steps. The identified values for the lifetime damage constant of minority electrons and holes are in good agreement with previous studies [89, 105]. In particular, taking into account the carriers' diffusivity, the ratio K_{τ_n}/K_{τ_p} corresponds to a ratio in terms of diffusion length damage constant of about one tenth, inferring a damage rate for the diffusion length in n-type GaAs about ten times larger than that one in p-type GaAs, as theoretically predicted by Yamaguchi et al. [89].

The thickness of the active layers and the position of the depletion region are shown to be the determinant parameters with regards to the radiation resistance of the cells. Thin-film devices present the big advantage of having a back reflector that allows the thickness of the active layers to be significantly reduced. Therefore, a shallow junction solar cell processed into a thin-film geometry is found to be the best structure for space applications. The MOCVD growth of hetero-interfaces such as GaAs/AlInP and GaAs/InGaP has been shown to be a challenge in the past [77–80]. A meticulous control of chemical composition, material inter-diffusion and surface segregation is necessary in order to prevent the formation of mixed compounds that reduce the abruptness of the interfaces. The fact that interface recombination velocity is affected by irradiation indicates that it is an important aspect to be optimized, with the potential to further increase the resilience of the TF - SJ devices under irradiation.

6.4 Conclusions

A combined experimental and theoretical analysis of the performance of GaAs solar cells upon electron radiation exposure is presented. In order to deduce the important cell parameters, five different solar cells architectures were applied, and the environment the cells would face in GEO and LEO space missions was simulated by subjecting the devices to electron fluences up to $1\text{x}10^{15}$ e^{-}/cm^{2}.

The GaAs minority carriers' lifetime damage constants reported in the literature, required for a proper prediction of the cells performance in space application, differ significantly. In this study, by simultaneously analyzing the performance of the five different cells geometries, a coherent set of lifetime damage constants could be derived. The damage constants are found to be material dependent and insensitive to the device geometry or fabrication steps. The incidence of electrons introduces lattice defects in the cells that act as recombination centers, directly impacting carrier lifetimes. Because for the DJ cells at EOL the hole diffusion length is smaller than the emitter thickness, the collection of generated carriers is strongly reduced, and this geometry presents a much larger decrease of J_{sc} when compared to SJ devices. Therefore, we find that DJ cells in the present configuration are not suited for space application.

Most importantly, however, the modeling study has pointed out that besides the reduction of the lifetime of the carriers, the electron irradiation strongly affects the quality of hetero-interfaces, characterized by a linear increase in the interface recombination velocity. The current study shows that the degradation of the window-emitter and base-BSF hetero-interfaces quality is responsible for a significant increase of the diffusion component of the dark current, and consequently for the reduction of V_{oc}. Therefore, it is a critical aspect which deserves further investigation since it can become the bottleneck for the optimization of the cell radiation tolerance.

A shallow junction solar cell processed into a thin-film geometry is found to be the best structure for space applications, presenting an EOL average efficiency that is 82% of the BOL value. The presence of a rear reflector in the thin-film geometry allows the design of thinner devices that show the potential to further increase the BOL performance and the resilience under irradiation, provided that the interface radiation hardness can also be improved.

Acknowledgements

The authors would like to thank the support from Marinus Hom of the RID during the performance of the irradiation tests. The authors acknowledge financial support from the Brazilian National Council for Scientific and Technological Development, under the program Science Without Border, project 233259/2014-7, and from the European Union's Horizon 2020 research and innovation program, under grant agreement 687253 TFQD (http://tfqd.eu).

Chapter 7

Proton radiation induced degradation of GaAs solar cells[1]

Abstract

The effects of proton irradiation on the performance of GaAs solar cells with different designs are studied. Solar cells with the same active layers thicknesses but with either a shallow or a deep junction, processed on the native wafer as well as into thin-film devices, were irradiated by 1-MeV protons with fluences up to 5x10^{12} H^+/cm^2. The degradation of the cell parameters due to irradiation was studied experimentally and theoretically, using physical models in order to describe the solar cell working mechanisms. The degradation of the solar cells performance primarily depends on the junction depth and the thickness of the active layers, and is insensitive to the cell architecture and fabrication steps. A coherent set of minority carriers lifetime degradation constants is derived, based on previously reported electron irradiation data, resulting in a good correlation between simulated and experimental results. These results show that, by using this method, performance predictions of a range of solar cell architectures subjected to different particle fluences can be made, provided the material thickness and doping levels are known.

---

[1] The work presented in this section is based on ”Proton radiation induced degradation of GaAs solar cells”, by N. Gruginskie, G. Bauhuis, P. Mulder, E. Vlieg and J.J. Schermer. *In preparation.*

7.1 Introduction

Most of the space solar power applications are directed towards comunication satellites operating in Geostationary Earth Orbits (GEO) or in satellite constellations in Low Earth Orbits (LEO) [10]. New advances in satellite technology, such as elliptical orbits that partially operate in the vicinity of the Van Allen radiation belt, require the understanding of solar cell degradation upon higher levels of radiation exposure [94].

Electron irradiation is the most commonly studied characterization method to replicate the space environment [56, 92, 93, 97, 107–109]. Using this method, a predefined equivalent irradiation dose of 1-MeV electrons is used to simulate the displacement damage from electrons, protons, ions and neutrons of different energies throughout the entire mission. The displacement damage dose (DDD) usually associated to GEO missions is achieved with 1x10^{15} 1-MeV electrons/cm^2, while 5 to 10 times lower doses are required for the simulation of LEO missions. Proton irradiation is a less used characterization method, and the equivalent doses are not as well defined.

It has been established that the degradation of the solar cells short circuit current density (J_{sc}) upon irradiation depends primarily on the DDD, while the impact of radiation on other cell parameters such as the non-radiative recombination in the space charge region and the open circuit voltage (V_{oc}) is dependent on the particle type. As compared to electrons, protons have shown to cause relatively higher damage in GaAs solar cells V_{oc} and have a very irregular damage profile for lower energy particles [96, 110].

In this study we systematically evaluate the effect that 1-MeV proton irradiation exposure has on GaAs solar cells with different architectures but comparable thicknesses and beginning of life (BOL) performances. For that, substrate based and thin-film devices with different junction depths were subjected to fluences up to 5x10^{12} 1-MeV H$^+$/cm^2, and their performances were theoretically modeled. The conversion of previously reported electron irradiation degradation constants, based on the particle equivalent DDD, resulted in a good representation of the experimentally obtained illuminated $J-V$, dark $J-V$ and external quantum efficiency (EQE) curves. Furthermore, a reported voltage-dependency of the photocurrent [94] is seen in the irradiated cells.

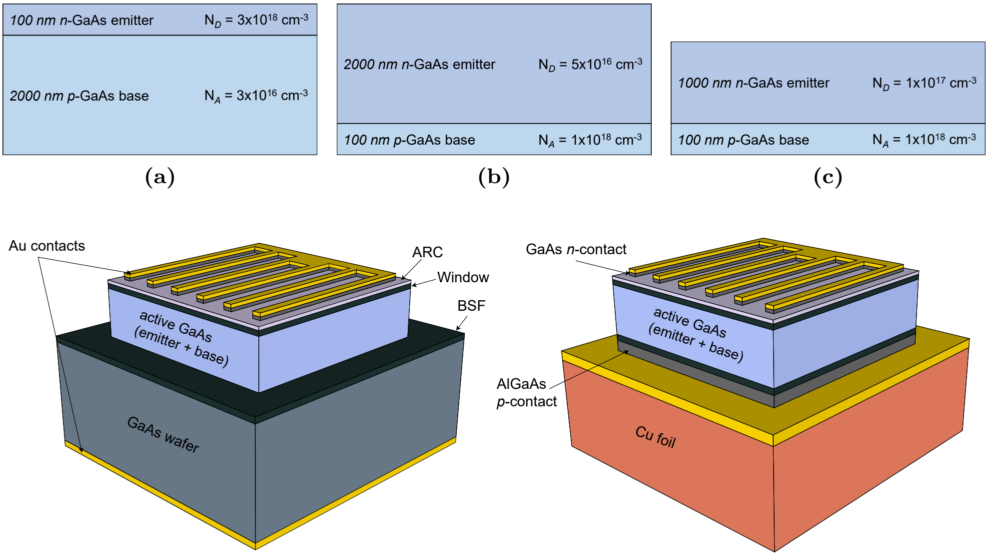

(a) **(b)** **(c)**

(d) **(e)**

Figure 7.1: Schematic depiction of a) the shallow junction, b) the deep junction and c) the thinner deep junction active layers thicknesses and acceptor and donor doping densities (N_A and N_D), and a representation of the solar cell structures processed into d) substrate based (SB) and e) thin-film (TF) devices.

7.2 Methods

7.2.1 Experimental Techniques

All solar cells used in this study were grown by low-pressure MOCVD on 2 inch diameter GaAs wafers with (1 0 0) 2^o off to (1 1 0) orientation. The structures consist of solar cells with either a thin n-doped emitter and a thick p-doped base, here called shallow junction (SJ) geometry, or a thick n-doped emitter and a thin p-doped base, here called deep junction (DJ) geometry. In order to evaluate the effect of irradiation on solar cells with reduced thickness, thinner DJ devices were also produced. Schematic depictions of the studied cell structures are shown in figures 7.1a-c, indicating the cells active layers thickness and acceptor and donor doping densities (N_A and N_D). Additionally, all structures have a 20 nm AlInP window and 100 nm InGaP back surface field (BSF) on the top and bottom of the active layers. The top most layer in all cells consists of a 300 nm n-GaAs contact, which provides low resistance ohmic contact.

The cells were processed either in the substrate-based form (SB) or into thin-film (TF) devices. For the thin-film solar cells, the first grown layer consists of an etch-stop AlGaInP layer, in order to limit the etching of the wafer, followed by a *p*-AlGaAs contact layer. The wafer was removed with an aqueous citric acid and hydrogen peroxide solution (5:1 in volume) and the etch-stop layer was removed in HCl 37%. A 200 nm thick Au rear contact/mirror was e-beam evaporated onto the rear side of the cell, and the structures were mounted on a copper foil that acts as a conductive foreign carrier. In the substrate-based devices, the back contact consists solely of 100 nm thick e-beam evaporated Au.

The cells all have 200 nm thick Au e-beam evaporated front contacts that cover 16.6% of the cell area. The 5x5 mm^2 individual cells were defined by a MESA etch using an ammonia:hydrogen peroxide solution for the GaAs layers and either an HBr:Br$_2$:H$_2$O solution (for the thin-film cells) or HCl 37% (for the substrate based cells) for the phosphide layers. The *n*-GaAs contact layer between the grid fingers was removed also using an ammonia:hydrogen peroxide solution. Finally, an anti-reflection coating (ARC) consisting of 44 nm ZnS and 94 nm MgF$_2$ was thermally evaporated on the top surface of all cells. A schematic depiction of the processed substrate based and thin-film devices is shown in figures 7.1d and 7.1e.

From each 2 inch wafer, 38 regular solar cells and 6 cells with an open grid dedicated for optical characterization were fabricated. The latter cells, instead of a grid, only have a contact frame at the outer edge of the front surface. The wafers were cleaved in quarters consisting of 11 solar cells (see figure 7.2) to be subjected to a specific radiation dose. The samples were exposed to proton fluences of 5x10^{10}, 2x10^{11}, 5x10^{11}, 2x10^{12} and 5x10^{12} H$^+$/cm^2 of 1-MeV radiation, performed at the Center of Nuclear Science and Materials Science (CSNSM) of Paris-Sud University with a Van der Graaf accelerator. The used proton flux is equal to 1x10^9 H$^+$/cm^{2}s for the lower two doses and 1x10^{10} H$^+$/cm^{2}s for the higher three doses.

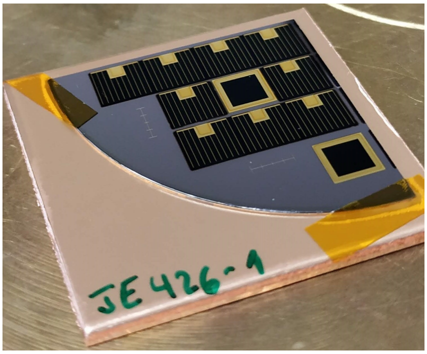

Figure 7.2: Example of one quadrant of a 2-inch wafer containing multiple 5x5 mm^2 solar cells to be subjected to a specific radiation dose.

Illuminated $J - V$, dark $J - V$ and External Quantum Efficiency (EQE) characteristics were measured before and after exposure to radiation. Illuminated and dark $J - V$ characterization of the solar cells were performed using an ABET Technologies Sun 2000 Class AAA solar simulator set-up, equipped with a Keithley 2601B source meter, and ReRa Tracer3 software for data acquisition. The solar cells were kept at 25°C during measurement using a heating/cooling water thermostat and a Pt100 temperature sensor. The light intensity was set and corrected using an NREL calibrated reference cell before each measurement series. Because at higher voltages the series resistances cause the dark curve to bend downwards, a set of $J_{sc} - V_{oc}$ data points measured under different light intensities was used in the dark characteristics analysis, as the series resistance is excluded under these conditions [45]. EQE measurements were performed with a ReRa SpeQuest Quantum Effciency system. The system uses both a Xenon and Halogen light source to address all wavelengths present in the solar spectrum, a monochromator to generate quasi-monochromatic light and a chopper for intensity modulation.

7.2.2 Device modeling

A combination of models reported in the literature [19, 20, 68, 100, 101] was used in order to simulate the different optical and electronic mechanisms of the solar cells. The minority carriers diffusion lengths are calculated by $L_{p(n)} = \sqrt{D_{p(n)}\tau_{p(n)}}$, whith the substcripts p and n representing holes in the emitter or electrons in the base. $D_{p(n)}$ is the diffusion coefficient, defined according to the empirical model described by Sotoodeh et al. [68]. The minority carrier lifetime $\tau_{p(n)}$ is determined considering both radiative and Shockley-Read-Hall (SRH) recombination, using [20]:

$$\frac{1}{\tau_{p(n)}} = \frac{1 - f_{PR}}{\tau_{p(n)_{rad}}} + \frac{1}{\tau_{p(n)_{SRH}}}. \tag{7.1}$$

where the radiative lifetime is given as $\tau_{p(n)_{rad}} = 1/BN_{D(A)}$, with N_D and N_A the donor doping density in the emitter and acceptor doping density in the base. The semiconductor microscopic radiative recombination coefficient (B) is calculated, for thermodynamic consistency, by integrating the spontaneous emission rate associated with the GaAs absorption profile, and is found to be 6.22x10^{-10} cm^3/s. The photon recycling factor (f_{PR}) is defined according to the model reported by Steiner et al. [19] using the optical data from the literature [70, 71] for GaAs and AlGaAs, and from elipsometry measurements for the other materials applied in the cell structures. The Shockley-Read-Hall (SRH) recombination $\tau_{p(n)_{SRH}}$ is determined according to the empirical model from Lumb et al. [20].

The solar cells' dark currents were initially analyzed as two diodes in parallel, which after de-embedding the possible influence of the parasitic series and shunt resistances, can be expressed as:

$$J_{dark} = J_{01}\left(e^{\frac{qV}{kT}} - 1\right) + J_{02}\left(e^{\frac{qV}{2kT}} - 1\right), \tag{7.2}$$

where q is the electron charge, k is the Boltzmann constant, T is the temperature and J_{01} and J_{02} are the saturation current densities at the $1kT$ and $2kT$ components of the curve, respectively. At higher voltages, the dark curve is dominated by J_{01}, which is composed by the diffusion and radiative recombination current densities at the quasi-neutral regions (QNR). Furthermore, J_{01} can be expressed as the result of the bulk and interface recombination of minority carriers in the base ($J_{01,B}$) and emitter ($J_{01,E}$) by [100]:

$$J_{01} = J_{01,B} + J_{01,E} \tag{7.3a}$$

with each component given by:

$$J_{01,B} = \frac{qD_n n_i^2}{L_n N_A} \times \frac{\sinh\frac{d_B}{L_n} + \frac{S_n L_n}{D_n}\cosh\frac{d_B}{L_n}}{\cosh\frac{d_B}{L_n} + \frac{S_n L_n}{D_n}\sinh\frac{d_B}{L_n}}, \tag{7.3b}$$

and

$$J_{01,E} = \frac{qD_p n_i^2}{L_p N_D} \times \frac{\sinh\frac{d_E}{L_p} + \frac{S_p L_p}{D_p}\cosh\frac{d_E}{L_p}}{\cosh\frac{d_E}{L_p} + \frac{S_p L_p}{D_p}\sinh\frac{d_E}{L_p}} \tag{7.3c}$$

where d_B and d_E are the thickness of the QNR of the base and emitter with intrinsic carrier density n_i^2, and S_p and S_n are the interface recombination velocities in the hetero-interfaces emitter-window and base-BSF.

The J_{02} component involves the non-radiative recombination that takes place predominantely in the space charge region (SCR) and the perimeter of the cell, dominating the dark current at lower voltages. The contribution from the SCR can usually be modelled according to the Shockley-Read-Hall theory [101, 104], with analytical or semi-analytical formulations available under the assumption of a single mid-gap defect level [104] and for the more realistic case of multiple trap levels [95]. In the case of the solar cells in this study, however, their relatively small size results in a large contribution from perimeter recombination to the dark curves [53, 74], which cannot be theoretically determined with sufficient accuracy. Therefore, only the experimentally obtained J_{02} values are considered.

Finally, the cells illuminated performances are modeled based on the 1D analytical Hovel model [100] and its extended version for thin-film solar cells with back-side reflector [101]. This model describes carrier generation and collection in the emitter and base layers of the cells, and computes the total photo-current as the sum of the contributions from the QNR in the emitter and base and the contribution from the depletion region.

7.3 Results and Discussion

7.3.1 Solar cell performance at the beginning of life

The solar cells average illuminated $J-V$ parameters at BOL are displayed in figure 7.3, as well as the maximum and minimum obtained values. The cells presented a high reproducibility of the performance, with the thin-film devices showing a slightly larger spread of the parameters due to the increased number and less routinely applied processing steps. Overall, the short-circuit current of the thin-film solar cells is higher than the equivalent substrate-based devices due to the reflectance at the rear mirror of the long wavelength portion of the incident light that is not absorbed in the first pass through the active layers. Furthermore, the relatively large front grid coverage (16.6 %) causes the solar cells J_{sc}, and therefore also their efficiency (η), to be considerably reduced, as compared to previously reported cells [8,45]. If the J_{sc} is corrected for the active area, the devices' approximated average efficiencies range from 24.6 % (thin SB-DJ) to 27 % (TF-DJ). These efficiencies indicate high material quality, for which the BOL collection and mobility parameters are well approximated by the theoretical models [20,68].

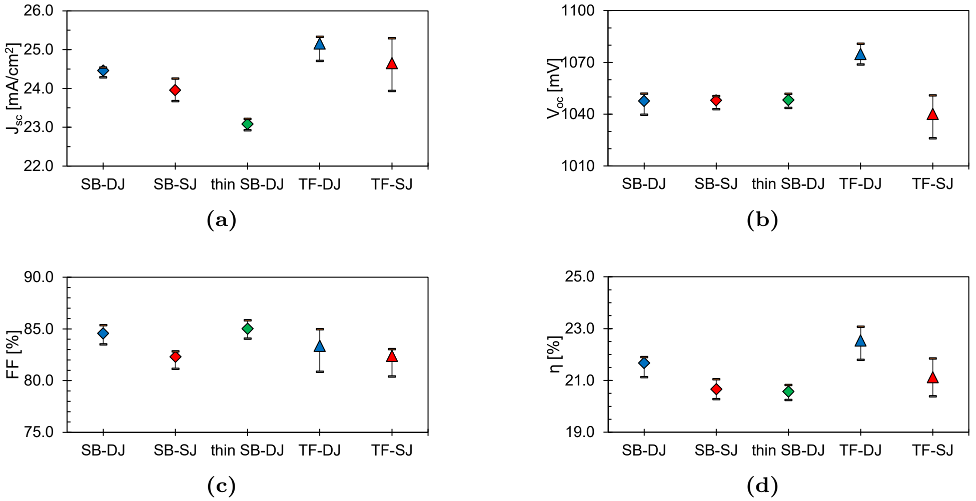

(a) (b)

(c) (d)

Figure 7.3: Average, maximum and minimum experimentally determined values of the a) J_{sc}, b) V_{oc}, c) FF and d) η of the five studied architectures at the beginning of life.

The BOL dark saturation current densities J_{01} and J_{02} are deduced from the best fit of equation 7.2 to the cells dark characteristics and $J_{sc} - V_{oc}$ data under different light intensities. The extracted values that result in the modeled curves from figure 7.5, are also displayed in table 7.1, together with all the relevant calculated BOL parameters for the five solar cell structures. The calculated J_{01} values using equations 7.3a-c, considering S_p and S_n to be negligible, show a considerable discrepancy to the experimentally deduced values. In fact, for all cells the interface recombination is limiting the dark curves at the $1kT$ region, with values ranging between 1x10^3 and 5x10^3 cm/s. With the analysis of the cells' external quantum efficiency (EQE) curves, displayed in figure 7.6, S_p and S_n are more precisely determined, and the resulting recombination velocities are depicted in table 4.1.

Table 7.1: Fitted and calculated parameters from each solar cell structure at BOL.

Parameter	SB-DJ	SB-SJ	TF-DJ	TF-SJ	thin SB-DJ
J_{01} [A/cm^2]	6.0x10^{-20}	7.0x10^{-20}	1.5x10^{-20}	5.0x10^{-20}	6.0x10^{-20}
J_{02} [A/cm^2]	6.0x10^{-12}	5.0x10^{-12}	1.0x10^{-11}	1.2x10^{-11}	6.0x10^{-12}
f_{PR}	0.78	0.78	0.95	0.95	0.67
μ_p [cm^2/Vs]	304	134	304	134	273
$\tau_{p,SRH}$ [ns]	1703	8.0	1703	8.0	1361
τ_p [ns]	133	1.8	492	4.7	46.0
L_p [μm]	10.2	0.8	19.6	1.3	5.7
μ_n [cm^2/Vs]	2709	5554	2709	5554	2709
$\tau_{n,SRH}$ [ns]	9.9	283	9.9	283	9.9
τ_n [ns]	4.2	130	7.7	227	3.2
L_n [μm]	5.4	43.2	7.4	57.1	4.7
S_p [cm/s]	2.0x10^3	1.0x10^3	0.5x10^3	1.0x10^3	4.0x10^3
S_n [cm/s]	5.0x10^3	1.0x10^3	1.0x10^3	1.0x10^3	2.0x10^3

7.3.2 Solar cell performance degradation upon proton irradiation

The averaged remaining factors of the illuminated $J - V$ parameters of the cells upon proton irradiation, normalized to the BOL values, are shown in figure 7.4, together with the modeled curves. It is clear that both thin-film and substrate based devices with a SJ geometry are less sensitive to irradiation damage than the cells with the DJ geometry, and the thinner DJ cells present a much lower degradation than their thicker counterparts, in particular for lower fluences.

The J_{sc} and V_{oc} remaining factors overlap for both thin-film and substrate based devices with similar junction depth. Because proton irradiation exposure is expected

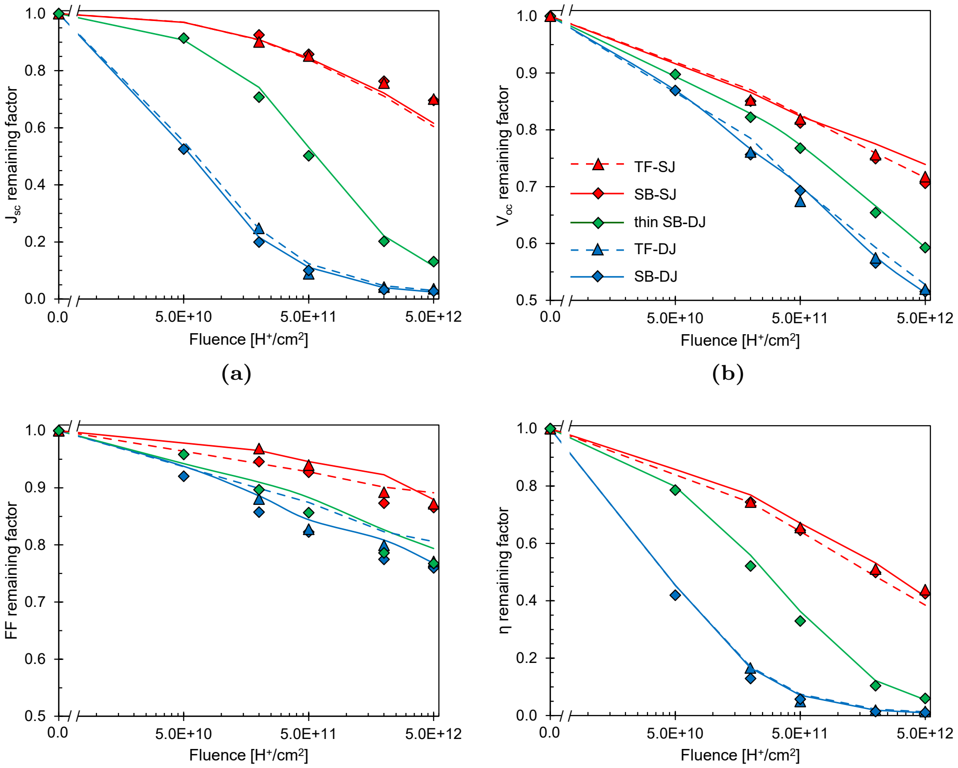

(a)

(b)

(c)

(d)

Figure 7.4: Average remaining factors of a) J_{sc}, b) V_{oc}, c) FF and d) η of the four different structures subjected to different radiation doses. The markers in these figures represent the experimental results and the lines are the modeled curves.

to create uniform damage throughout the GaAs active layers, the radiation-related degradation is expected to be material dependent, creating displacement defects and reducing the average minority carriers lifetime. All changes in performance should, therefore, be caused primarily by reduction of the minority carriers lifetime and degradation of hetero-interfaces [57], being independent of solar cell geometry and processing steps. Because of this, the changes in dark $J-V$ and EQE characteristics of the thin-film cells upon irradiation are highly similar to those shown for the substrate-based cells in figures 7.5 and 7.6.

The performance degradation mechanism is well illustrated by the EQE curves, shown in figure 7.6. The differences between the SJ and DJ geometries are related to the fact that the absorption of light into the cell decreases exponentially, so the largest fraction of light is absorbed at the upper part of the cell. In the SJ cells (figure

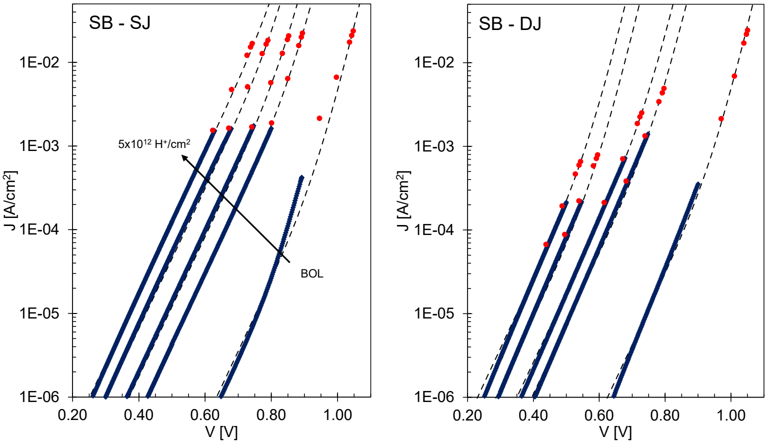

(a) **(b)**

Figure 7.5: Dark $J - V$ characteristics of a) shallow junction and b) deep junction solar cells in the substrate-based architecture after exposure to different levels of proton radiation. The red markers represent the measured $J_{sc} - V_{oc}$ values under different light intensities, the blue markers that appear as continuous lines are the measured dark curves and the dashed lines show the curves deduced from the 2-diode model (equation 7.2).

7.6a), most of the photo-generated free carriers, therefore, only have to diffuse over a short distance to the $p-n$ junction to be drifted towards the right electrode and be collected. For longer wavelengths a smaller fraction of the light is able to penetrate deeper into the cell and consequently generate some minority carriers deeper in the base, which have to travel further before reaching the $p-n$ junction. Upon irradiation, these carriers face an increased SRH recombination probability, decreasing the EQE at longer wavelengths. In DJ cells (figure 7.6b), on the other hand, most of the minority carriers generated in the thick emitter have to diffuse over a long distance before reaching the $p-n$ junction, with the exception of the small fraction generated deeper in the cell. Therefore, the collection efficiency in these cells is reduced over the entire wavelength, being slightly higher for the longer wavelength portion of the light. The degradation of the thinner SB-DJ cells (figure 7.6c) has a similar profile, but the reduced emitter thickness results in a smaller average distance between the location where light is absorbed and the SCR, and therefore the reduction of the EQE is less extreme than for the thicker devices.

In figure 7.5 the measured dark curves (dark blue lines of connected markers) and the $J_{sc} - V_{oc}$ values under different illumination intensities (red markers) are shown,

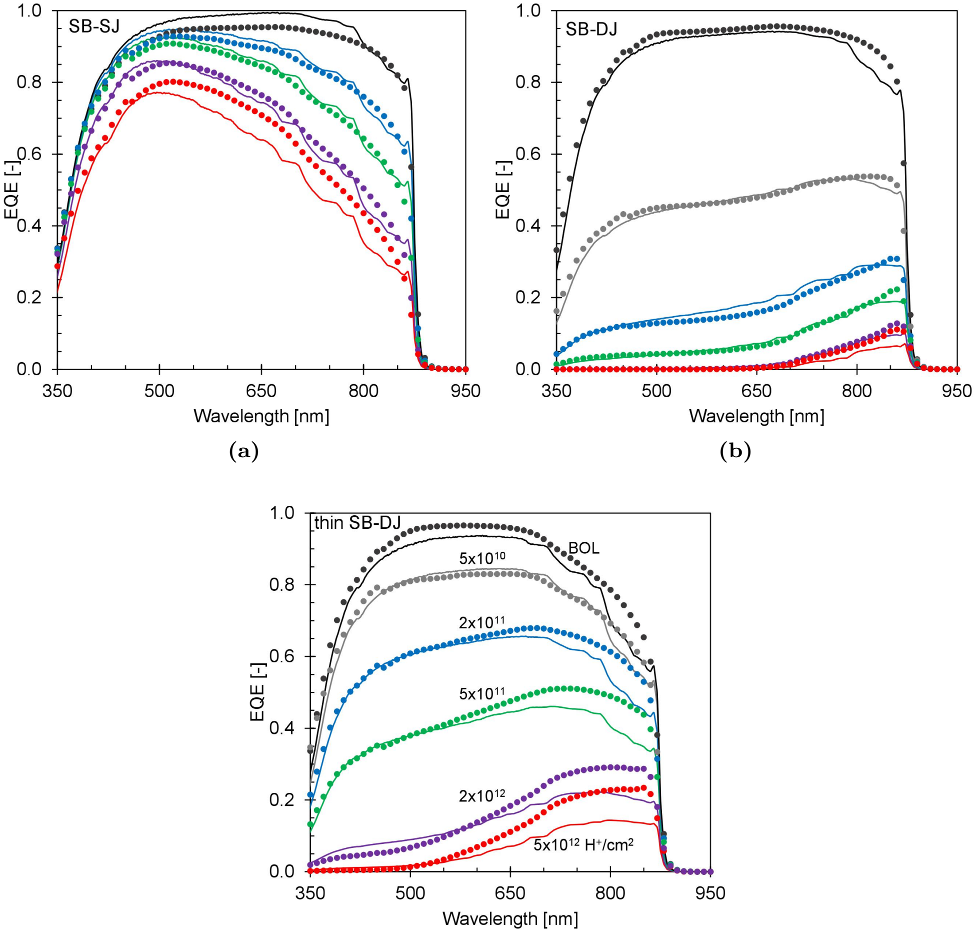

(a) **(b)**

(c)

Figure 7.6: External quantum efficiency curves of a) the shallow junction, b) the deep junction and c) the thinner deep junction solar cells in the substrate-based architecture after exposure to different doses of proton radiation. The markers represent the experimental results and the lines are the modeled curves.

as well as the best 2-diode model fits (equation 7.2) to these measured quantities. The extracted parameters J_{01} and J_{02} of the irradiated cells are displayed in figure 7.7. It is important to note that, in particular for the DJ solar cells, there may be some uncertainty with regards to the J_{01} values of the irradiated cells, since the dark curves are dominated by the $2kT$ component. The J_{01} increase for the different cell geometries is consistent with the degradation in EQE as described above, with a large difference between the saturation currents of the SJ and the DJ cells. The increase of J_{02}, on the other hand, is much more uniform between the solar cell architectures. This illustrates that, while the radiation-induced degradation of the perimeter and SCR affects the different cell geometries in a similar way, the junction depth determines how strongly the QNR and hetero-interfaces degradation will reduce the performance.

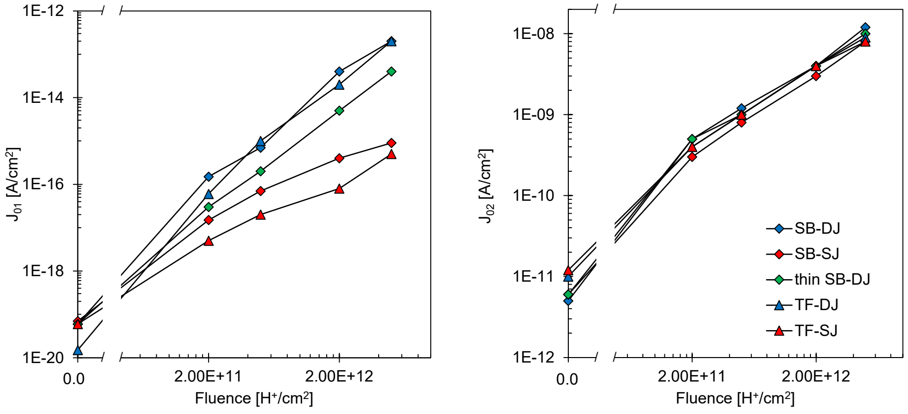

(a) **(b)**

Figure 7.7: Dark curve parameters a) J_{01} and b) J_{02} extracted from the dark curves of the solar cells subjected to different doses of proton irradiation, using the two-diode model (equation 2.9). The lines in these figures are merely a guide to the eye.

The total damage that the incidence of charged particles will generate in the semiconductor material is proportional to the incident particle non-ionizing energy loss (NIEL), or the amount of energy deposited by the particle passing through the material and resulting in displacement processes. It is possible to calculate the absorbed NIEL dose (or the DDD) of different types of irradiation by:

$$DDD = \phi \times \text{NIEL}, \tag{7.4}$$

where ϕ is the charged particle fluence. The NIEL values calculated by Baur et al. [111]

for a displacement threshold energy of 21 eV, are NIEL$_e$=1.125x10^{-5} MeVcm^2/g for 1-MeV electrons and NIEL$_p$=4.967x10^{-2} MeVcm^2/g for 1-MeV protons. Using equation 7.4, the J_{sc} of the studied solar cells is presented as a function of DDD in figure 7.8. For comparison, the data from previously reported GaAs solar cells subjected to electron irradiation [57] is also presented in this figure. Furthermore, the DDD value equivalent to the electron radiation dose of 1x10^{15} e$^-$/cm^2, usually associated to GEO missions, is highlighted in the figure as a reference.

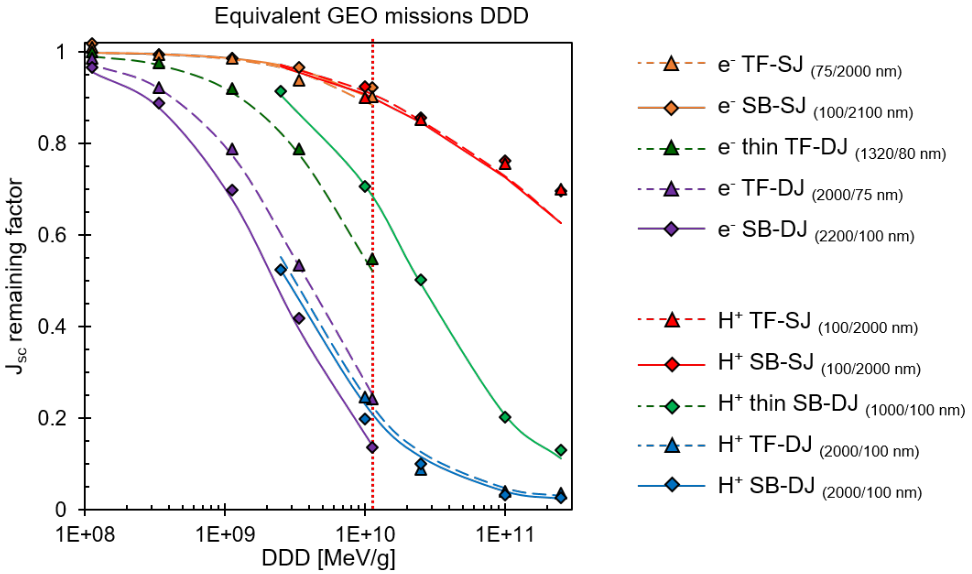

Figure 7.8: J_{sc} remaining factor of the proton irradiated solar cells in this study as well as previously reported electron irradiated cells [57] related to the total displacement damage dose (DDD). The markers represent the experimental results and the lines are the modeled curves. The red vertical line represents the equivalent DDD usually associated to GEO missions.

Although the active layer thickness of the various cell configurations evaluated in the previous study were slightly different, overall the J_{sc} remaining factors from the proton and electron irradiated cells as a function of DDD show a good correlation. For the SJ cells, the small variations in thickness between the different studied cell structures do not impact the degradation, resulting in a near perfect overlap of results in the DDD range that is covered by each of the two irradiation studies. For the DJ cells, on the other hand, the degradation is very sensitive to the small changes in active layer thickness, resulting in small discontinuities between the curves following from e$^-$ and H$^+$ irradiation. For the thinner DJ cells, the reason for the increased resilience to irradiation of the H^+ irradiated thin SB-DJ cells as compared to the e^- irradiated thin TF-DJ cells is due to the 300 nm difference in active layer thickness.

In order to simulate the cell performance upon proton irradiation, the decrease of the SRH lifetime $\tau_{p(n)_{SRH}}$ with proton fluence is modeled as:

$$\frac{1}{\tau_{p(n)_{SRH}}} = \frac{1}{\tau_{p(n)_{SRH,0}}} + K^p_{\tau_{p(n)}}\phi_p, \tag{7.5}$$

where $\tau_{p(n)_{SRH,0}}$ is the SRH lifetime at BOL and $K^p_{\tau_{p(n)}}$ is the minority carrier lifetime damage constant for proton irradiation. Based on the results from a previous study [57], an increase of the surface recombination velocity at the window and BSF hetero-interfaces is also considered. For this purpose, $S_{p(n)}$ is expressed as:

$$S_{p(n)} = S_{p(n)_0} + K^p_{S_{p(n)}}\phi_p, \tag{7.6}$$

where $S_{p(n)_0}$ is the value of $S_{p(n)}$ at BOL and $K_{S_{p(n)}}$ is the interface damage rate for proton irradiation. The lifetime degradation constants encountered in the previous study for electron irradiated GaAs cells are $K^e_{\tau_p} = 8.75\text{x}10^{-7}$ cm^2/s and $K^e_{\tau_n}$=5.25x10^{-6} cm^2/s. Because both $1/\tau_{p(n)}$ and $S_{p(n)}$ scale linearly with ϕ, which is also directly proportional to the DDD, it can be assumed that, for a certain DDD, electrons and protons cause similar degradation to the minority carrier lifetimes. Therefore, an approach was taken in which:

$$K^p_{\tau_{p(n)}} = K^e_{\tau_{p(n)}}\frac{NIEL_p}{NIEL_e}. \tag{7.7}$$

As a starting point, a similar conversion was made to $K^p_{S_{p(n)}}$. Subsequently, this latter value was corrected as needed to the fitting of the EQE and dark $J-V$ characteristics, as it also varied between the different geometries of the electron irradiated cells [57]. The resulting lifetime and interface recombination degradation constants used in the model are stated in table 7.2. Figure 7.9 depicts the reciprocal lifetime values of the SB-DJ and SB-SJ cell geometries simulated using these constants, for a large range of DDD, equivalent to proton fluences from approximately 2x10^8 to 2x10^{13} H^+/cm^2. For higher irradiation doses, the cells' minority carrier lifetime are limited by the $K_\tau\phi$ component from equation 7.5, which is also highlighted in the figures, independent of their BOL values.

Aside from J_{sc} and V_{oc} degradation, the fill factor (FF) of the solar cells also decreases upon irradiation (see figure 7.4c). The shape of the illuminated $J-V$ curves of the irradiated cells presents an effect resembling that of a reduced shunt resistance (see example in figure 7.10b), yet the dark characteristics of the cells, shown in figure 7.5, do not indicate the same effect. This difference between the illuminated

Table 7.2: Proton radiation induced damage constants, as deduced from the analysis of the $J-V$ and EQE measurements.

Solar cell	**Damage rates**			
geometry	K_{τ_p} [cm^2/s]	K_{τ_n} [cm^2/s]	K_{S_p} [cm^3/s]	K_{S_n} [cm^3/s]
SB-DJ	3.9x10^{-3}	2.3x10^{-2}	5x10^{-7}	4x10^{-5}
SB-SJ	3.9x10^{-3}	2.3x10^{-2}	5x10^{-9}	4x10^{-5}
TF-DJ	3.9x10^{-3}	2.3x10^{-2}	5x10^{-7}	4x10^{-5}
TF-SJ	3.9x10^{-3}	2.3x10^{-2}	5x10^{-9}	4x10^{-5}
thin SB-DJ	3.9x10^{-3}	2.3x10^{-2}	1x10^{-8}	4x10^{-5}

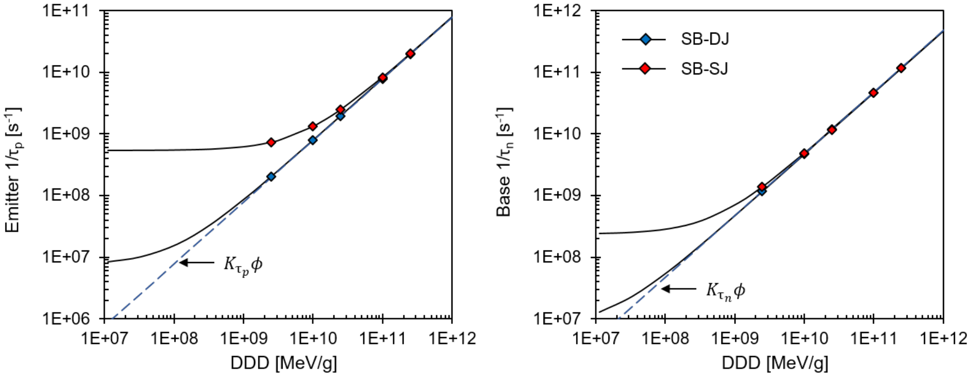

(a) (b)

Figure 7.9: Modeled a) emitter and b) base reciprocal minority carrier lifetimes of the SB-SJ and SB-DJ solar cells as a function of the displacement damage dose (DDD). The markers represent the equivalent DDD to the five studied proton irradiation doses.

and dark characteristics was also observed in a study by Salzberger et al. [94], where the voltage dependency of the space charge region width is suggested to explain the voltage-dependent photo-current. We can model the width of the emitter (w_E) and base (w_B) fractions of the space charge region by [112]:

$$w_E = \sqrt{\frac{2\varepsilon_r\varepsilon_0}{q}\frac{N_A}{N_D(N_A+N_D)}(V_{bi}-V)} \tag{7.8a}$$

and

$$w_B = \sqrt{\frac{2\varepsilon_r\varepsilon_0}{q}\frac{N_D}{N_A(N_A+N_D)}(V_{bi}-V)} \tag{7.8b}$$

where ε_0 is the vacuum permittivity, ε_r is the relative permittivity of GaAs and V_{bi} is the built in potential of the junction. The proportions to which w_E and w_B are reduced upon the application of a voltage larger than zero, for the DJ and SJ geometries, are visualized in figure 7.10a. The effect of this reduction on the shape of the curve is illustrated in figure 7.10b, where the illuminated $J-V$ curve of an irradiated SB-DJ cell is simulated considering either a constant SCR width, equal to the width at $V = 0$ (solid black line), or a V-dependent SCR width, calculated according to equations 7.8a and 7.8b (solid red line).

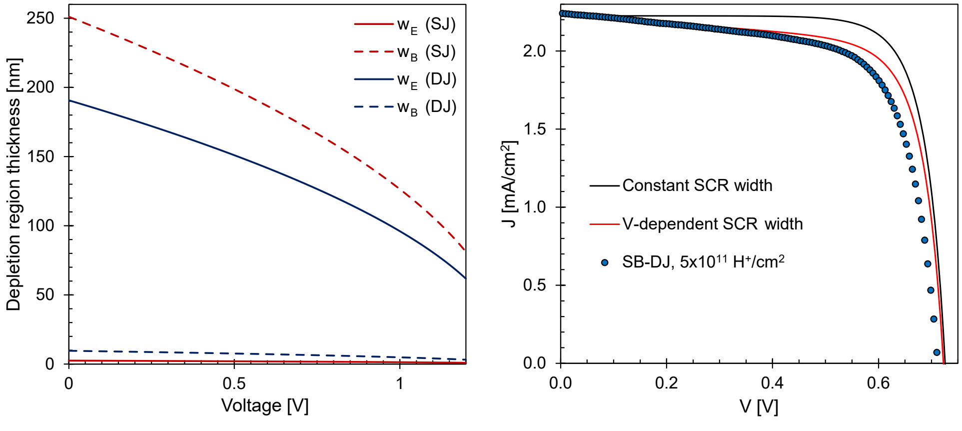

(a) (b)

Figure 7.10: a)Modeled emitter and base space charge region width as a function of the voltage for the SJ and DJ cell geometries. b) Example of an experimentally obtained illuminated $J-V$ curve (blue markers) and two model simulations, considering either a constant SCR width equal to the width for V=0 (black line) or a voltage-dependent SCR width (red line).

Because at BOL the sum $L_{p(n)} + w_{E(B)}$ is larger than the layers thicknesses, the voltage-dependency of the SCR width does not affect the illuminated curves. After irradiation, however, the diffusion length is reduced so that $L_{p(n)} + w_{E(B)}$ is much smaller than the total layer thickness, and the collection of photo-generated carriers is directly affected by the reduction of SCR. This results in a decrease in the slope of the illuminated $J - V$ curve, similar to the effect of a reduced shunt resistance, and consequently,in a reduction of the FF. As in SJ devices the reduced SCR width affects more strongly the bottom portion of the cells, which has a lower carrier generation rate, the effect of proton irradiation on the FF of cells with this geometry is smaller. By accounting for a V-dependent SCR width, the simulated curve in figure 7.10b overlaps with the experimental data (blue markers) for most of the applied voltage range. Only for voltages close to V_{oc} the current collection is over-estimated by the simulations, which indicates the presence of an increased series resistance, such as an increased lateral resistance with irradiation, not accounted for on the model.

As shown in figures 7.4, 7.6 and 7.8, the presented model simulations show a good overlap with the experimental results, which indicates the accuracy of this method. The damage constants presented in this work can be converted and applied to any particle type and energy with a known NIEL value. The performance degradation of a multitude of solar cell structures can be therefore simulated to the specific application conditions, providing a good quality of the epilayers.

7.4 Conclusions

In this study, solar cells with different architectures were subjected to 1-MeV proton irradiation with fluences up to 5x10^{12} H^{+}/cm^{2}. A significant number of solar cells were produced in order to systematically evaluate the degradation mechanisms and the effect of solar cells design in their performance under space conditions. It is shown that exposure to radiation affects the performance of solar cells by reducing the minority carrier lifetimes. Therefore, the distance from the space charge region to the location where carriers are generated is the determining aspect with regard to the cell's resilience to radiation. Since for the DJ cells upon irradiation the hole diffusion length is much smaller than the emitter thickness, the collection of generated carriers is strongly reduced, and this geometry presents a much larger decrease of J_{sc} when compared to SJ devices.

Because the fluences used in this study are representative of more extreme radiation doses than the equivalent for GEO missions, a strong degradation in performance of all solar cell geometries is observed. Furthermore, a pronounced voltage dependency of the photo-current is introduced, reducing the cells fill factor by 20%. A NIEL-based conversion of previously found minority carrier lifetime degradation constants from electron irradiation studies was demonstrated to be sufficient to obtain a good correlation between experimental and theoretical results. The degradation constants deduced from this study are material dependent, being quite insensitive to the cell's geometry and processing steps. The presence of a rear reflector in the thin-film geometry, however, allows the design of thinner devices, and has the potential to achieve higher performances at beginning-of-life.

Acknowledgements

The authors acknowledge financial support from the Brazilian National Council for Scientific and Technological Development, under the program Science Without Border, project 233259/2014-7, from the European Union's Horizon 2020 research and innovation program, under grant agreement 687253 TFQD (http://tfqd.eu), and funding under grant agreement 17043 REGENERATION from the European institute for Innovation and technology (EIT), a body supported by the European Union's Horizon 2020 research and innovation program.

Chapter 8

Temperature induced degradation of GaAs solar cells[1]

Abstract

High-efficiency, thin-film III–V solar cells offer excellent characteristics for implementation in flexible solar panels for space applications. In order to investigate the space compatibility of such cells, the temperature-induced degradation of both substrate-based cells with Au and Au/Cu contacts and thin-film cells on Au and Cu carriers was studied by accelerated ageing testing (AAT) at 200 °C. With less than 3% decrease in efficiency after 37 days at 200 °C (equivalent to 10 years at 100 °C for $E_a = 0.70$ eV), the substrate-based cells show excellent results. With a 10% decrease in efficiency after 37 days of AAT, the thin-film cells on an Au carrier exhibit promising results, given the early stage of development of the thin-film cells. On the other hand, severe degradation is ob- served for thin-film cells on a Cu carrier (decrease in efficiency > 60% after 37 days of AAT). At least two factors contribute to this severe degradation: thermally induced stress and Cu diffusion.

---

[1] The work presented in this section is based on "Temperature induced degradation of thin-film III-V solar cells for space application", by R.H van Leest, P. Mulder, N. Gruginskie, S.C.W van Laar, G. Bauhuis, H. Cheun, H. Lee, W. Yoon, R. van der Heijden, E. Bongers E. Vlieg and J.J. Schermer in IEEE Journal of Photovoltaics, vol. 7, no. 2 (2017) 702-708.

8.1 Introduction

Novel III–V solar cell preparation approaches, such as inverted metamorphic growth [113–115], wafer bonding [116], and mechanical stacking [117], require at least one growth substrate removal to create an operational device. Techniques, such as epitaxial lift off (ELO) [23, 84, 118, 119] and controlled spalling [120, 121], allow for substrate removal without destruction of the expensive growth substrate, thus, allowing for substrate reuse [29, 122]. The released active cell structures have the intrinsic potential to be turned into genuine thin-film devices if they are transferred to a thin and flexible carrier. Such thin-film III–V devices offer excellent characteristics for implementation in next-generation space solar panels, as they allow for a significant weight reduction on panel level [58], while, at the same time, offering the highest possible solar cell efficiencies [115,123,124]. Space, however, also provides a harsh environment (vacuum, harsh UV, electron and proton radiation, temperature cycling) that adds additional design challenges. Unfortunately, reports of space environmental testing of thin-film III–V solar cells are scarce [28,90,125,126] and a number of design challenges remain to be addressed. These include the need for thin-film interconnection techniques, suitable radiation, and UV resistant flexible cover glasses [11,58] and in particular a space compatible flexible carrier and support.

Both the ELO and controlled spalling techniques already implement metal-foil carriers as flexible handling and thin-film support during substrate removal [127–131]. The ELO process currently used at Radboud University, Nijmegen, The Netherlands, utilizes a Cu carrier for handling and support of the thinfilm semiconductor structures, as Cu is relatively cheap, compatible with all (post)ELO solar cell processing steps and can be easily applied by a number of chemical and physical deposition processes. However, Cu is also known to diffuse rapidly into many semiconductors [132] and to introduce midband gap trap levels [133]. The harsh environment provided by space (particularly the elevated maximum temperature during temperature cycling) may induce Cu diffusion, having a potentially detrimental effect on the device performance. The main objective of this study is to investigate the temperature-induced degradation of thin-film solar cells on Cu carrier foils.

Unfortunately, standardized test procedures to address temperature-induced degradation of (bare) thin-film III-V solar cells have yet to be developed. Since Cu diffusion is exponentially temperature dependent ($D = D_0 \exp(-E_a/k\mathrm{T})$), an accelerated life-time testing (ALT) procedure can be used to accelerate the degradation process. ALT assumes that exposure for a long period of time to a (relatively) low temperature equals a short exposure (few days) to a higher temperature. This can be described with the following equation [34]:

$$\frac{t_{op}}{t_{acc}} = \exp\left[\frac{\mathrm{E_a}}{k}\left(\frac{1}{\mathrm{T}_{op}} - \frac{1}{\mathrm{T}_{acc}}\right)\right], \tag{8.1}$$

where k is the Boltzmann constant, $\mathrm{E_a}$ is the activation energy for the degradation process, T_{op} is the regular operation temperature, T_{acc} is the accelerated test temperature and t_{op} and t_{acc} are the exposure times to the corresponding temperatures. Typically, the actual operation conditions (illumination, bias voltage, vacuum) are simulated during such tests [35, 134]. In order to exclude additional (i.e., non-temperature induced) light and/or electrically induced degradation mechanisms these operating conditions were excluded in our test procedure. In order to distinguish this procedure from regular ALT, we will refer to this adapted procedure as accelerated ageing testing (AAT).

The main difficulty with both ALT and AAT is that it requires a known activation energy. Unfortunately, experimental determination is difficult, and hence, there are very few activation energies reported for solar cell degradation [34,135,136] and none of these concern (Cu) diffusion. The European Cooperation for Space Standardization (ECSS) standard for photovoltaic assemblies and components (ECSS-EST-20-08C [35]) advises to use an $\mathrm{E_a}$ of 0.70 eV in calculations for solar cell assemblies (solar cells with cover glass, interconnect and (if used) bypass diode); this appears to be a suitable initial estimate for the activation energy. For an accelerated test temperature of 200 °C, this $\mathrm{E_a}$ of 0.70 eV results in ALT/AAT times of 8.5, 37, and 55 days for simulation of a geosynchronous orbit mission (GEO, 15 years, max 70 °C), a low-Earth orbit mission (LEO, 10 years, max 100 °C), and an extreme scenario (15 years, max 100 °C), respectively.

In previous studies [137, 138], a substrate-based model system that utilizes a 45% coverage front contact grid was used to investigate the effects of Cu diffusion on GaAs solar cells. In these studies, it was shown that at temperatures <250 °C, Cu diffusion has no significant effect on the *J*-*V* characteristics of (substrate based) solar cells. In this paper, we report the first results of AAT at 200 °C of thin-film III–V solar cells on Cu and Au carriers and compare them with the AAT results of substrate-based solar cells with and without Cu. Three different types of cells on a Cu carrier were compared: regular ELO *n*-type emitter on *p*-type base cells, ELO *p*-type emitter on *n*-type base cells, and *n*-on-*p* cells obtained by substrate etching. These three different cell types were chosen as Cu diffusion may affect *n*-type and *p*-type material differently, and Cu is at the *n*-type side in the substrate-based cells and on the *p*-type side in conventional *n*-on-*p* ELO cells. In order to exclude the potential effects of the ELO process (particularly the sample bending during lift off) on the diffusion process, substrate etched cells were prepared in such a way that they remained planar during the entire production process.

8.2 Materials and Methods

8.2.1 Solar cell processing

The substrate-based, ELO, and substrate etch solar cell structures, as schematically depicted in figures 8.1a, 8.1b and 8.1c, respectively, were grown on 2-inch substrates in an Aixtron 200 MOCVD reactor at Radboud University or obtained from a third-party supplier on 4-inch substrates. The epilayers for the cell structures were grown in upright order, and Zn was used for *p*-type doping and Si for *n*-type doping, and the *n*-GaAs contact layers were Te doped. Except for the ELO cells on an Au carrier which were grown inverted and with a Si-doped *n*-type contact layer. InGaP windows were used for the *p*-on-*n* cells and the cells on an Au carrier, whereas AlInP windows were used in the *n*-on-*p* cells on a Cu carrier and for the substrate-based cells. The thickness of the *p*-type contact layer of the *n*-on-*p* cells was varied: 300 nm for the substrate-based cells and ELO cells on an Au carrier, 50 nm for the first series of ELO cells on a Cu carrier (labeled (1)), and 100 nm for the substrate etched cells and the second series of ELO cells on a Cu carrier (labeled (2)).

First, a flexible handle was applied to the thin-film solar cell structures after which they were removed from their growth substrates either by ELO [29] or by substrate etching with a 5:1 citric acid (1 kg in 1 kg H_2O) : H_2O_2 (32%) solution. After substrate removal, the cell structures were transferred to a $\approx$ 20 μm Au mirror/back contact/carrier or to a $\approx$ 25 μm Cu carrier with a 100 nm Au mirror/back contact (the Au acts as a photon confining mirror [6,8,9,19]) and then mounted on a temporary glass carrier for further processing. Then a 45% coverage 200-nm thick Au front contact grid was applied by e-beam evaporation. For the substrate-based cells, first 45% coverage metal front contacts (100 nm Au or 100 nm Au / 3 μm Cu) and 100 nm Au back contacts were applied by e-beam evaporation. After application of the contacts 6x6 mm^2 solar cells were created by an MESA etch. A 1:2:10 NH_4OH:H_2O_2:H_2O solution was used for the GaAs layers and a 1:100:200 Br_2:HBr:H_2O solution (thin-film cells) or 37% HCl solution (substrate-based cells) was used for the AlInP and InGaP layers. For the thin-film cells, all semiconductor layers were removed, in such a way that the Au mirror / back contact became exposed after the MESA etch for the substrate-based cells only the front contact, window, emitter, and base layers were removed. Then, the front contact layer between the metal grid fingers was removed with 2:1:10 NH_4OH:H_2O_2:H_2O solution. Finally, a ZnS (42.5 nm)/MgF_2 (88.0 nm) anti-reflection coating was applied by e-beam evaporation. The resulting substrate-

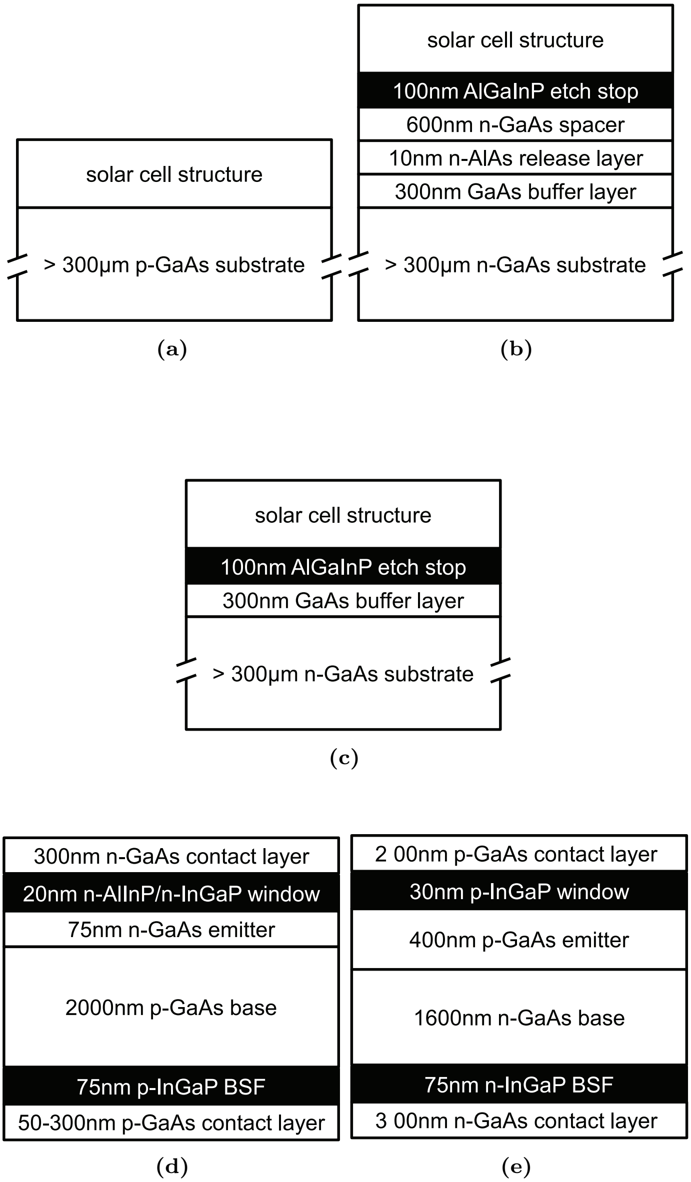

(a) **(b)** **(c)** **(d)** **(e)**

Figure 8.1: Schematic representations of a) substrate-based structure, b) ELO structure, c) substrate etch structure, d) n on p solar cell structure and e) *p*-on-*n* solar cell structure. The solar cell structures (d) and (e) were grown upright on top of the substrate-based structure (a), ELO structure (b) or substrate etch structure (c), unless specified otherwise.

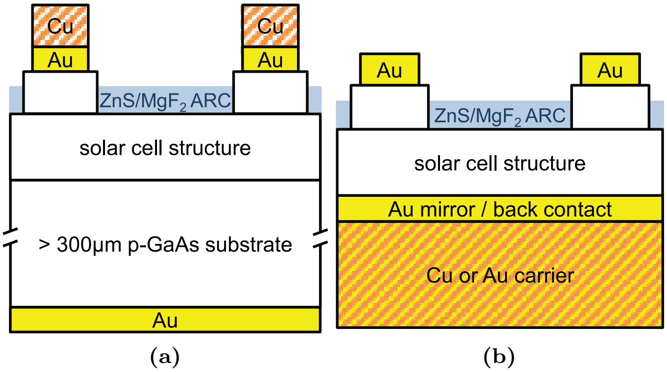

Figure 8.2: Schematic representations of a) the substrate-based structure processed into a substrate-based solar cell, and b) the ELO or substrate etch structure processed into a thin-film solar cell.

based and thin-film cells have structures as schematically depicted in figure 8.2a and 8.2b, respectively. The thin-film samples were then removed from their temporary glass carrier and cut into smaller pieces typically including three to six cells with a scalpel.

8.2.2 Characterization and accelerated life-time testing

After cell preparation, the solar cells were characterized by J-V measurements with an ABET 2000 solar simulator and ReRa Tracer 3.0 measurement software and by EQE measurements with a ReRa SpeQuest system with ReRa Photor 3.1 measurement software. Sets of 3–6 cells were then exposed to stepwise AAT in a vacuum oven at 200 °C up to a total of 37 days (equal to 10 years at 100 °C for an E_a of 0.70 eV); for some of the cells the test was extended to 55 days (equal to 15 years at 100 °C for $E_a = 0.70$ eV). After each AAT step the $J-V$ and EQE of the cells were measured and for the short-circuit current density (J_{sc}), the open-circuit voltage (V_{oc}), the fill factor (FF) and the efficiency (η) remaining factors (R) were calculated according to:

$$\text{R-parameter} = \frac{\text{parameter value after ALT}}{\text{parameter value as processed}} \; . \tag{8.2}$$

The R values were then averaged over the set of cells.

Based on the results of the AAT, a number of cells were selected for transmission electron microscopy (TEM) analysis. These solar cells were covered with a thin Pt protection layer. A cross section was made and then thinned using focused ion beam milling to allow for cross-sectional TEM analysis of the front contacts. TEM images were obtained with an FEI Titan G2 microscope.

8.3 Results and Discussion

The average beginning of life values for J_{sc}, V_{oc}, FF, and η of the different cell types are given in table 8.1. The V_{oc} values of ≈ 1.00 V and FFs of 82–83% are typical values for reasonable quality GaAs solar cells. The J_{sc} values may at first glance appear to be rather low but can be accounted for by the 45% coverage front grid, which significantly limits the amount of light entering the cells. The somewhat poorer efficiencies of the Cu ELO *p*-on-*n* and Cu substrate etch *n*-on-*p* cells can be accounted for by the fact that device design and cell processing were not yet optimized for these types of samples.

Table 8.1: Average beginning of life values of J_{sc}, V_{oc}, FF, and η of the different cell types.

	J_{sc} [mA/cm^2]	V_{oc} [mV]	FF [%]	η [%]
Au Sub *n*-on-*p*	15.6	1022.4	82.4	13.1
Cu Sub *n*-on-*p*	15.2	970.4	83.0	12.3
Au ELO *n*-on-*p*	15.6	1029.3	83.5	13.4
Cu ELO *n*-on-*p* (1)	16.4	1008.8	83.9	13.9
Cu ELO *n*-on-*p* (2)	16.2	1003.3	82.4	13.3
Cu ELO *p*-on-*n*	14.7	986.7	78.5	11.4
Cu SubEtch *n*-on-*p*	11.4	989.8	82.6	9.4

In figure 8.3, the average J_{sc}, V_{oc}, FF, and η remaining factors of substrate-based and thin-film cells with and without Cu are plotted as a function of AAT time. Both the Au and Cu substrate-based cells show little degradation, which is indicated by the R–η values that remain above 0.97 after 37 days at 200 °C. The other remaining factors indicate that this minor decrease in performance is mainly because of decreases in V_{oc} and FF. V_{oc} losses are typically caused by enhanced non-radiative recombination, whereas decreases in FF may be related to changes in J_{sc}, V_{oc}, and resistance. As these decreases occur for both Au and Cu contacts, they must be caused by general (i.e., non-Cu specific) temperature-induced degradation mechanisms. These results clearly indicate that, under these conditions, the application of a thick (3 μm) Cu layer in a III–V solar cell does not affect device performance significantly and, hence, that Cu diffusion from the contact into the active solar cell should not be an issue for application of Cu in space solar panels.

For the thin-film cells on an Au carrier the decrease in efficiency upon AAT is

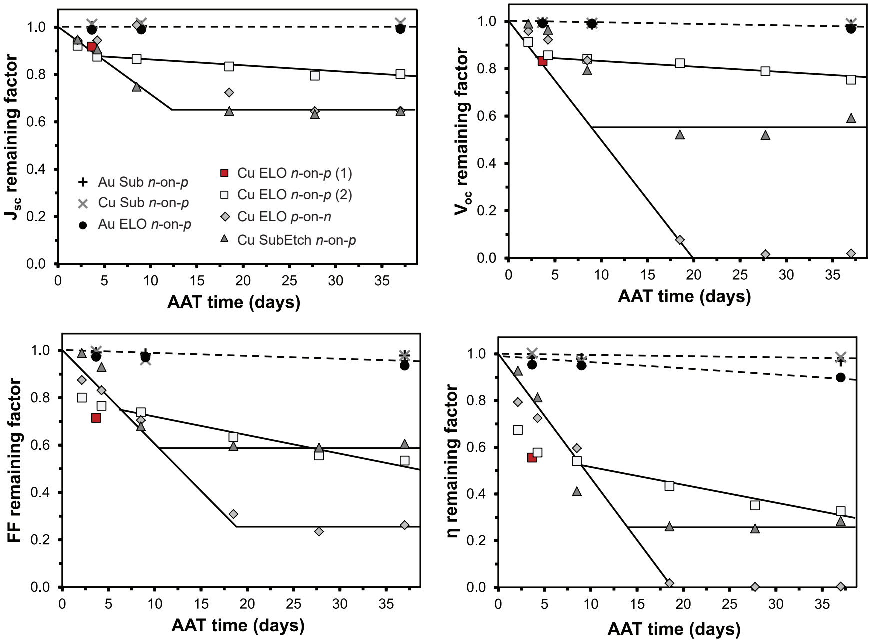

Figure 8.3: Average a) J_{sc} b) V_{oc} c) fill factor (FF) and d) efficiency (η) remaining factors as a function of the AAT time for the different solar cell structures. The dashed lines indicate the general degradation trends for substrate-based cells and thin-film cells on an Au carrier, and the solid lines indicate the trends for thin-film cells on a Cu carrier.

almost 10% after 37 days at 200 °C, mainly caused by decreases in V_{oc} and FF. This slightly larger degradation compared with substrate-based cells is likely to be (at least partially) caused by non optimized thin-film cell processing, which is in an early stage of development compared with substrate-based processing. In contrast with the cells on an Au carrier, all cells on a Cu carrier show severe and rapid degradation as is indicated by the R–η values (see figure 8.3d), which are already below 0.85 after 4.25 days. Although there are differences between the different sample types, the general degradation trends are similar for all cells on a Cu carrier. Initially, rapid decreases in all parameters can be observed, whereas the initial rapid degradation of the n on p cells starts to level off after 5–10 days, resulting in R–η values of about 0.3 after 37 days of AAT; the rapid degradation of the *p*-on-*n* cells continues (in particular for V_{oc} and FF), resulting in non-operational cells after 18 days. This hints that *n*-type GaAs is more prone to Cu diffusion, if Cu diffusion is a process contributing to device degradation. However, the fact that the substrate-based cells also have the Cu at the *n*-type side and hardly show any degradation indicates that there is at least one other

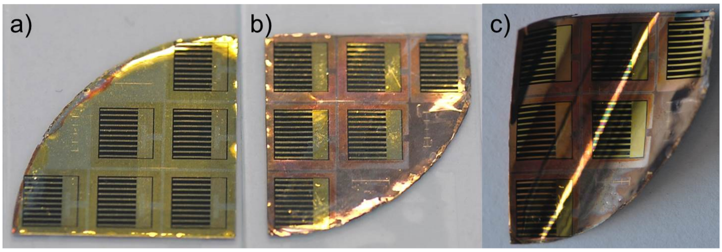

Figure 8.4: ELO *n*-on-*p* thin-film solar cells on a Cu carrier with 100 nm Au mirror a) as processed and b) and c) after 37 days AAT at 200 °C. For images a) and b) the samples were placed behind a glass plate to keep them flat. Without this glass plate the samples show significant curvature, in particular after AAT as is shown in image c).

degradation mechanism that has a major impact on the degradation process. The fact that both the substrate etched and ELO *n*-on*p* thin-film cells show a very similar degradation trend indicates that the manipulation of the thin film during the ELO process does not inflict damage that is detrimental to the solar cell device operation.

The significant decrease in J_{sc} observed for the thin-film cells on Cu carriers is in sharp contrast with the small changes (typically 1-2%) observed for cells on an Au carrier and substrate-based cells with and without Cu (both in this study and in previous work [137–139]). This indicates that the degradation process causing the decrease in J_{sc} is specific for thin-film cells on a Cu carrier and therefore of interest for further investigation. The decrease in J_{sc} is (at least partially) caused by a reflectance loss of the Au mirror that is applied to reflect transmitted and recycled photons back into the solar cell [6, 19, 26]. Figures 8.4a and 8.4b show an as processed ELO thin-film sample and an ELO thin-film sample after exposure to AAT. Around the cells the as processed sample shows the yellowish color of the gold mirror / back contact, while the sample exposed to AAT has a reddish Cu color, indicating that Cu from the carrier has diffused through the Au mirror/back contact during AAT. The same color change is observed for all samples on a Cu carrier.

TEM images show that the rear interface of thin-film cells on Au and Cu carrier are remarkably different upon exposure to AAT. After 55 days at 200 °C, the cell on an Au carrier shows a smooth Au/GaAs interface at the back (see figure 8.5a), whereas the cell on a Cu carrier shows an intermixed Au/Cu layer and a GaAs contact layer that appears to have been almost fully consumed by the Au/Cu matrix already after 3.7 days at 200 °C (see figure 8.5b). This undulation of the metal/GaAs interface and intermixing of the Au and Cu is similar to the undulation and intermixing previously observed for substrate-based cells after 1320 h (55 days) at 200 °C [138].

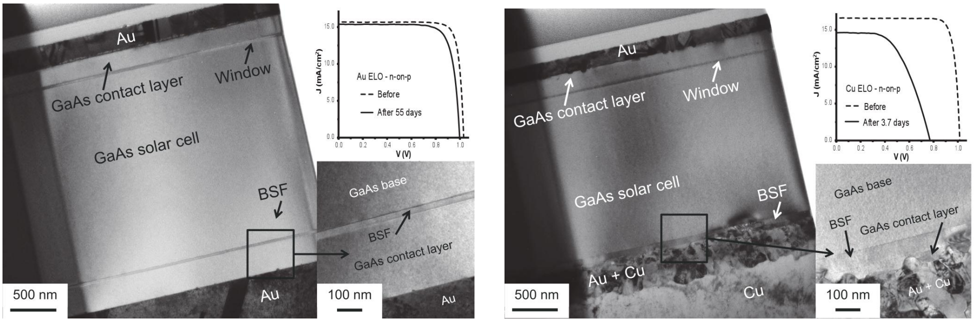

(a) **(b)**

Figure 8.5: TEM images of (a) a thin-film ELO cell on an Au carrier after 55 days at 200 °C and (b) and (b) a thin-film ELO cell on a Cu carrier after 3.7 days at 200 °C.

The intermixing of the Au and Cu is in agreement with the observed color change of the carrier foil (see figure 8.4). The intermixing and particularly the undulation of the Au/GaAs interface indicates severe degradation of the Au mirror.

The reflectivity loss of the mirror can also be deduced from the EQE data of the cells. In figure 8.6a the EQE of an *n*-on-*p* thin-film ELO cell on an Au carrier is plotted before AAT and after 9 days at 200 °C and in figure 8.6b the EQE of an *n*-on-*p* ELO thin-film cell on a Cu carrier is plotted before AAT, after 8.5 days and after 37 days at 200 °C. After AAT the interference fringes in the 700-900 nm range caused by the reflection of the mirror [8] have disappeared for the cell on a Cu carrier, but remain visible for the cell on an Au carrier. Additionally the EQE data show that the loss in J_{sc} for the cells on a Cu carrier is mainly caused by a reduced collection efficiency of carriers created by long wavelength (600-900 nm) photons, which are mostly absorbed at the back of the cell. The fact that no reduction in collection efficiency is observed for the cell on an Au carrier suggests that the decrease for the cells on a Cu carrier is Cu related. Two mechanisms may contribute to the loss in collection efficiency: reduced reflection of photons by the mirror and diffusion of Cu into the active cell, creating trap levels that reduce the carrier collection efficiency.

Next we discuss V_{oc}. The decrease in V_{oc} of the thin-film cells on Cu carrier is far more severe than the decreases observed for substrate-based cells and thin-film cells on an Au carrier. As decreases in V_{oc} are typically related to increases in the (non-radiative) recombination current and Cu is known to introduce trap levels in the band gap [133] which act as recombination centres, the decreases in V_{oc} are most likely related to the introduction of Cu trap levels as a result of Cu diffusion. The colour change of the metal foil as depicted in figure 8.4b and the reduced collection

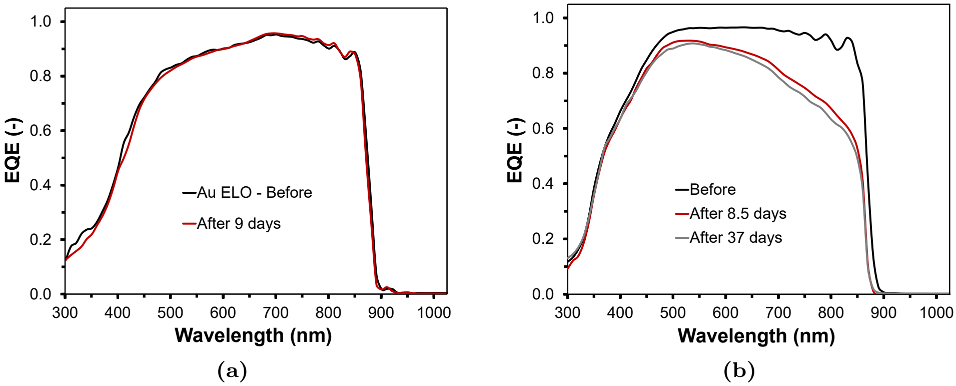

Figure 8.6: EQE of (a) a thin-film ELO *n*-on-*p* solar cell on an Au carrier before AAT (black curve) and after 9 (red curve) days of AAT at 200 ∘C and (b)a thin-film ELO *n*-on-*p* solar cell on a Cu carrier with 100-nm Au mirror before AAT (black curve) and after 8.5 (red curve) and 37 (gray curve) days of AAT at 200 °C.

efficiency in de long wavelength range of the EQE (figure 8.6) all indicate that Cu diffusion may indeed take place. Direct quantitative measurement of Cu diffusion by, for example, SIMS is difficult as the concentration of Cu causing an electrical effect is most likely significantly below the detection limit of such methods. A problem that was already discussed by Istratov et al. [140] for Cu diffusion in silicon. However, as the substrate-based Cu cells do not show signs of Cu diffusion there must be a thin-film related process that induces/enhances the diffusion process.

The image in figure 8.4c provides a possible explanation for the enhanced Cu diffusion in thin-film cells, as it shows that the carrier tends to curl upon exposure to AAT. This curling of the sample can be explained by the difference in thermal expansion coefficient between the Cu (16.5x10^{-6} K^{-1}) and Au (14.2x10^{-6} K^{-1}) on the one hand and GaAs (5.4x10^{-6} K^{-1}) on the other. Upon exposure to AAT the metal expands more rapidly, thereby creating stress in the solar cell material. Such stress is likely to induce (micro-)cracks and other defects which are known to enhance diffusion [141, 142].

8.4 Conclusions & Outlook

In order to investigate the space compatibility of thin-film III–V solar cells, the temperature-induced degradation of thin-film cells on Cu and Au carriers and substrate based cells with Au and Au/Cu front contacts was studied by AAT. The substrate-based cells show little degradation with a decrease in efficiency of 3% or less for both Au and Au/Cu contacts (after 37 days, equivalent to 10 years at 100 °C for an E_a of 0.70 eV), which indicates that application of Cu in itself is not a threat to the long term device performance. The slight efficiency loss of $\approx$ 10% of the cells on an Au carrier after 37 days at 200 °C, indicates that there is a definite potential for the thin-film III–V cells in space modules. The severe degradation observed for the cells on Cu carriers (efficiency losses typically >60% after 37 days at 200 °C) shows that the carrier material significantly influences the device stability. The fact that both ELO and substrate etched thin-film cells on a Cu carrier show severe degradation indicates that the ELO process itself does not affect the device performance. At least two factors contribute to the decrease in solar cell performance: thermally induced stress and Cu diffusion. These two factors may influence each other as diffusion processes are likely to be enhanced by damage (such as cracks and defects) induced by thermal stress.

In order to improve long-term stability of thin-film solar cells, a better understanding of the effect(s) of thermally induced stress on the solar cell/carrier combination is required. As the actual maximum temperature reached during solar cell operation in space is significantly lower (typically max ± 100 °C, possibly somewhat higher in extreme circumstances) than the AAT temperature applied in this study (200 °C), the critical levels of stress induced by the AAT may not be reached during an actual space mission. Lowering the AAT temperature to a value well below 200 °C may significantly reduce the thermally induced stress. Additionally, mounting the thin-film cells on a space compatible flexible mechanical support might help reducing the stress effects in the thin-film cells (i.e., preventing the thin-film cells from bending upon exposure to thermal stress). Furthermore, a solution for the intermixing of the Au mirror and Cu carrier and diffusion of Cu into the device has to be found. This could be achieved either by implementation of a barrier that prevents intermixing of the Au mirror/back contact and the Cu carrier or by replacement of the Cu carrier with a different (metal) carrier.

Acknowledgements

The authors would like to thank Wil Corbeek for the technical support. This work was supported in part by the Netherlands Space Office under Project PEP12010, in part by the European Union's Horizon 2020 research and innovation programme under Grant 687253, and in part by the Brazilian National Council for Scientific and Technological Development under Grant 233259/2014-7

Chapter 9

Summary and Outlook

Thin-film GaAs solar cells have several application advantages over cells on their native GaAs or Ge substrate, such as a high power to weight ratio, flexibility, prospects for costs reduction by wafer reuse and possibilities for transferred device applications. These advantages allow the solar cell systems to be optimized to the specific application requirements. Furthermore, it has been shown that the thin-film cells present a superior performance than of their substrate-based counterparts, which is attributed to an increased photon recycling provided by the reflectance of photons at the rear mirror. Because GaAs solar cells quality increased to a point where their performance is limited by radiative recombination, the high internal emissions in these cells make the optical design of the devices to be extremely important. In this thesis, the design and fabrication of thin-film GaAs solar cells is studied, focusing on photon recycling mechanisms and their applicability in space missions.

An experimental proof of concept of the importance of the rear mirror reflectance to the solar cells performance is presented in chapter 4, where the fabrication process of thin-film GaAs solar cells with a patterned semi-planar mirror is elaborated. A high absorption of photons at the bottom contact layer, that typically remains whole in the thin-film configuration, is initially identified, and a fabrication technique to partially remove it is developed. In this manner, an approximated increase of almost to 30% in the back reflectance is obtained. It is shown that cells with a shallow junction design do not benefit from an increased photon recycling. The analysis of the cells dark characteristics indicate that these cells are operating in the non-radiative recombination regime, and therefore the contribution of photon recycling to the performance is small. For the deep junction solar cells, on the other hand, the patterning resulted in a more than linear increase in the open circuit voltage and a linear increase in the short circuit current, which is in good agreement with previously reported theoretical models. However, as the rear contact coverage is reduced to 10%, the cells fill factor decrease drastically, as a result of an increased lateral resistance.

In chapter 5, an in-depth analysis of the photon recycling mechanisms in thin-film GaAs solar cells is shown. Using theoretical modeling supported by experimentally obtained results, the reflectance at the rear layer structures of the cells, the photon recycling probability and the solar cell performance are correlated. Furthermore, the technique of patterning the rear mirror is further improved, and the previously seen decrease in fill factor is reduced, which allowed the production of solar cells with back contact coverages as low as 1.5%. In this chapter, it is shown that the photon recycling probability can be strongly reduced by the front grid coverage, which is usually disregarded in rear mirror focused studies. Furthermore, the perimeter and interface recombination are identified as limiting parameters to the cells dark characteristics, obstructing the cells internal radiative efficiency and preventing further increase of the open circuit voltage. In order to achieve a significant benefit of increased photon recycling probability to the solar cell performance, these limiting mechanisms need to be properly addressed.

The importance of the cells design for their resilience to the space applications is studied in chapters 6, 7 and 8 of this thesis, by analyzing the cells performances under extreme conditions that mimic the space environment. In chapter 6, the effects of electron irradiation on the performance of GaAs solar cells with different architectures is studied. The combined experimental and theoretical analysis of the degradation of the cell performance due to irradiation allowed the determination of a coherent set of damage constants. This study demonstrates that, because the incidence of electrons reduces the minority carriers lifetime, the solar cell performance degradation primarily depends on the average distance between the location where light is absorbed and the depletion region. Therefore, although the deep junction design can achieve higher efficiencies at the beginning of life, it shows a much stronger performance degradation upon electron irradiation than the shallow junction cells. Besides the reduction of carriers lifetime, the modeling study has pointed out that the electron irradiation strongly affects the quality of hetero-interfaces, characterized by an increase in the interface recombination velocities.

The effects of proton irradiation on the performance of GaAs solar cells with different designs are studied in chapter 7. Similarly to electron irradiation, the incidence of protons reduces the minority carrier lifetimes, and therefore, the distance from the space charge region to the location where carriers are generated is also the determining aspect with regard to the resilience of cells to proton irradiation. A particle non-ionizing energy loss (NIEL) based conversion of the previously found degradation constants from electron irradiation studies was demonstrated to provide a good correlation between experimental and theoretical results. Because the used proton fluences are representative of more extreme radiation doses than the equivalent for geostationary Earth orbit (GEO) missions, a strong degradation in performance of all solar cell geometries is encountered. Furthermore, a pronounced voltage dependency of the photo-current is observed, reducing the cells fill factor in up to 20%, a mechanism that did not occur in the electron irradiated cells.

Temperature related degradation processes, such as metal diffusion into the semiconductor, are studied in chapter 8. By studying both substrate-based and thin-film cells, with either Au or Cu thick contacts, the different degradation mechanisms could be identified. Since the substrate-based Cu cells show less than 3% decrease in efficiency for exposure times equivalent to GEO missions, Cu diffusion alone does not seem to be a threat to solar cell operation. Both Au and Cu thin-film cells, on the other hand, show degradation in the performance, indicating that thermally induced stress aggravates Cu diffusion, resulting in a strong decrease in the cells performance. Provided that thermally induced stress in the thin-film cells can be prevented or attenuated, copper applied as a foreign carrier might still be a viable option for space application.

The studies described in this thesis provide a better understanding of the working mechanisms and limitations of thin-film GaAs solar cells, and allow the performance prediction for cells of different designs at their operating conditions. The optimization of the growth of hetero-interfaces with low surface recombination velocities will result in cells with higher performances at the beginning of life due to an increased open circuit voltage, as well as a reduced effect to the degradation of the cells parameters upon irradiation. Furthermore, the fabrication of cells with larger areas should mitigate the perimeter recombination effects so that it is not limiting the cells dark characteristics. The knowledge acquired from these studies can be applied to the development of light weight novelty space power arrays, but also on Earth applications that require high a power density, such as solar-powered autonomous cars or unmanned aerial vehicles. In these cases, the radiation-related degradation, and in some cases also the temperature induced degradation, is not relevant to the cells performance. Therefore the applicability of optimized deep junction GaAs solar cells with a highly reflective back mirror is ideal, either as a single junction or as a bottom sub-cell in tandem devices.

Samenvatting en Vooruitzicht

GaAs dunne-film zonnecellen hebben verschillende voordelen ten opzichte van cellen die het GaAs of Ge substraat behouden, zoals een hoge vermogen-gewichtsverhouding, flexibiliteit, kostenbesparingperspectieven door waferhergebruik en de mogelijkheid tot overdracht naar verschillende oppervlakken. Dankzij deze voordelen kunnen de zonnecelsystemen worden geoptimaliseerd voor specifieke toepassingsvereisten. Bovendien is aangetoond dat dunne-filmcellen vergelijkbare cellen op substraat overtreffen, door de verhoogde fotonrecycling die mogelijk wordt door reflectie van fotonen die de spiegel aan de achterkant bereiken. Doordat de kwaliteit van GaAs zonnecellen is toegenomen tot een niveau waar de prestaties beperkt worden door stralende recombinatie, wordt het optische ontwerp van de cellen uitermate belangrijk vanwege de hoge interne emissies. In dit proefschrift wordt het ontwerp en de fabricage van GaAs dunne-film zonnecellen bestudeerd, waarbij de focus ligt op fotonrecyclingmechanismen en toepasbaarheid in de ruimtevaart.

Een experimenteel proof of concept van het belang van reflectie aan de spiegelende achterkant voor de prestaties van zonnecellen wordt gepresenteerd in hoofdstuk 4, waar de methode voor het maken van dunne-film GaAs zonnecellen wordt uitgewerkt die een patroon bevatten en een semi-vlakke spiegel. Hoge fotonabsorptie in de onderste contactlaag, die normaliter intact blijft in de dunne-filmconfiguratie, wordt aanvankelijk geïdentificeerd en een methode ontwikkeld om deze gedeeltelijk te verwijderen. Op deze manier neemt de reflectie aan de achterkant toe met ongeveer 30%. Het wordt aangetoond dat cellen met een ondiepe junctie niet profiteren van verhoogde fotonrecycling. Analyse van de donkerkarakteristieken geeft aan dat cellen met deze geometrie werken in het niet-stralende recombinatieregime en daarom is de bijdrage van fotonrecycling aan de prestaties klein. Aan de andere kant resulteerde het patroon bij diepe-junctie zonnecellen in een meer dan lineaire toename van de openklemspanning en een lineaire toename van de kortsluitstroom, wat overeenkomt met eerder gerapporteerde theoretische modellen. Echter wordt het contactoppervlak gereduceerd tot 10%, waardoor de vormfactor drastisch afneemt als gevolg van een verhoogde laterale weerstand.

In hoofdstuk 5 wordt een diepgaande analyse gepresenteerd van de mechanismen voor fotonrecycling in GaAs dunne-film zonnecellen. Reflectie in de structuur van de onderste cellagen, de waarschijnlijkheid van fotonrecycling en zonnecelprestaties worden gecorreleerd door theoretische modellen ondersteund door experimenteel verkregen resultaten. Bovendien is de methode voor het aanbrengen van het patroon voor de spiegel verbeterd en is de eerder waargenomen afname van de vormfactor gereduceerd, waardoor de productie van zonnecellen met een lager contactoppervlak tot 1.5% mogelijk is geworden. In dit hoofdstuk is aangetoond dat de fotonrecyclingkans sterk kan worden verkleind door de dekking van het voorcontact, wat in het algemeen buiten beschouwing wordt gelaten in studies gericht op de spiegel aan de achterkant. Bovendien worden interface- en perimeterrecombinatie geïdentificeerd als beperkende parameters voor de donkerkarakteristieken van cellen, waardoor de interne stralingsefficiëntie wordt belemmerd en verdere toename van de openklemspanning wordt voorkomen. Om een significant voordeel van de verhoogde fotonrecyclingkans op de prestaties van zonnecellen te bereiken, moeten deze beperkende mechanismen adequaat worden aangepakt.

Het belang van het celontwerp bij toepassingen in de ruimtevaart wordt bestudeerd in hoofdstukken 6, 7 en 8 van dit proefschrift door celprestaties te analyseren onder extreme omstandigheden die de ruimteomgeving simuleren. In hoofdstuk 6 worden de effecten van elektronenbestraling op de prestaties van GaAs zonnecellen met verschillende structuren bestudeerd. De combinatie van experimentele en theoretische analyse van degradatie van de celprestaties als gevolg van bestraling maakte de bepaling van een coherente set schadeconstanten mogelijk. Deze studie toont aan dat, aangezien de inval van elektronen de levensduur van minderheidsladingdragers verkort, de verslechtering van de prestaties van zonnecellen voornamelijk afhangt van de gemiddelde afstand tussen waar het licht wordt geabsorbeerd en het depletiegebied. Hoewel diepejunctiecellen vroeg in de levensduur een hogere efficiëntie kunnen bereiken, vertonen ze een grotere prestatievermindering door elektronenbestraling in vergelijking met cellen met een ondiepe junctie. Naast het verkorten van de levensduur van ladingsdragers, volgt uit de studie dat elektronenbestraling de kwaliteit van hetero-interfaces sterk beïnvloedt, gekenmerkt door een toename in interface-recombinatiesnelheden.

De effecten van protonbestraling op de prestaties van GaAs zonnecellen met verschillende structuren worden besproken in hoofdstuk 7. Net als elektronenbestraling vermindert de inval van protonen de levensduur van minderheidsladingdragers en daardoor is de afstand van het depletiegebied tot de plaats waar de ladingdragers gegenereerd worden ook het bepalende aspect met betrekking tot de tolerantie van zonnecellen tegen protonbestraling. Er is aangetoond dat een op deeltjes gebaseerde *non-ionizing energy loss* (NIEL) conversie van de eerder gevonden degradatieconstanten een goede correlatie geeft tussen experimentele en theoretische resultaten. Omdat de gebruikte protonflux representatief is voor stralingsdoses extremer dan het equivalent voor geostationaire missies wordt een sterke verslechtering van de prestaties van alle zonnecelgeometrieën gevonden. Bovendien vertoont de lichtgegenereerde stroom een sterke spanningsafhankelijkheid waardoor de vormfactor met maximaal 20% wordt verminderd, een mechanisme dat niet plaatsvond in met elektronen bestraalde cellen.

Temperatuurgerelateerde degradatieprocessen, zoals diffusie van metaal in de halfgeleider, worden bestudeerd in hoofdstuk 8. Door dunne-film en substraatcellen met Au of Cu contacten te bestuderen, kunnen de verschillende degradatiemechanismen worden geïdentificeerd. Omdat substraatcellen met Cu contacten een efficiëntiereductie van minder dan 3% vertonen voor blootstellingstijden gelijk aan geostationaire missies, lijkt Cu diffusie op zichzelf de werking van zonnecellen niet te bedreigen. Zowel Au als Cu dunne-filmcellen vertonen daarentegen prestatievermindering, wat aangeeft dat thermisch geïnduceerde stress Cu diffusie verergert, wat resulteert in een scherpe afname in de prestaties. Aangezien thermisch geïnduceerde stress in dunnefilmcellen kan worden vermeden of verminderd, kan koper als drager nog steeds een haalbare optie zijn voor toepassingen in de ruimtevaart.

De studies beschreven in dit proefschrift geven een beter inzicht in de mechanismen en beperkingen van GaAs dunne-film zonnecellen, waarmee de prestaties van cellen met verschillende structuren voorspeld kunnen worden bij de door de toepassing vereiste omstandigheden. Het optimaliseren van de groei van hetero-interfaces met lage oppervlakterecombinatiesnelheden zal resulteren in cellen die vroeg in de levensduur beter presteren als gevolg van een hogere openklemspanning, evenals verminderde degradatie van celparameters ondergaan na bestraling. Bovendien zou de productie van cellen met grotere oppervlakken de effecten van perimeterrecombinatie moeten verminderen, om de donkerkarakteristieken van de cellen niet te beperken. De inzichten verkregen uit deze studies kunnen worden toegepast bij de ontwikkeling van lichtgewicht en innovatieve zonneceltechnieken voor in de ruimtevaart, maar ook bij toepassingen op aarde die een hoge energiedichtheid vragen, zoals autonome auto's op zonne-energie of onbemande luchtvaartuigen. In deze gevallen is stralingsgerelateerde degradatie, en in sommige gevallen ook temperatuurgeïnduceerde degradatie, niet relevant voor de prestaties van de cel. Daarom is de toepasbaarheid van geoptimaliseerde diepe-junctie GaAs zonnecellen met een sterk reflecterende spiegel aan de achterkant ideaal, zowel voor cellen met een enkele junctie en als de onderste subcel in een tandemconfiguratie.

Resumo e Perspectivas

As células solares de filmes finos de GaAs possuem diversas vantagens quando comparadas às células fabricadas em seus substratos nativos de GaAs ou Ge, como por exemplo uma alta relação potência-peso, flexibilidade, prospectos para redução de custo com o reuso do wafer e a possibilidade de transferência para diferentes superfícies. Estas vantagens permitem que o sistema de células solares seja otimizado para os requisitos específicos da aplicação. Além disso, foi demonstrado que as células de filme fino apresentam um desempenho superior ao de células semelhantes baseadas em substrato, o que é atribuído a uma maior reciclagem de fótons proporcionada por sua reflexão no espelho inferior. O alto desenvolvimento da qualidade das células solares de GaAs faz com que seu desempenho seja limitado pela recombinação radiativa, as altas emissões internas nessas células tornam o design óptico dos dispositivos extremamente importante. Nesta tese, é apresentado o estudo do projeto e da fabricação de células solares de filmes finos de GaAs, com foco nos mecanismos de reciclagem de fótons e sua aplicabilidade em missões espaciais.

Uma prova de conceito experimental da importância da refletância do espelho inferior para o desempenho das células solares é apresentada no capítulo 4, onde o processo de fabricação de células solares de filmes finos de GaAs com um espelho semi-plano padronizado é elaborado. A alta absorção de fótons na camada de contato inferior, que normalmente permanece inteira na configuração de filme fino, é inicialmente identificada e uma técnica de fabricação para removê-la parcialmente é desenvolvida. Deste modo, é obtido um aumento aproximado de 30% na refletância inferior. É mostrado que células com um design de junção rasa não se beneficiam do aumento na reciclagem de fótons. A análise das características de escuro indica que células com esta geometria operam no regime de recombinação não-radiativa e, portanto, a contribuição da reciclagem de fótons para o desempenho é pequena. Por outro lado, para as células solares de junção profunda, o padrão resultou em um aumento mais do que linear na tensão do circuito aberto e um aumento linear na corrente de curto-circuito, o que está de acordo com os modelos teóricos relatados anteriormente.

No entanto, como a cobertura do contato inferior é reduzida para 10%, o fator de forma das células diminui drasticamente, resultado de uma maior resistência lateral.

No capítulo 5, é apresentada uma análise aprofundada dos mecanismos de reciclagem de fótons nas células solares de filmes finos de GaAs. A refletância nas estruturas da camada inferior das células, a probabilidade de reciclagem de fótons e o desempenho da célula solar são correlacionadas pela modelagem teórica suportada por resultados obtidos experimentalmente. Além disso, a técnica de padronização do espelho inferior é aprimorada e a redução no fator de forma, observada anteriormente, é reduzida, o que permitiu a produção de células solares com coberturas do contato inferior tão baixas quanto 1,5%. Neste capítulo, é mostrado que a probabilidade de reciclagem de fótons pode ser fortemente reduzida pela cobertura do contato frontal, que geralmente é desconsiderada em estudos focados no espelho inferior. Além disso, a recombinação de interface e de perímetro são identificados como parâmetros limitantes às características de escuro das células, obstruindo a eficiência radiativa interna das células e impedindo um aumento maior da tensão de circuito aberto. Para alcançar um benefício significativo da probabilidade aumentada de reciclagem de fótons no desempenho das células solares, esses mecanismos limitadores precisam ser adequadamente abordados.

A importância do design das células para sua resiliência às aplicações espaciais é estudada nos capítulos 6, 7 e 8 desta tese, por meio da análise do desempenho das células sob condições extremas que simulam o ambiente espacial. No capítulo 6, são estudados os efeitos da irradiação de elétrons no desempenho de células solares de GaAs com diferentes arquiteturas. A combinação de análises experimental e teórica da degradação do desempenho das células devido à irradiação permitiu a determinação de um conjunto coerente de constantes de dano. Este estudo demonstra que, como a incidência de elétrons reduz o tempo de vida dos portadores de carga minoritários, a degradação do desempenho das células solares depende principalmente da distância média entre o local em que a luz é absorvida e a região de depleção. Portanto, embora os dispositivos de junção profunda possam alcançar eficiências mais altas no início da vida útil, eles apresentam uma maior degradação de desempenho com irradiação de elétrons em comparação com as células de junção rasas. Além da redução do tempo de vida dos portadores de carga, o modelo sugere que a irradiação de elétrons afeta fortemente a qualidade das interfaces, caracterizadas por um aumento nas velocidades de recombinação de interface.

Os efeitos da irradiação de prótons no desempenho de células solares de GaAs com diferentes configurações são estudados no capítulo 7. Da mesma forma que a irradiação de elétrons, a incidência de prótons reduz o tempo de vida dos portadores de carga minoritários e, portanto, a distância da região de carga espacial até o local onde portadores são gerados também é o aspecto determinante no que diz respeito à resiliência das células à irradiação de prótons. Uma conversão das constantes de dano anteriormente encontradas nos estudos de irradiação de elétrons, baseada na perda de energia não-ionizante (NIEL) das partículas, demonstrou fornecer uma boa correlação entre resultados experimentais e teóricos. Como as fluências de prótons usadas são representativas de doses de radiação mais extremas que o equivalente para missões de órbita terrestre geoestacionária (GEO), uma forte degradação no desempenho de todas as geometrias de células solares é encontrada. Além disso, a foto-corrente demonstra uma forte dependência da tensão, reduzindo o fator de forma das células em até 20%, um mecanismo que não ocorreu nas células irradiadas por elétrons.

Os processos de degradação relacionados à temperatura, como a difusão de metais no semicondutor, são estudados no capítulo 8. Ao estudar células de filme fino e baseadas em substrato com contatos espessos de Au ou Cu, os diferentes mecanismos de degradação podem ser identificados. Como as células de Cu baseadas em substrato mostram uma redução de eficiência de menos de 3% para tempos de exposição equivalentes às missões GEO, a difusão de Cu por si só não parece ameaçar a operação das células solares. Ambas as células de filme fino de Au e de Cu, por outro lado, mostram degradação no desempenho, indicando que o estresse induzido termicamente agrava a difusão do Cu, resultando em uma forte diminuição no seu desempenho. Desde que o estresse induzido termicamente nas células de filmes finos possa ser evitado ou atenuado, o cobre aplicado como suporte ainda pode ser uma opção viável para a aplicação espacial.

Os estudos descritos nesta tese fornecem uma melhor compreensão dos mecanismos de operação e limitações das células solares de filmes finos de GaAs, e permitem a previsão do desempenho de células de diferentes arquiteturas em suas condições de operação. A otimização da fabricação de interfaces com baixas velocidades de recombinação da superfície resultará em células com desempenho superior no início da vida útil, devido a um aumento da tensão do circuito aberto, bem como uma redução da degradação dos parâmetros das células após irradiação. Além disso, a fabricação de células com áreas maiores deve mitigar os efeitos de recombinação de perímetro, de modo a não limitar as características de escuro das células. O conhecimento adquirido com esses estudos pode ser aplicado ao desenvolvimento de sistemas solares espaciais leves e inovadores, mas também em aplicações na Terra que exigem alta densidade de energia, como carros autônomos movidos a energia solar ou veículos aéreos não tripulados. Nesses casos, a degradação relacionada à radiação e, em alguns casos, também a degradação induzida pela temperatura, não é relevante para o desempenho das células. Portanto, a aplicabilidade de células solares GaAs de junção profunda otimizadas, com um espelho inferior altamente reflexivo é ideal, tanto para uma junção única quanto como para uma sub-célula inferior em dispositivos em tandem.

Bibliography

[1] T. Stocker, Q. D., G. Plattner, M. Tignor, S. Allen, J. Boschung, A. Nauels, Y. Xia, V. Bex, and P. Midgley, *Climate Change 2013: the Physical Science Basis - Working Group I Contribution to the Fifth Assessment Report of the Intergovernmental Panel on Climate Change*. Cambridge University Press, 2014.

[2] International Energy Agency, "Energy Technology Perspectives," 2017.

[3] International Energy Agency, "Key world energy statistics," 2018.

[4] M. A. Green, Y. Hishikawa, E. D. Dunlop, D. H. Levi, J. Hohl, E. Masahiro, Y. Anita, and W. Y. H. Baillie, "Solar cell efficiency tables (Version 53)," *Progre*, vol. 27, pp. 3–12, 2019.

[5] N. R. E. Laboratory, "Best research-cell efficiencies," 2019.

[6] J. J. Schermer, G. J. Bauhuis, P. Mulder, E. J. Haverkamp, J. van Deelen, A. T. J. van Niftrik, and P. K. Larsen, "Photon confinement in high-efficiency, thin-film III-V solar cells obtained by epitaxial lift-off," *Thin Solid Films*, vol. 511-512, pp. 645–653, 2006.

[7] M. A. Green, K. Emery, D. L. King, S. Igari, and W. Warta, "Solar Cell Efficiency Tables (Version 25)," *Progress in Photovoltaics: Research and Applications*, vol. 13, pp. 49–54, 2005.

[8] G. J. Bauhuis, P. Mulder, E. J. Haverkamp, J. C. C. M. Huijben, and J. J. Schermer, "26.1% thin-film GaAs solar cell using epitaxial lift-off," *Solar Energy Materials and Solar Cells*, vol. 93, no. 9, pp. 1488–1491, 2009.

[9] O. D. Miller, E. Yablonovitch, and S. R. Kurtz, "Intense internal and external fluorescence as solar cell approach the SQ efficiency limit," *Photovoltaics, IEEE Journal of*, vol. 2, no. 3, pp. 1–27, 2012.

[10] B. R. Elbert, *Introduction to Satellite Comunication*. Artech House, 2008.

[11] N. J. Smeenk, C. Mooney, J. Feenstra, P. Mulder, T. Rohr, C. O. A. Semprimoschnig, E. Vlieg, and J. J. Schermer, "Space environmental testing of flexible coverglass alternatives based on siloxanes," *Polymer Degradation and Stability*, vol. 98, no. 12, pp. 2503–2511, 2013.

[12] M. A. Green, "General temperature dependence of solar cell performance and implications for device modelling," *Progress in Photovoltaics: Research and Applications*, vol. 11, no. 5, pp. 333–340, 2003.

[13] C. Brandt, C. Baur, A. Caon, P. Müller-Buschbaum, C. Zimmermann, and T. Andreev, "The influence of high temperatures on radiation damage of gainp$_2$/gaas/ge triple junction cells," *IEEE Journal of Photovoltaics*, vol. 3, pp. 904–908, April 2013.

[14] E. Grossman and I. Gouzman, "Space environment effects on polymers in low earth orbit," *Nuclear Instruments and Methods in Physics Research Section B: Beam Interactions with Materials and Atoms*, vol. 208, pp. 48 – 57, 2003. Ionizing Radiation and Polymers.

[15] European Space Agency, "Could High-Altitude Pseudo-Satellites Transform the Space Industry?." https://www.esa.int, 2019.

[16] Airbus, "Zephyr - UAV - Airbus." https://www.airbus.com/defence/uav/zephyr.html, 2019. [Online; accessed 12 August 2019].

[17] A. Smets, K. Jäger, O. Isabella, R. Swaaij, van, and M. Zeman, *Solar energy : the physics and engineering of photovoltaic conversion technologies and systems*. UIT Cambridge, 2016.

[18] T. Dittrich, *Materials Concepts for Solar Cells.* Imperial College Press, 2014.

[19] M. A. Steiner, J. F. Geisz, I. García, D. J. Friedman, A. Duda, and S. R. Kurtz, "Optical enhancement of the open-circuit voltage in high quality GaAs solar cells," *Journal of Applied Physics*, vol. 113, no. 123109, 2013.

[20] M. P. Lumb, M. A. Steiner, J. F. Geisz, and R. J. Walters, "Incorporating photon recycling into the analytical drift-diffusion model of high efficiency solar cells," *Journal of Applied Physics*, vol. 116, no. 19, 2014.

[21] H. M. Manasevit, "Single-crystal gallium arsenide on insullating substrates," *Applied Physics Letters*, vol. 12, no. 4, pp. 156–159, 1968.

[22] M. Konagai, M. Sugimoto, and K. Takahashi, "High efficiency GaAs thin film solar cells by peeled film technology," *Journal of Crystal Growth*, vol. 45, no. C, pp. 277–280, 1978.

[23] E. Yablonovitch, T. Gmitter, J. P. Harbison, and R. Bhat, "Extreme selectivity in the lift-off of epitaxial GaAs films," *Applied Physics Letters*, vol. 51, no. 26, pp. 2222–2224, 1987.

[24] M. M. A. J. Voncken, J. J. Schermer, A. T. J. van Niftrik, G. J. Bauhuis, P. Mulder, P. K. Larsen, T. P. J. Peters, B. de Bruin, A. Klaassen, and J. J. Kelly, "Etching AlAs with HF for Epitaxial Lift-Off Applications," *Journal of The Electrochemical Society*, vol. 151, no. 5, p. G347, 2004.

[25] M. M. A. J. Voncken, J. J. Schermer, G. J. Bauhuis, P. Mulder, and P. K. Larsen, "Multiple release layer study of the intrinsic lateral etch rate of the epitaxial lift-off process," *Applied Physics A: Materials Science and Processing*, vol. 79, no. 7, pp. 1801–1807, 2004.

[26] G. J. Bauhuis, J. J. Schermer, P. Mulder, M. M. A. J. Voncken, and P. K. Larsen, "Thin film GaAs solar cells with increased quantum efficiency due to light reflection," *Solar Energy Materials and Solar Cells*, vol. 83, no. 1, pp. 81–90, 2004.

[27] J. J. Schermer, P. Mulder, G. J. Bauhuis, M. M. A. J. Voncken, J. Van Deelen, E. Haverkamp, and P. K. Larsen, "Epitaxial Lift-Off for large area thin film III/V devices," *Physica Status Solidi (A) Applications and Materials Science*, vol. 202, no. 4, pp. 501–508, 2005.

[28] J. J. Schemer, P. Mulder, G. J. Bauhuis, P. K. Larsen, G. Oomen, and E. Bongers, "Thin-film GaAs epitaxial lift-off solar cells for space applications," *Progress in Photovoltaics: Research and Applications*, vol. 13, no. 7, pp. 587–596, 2005.

[29] G. J. Bauhuis, P. Mulder, E. J. Haverkamp, J. J. Schermer, E. Bongers, G. Oomen, W. Köstler, and G. Strobl, "Wafer reuse for repeated growth of III-V solar cells," *Progress in Photovoltaics: Research and Applications*, vol. 18, no. 3, pp. 155–159, 2010.

[30] F. L. Wu, S. L. Ou, R. H. Horng, and Y. C. Kao, "Improvement in separation rate of epitaxial lift-off by hydrophilic solvent for GaAs solar cell applications," *Solar Energy Materials and Solar Cells*, vol. 122, pp. 233–240, 2014.

[31] C. L. Stender, J. Adams, V. Elarde, T. Major, H. Miyamoto, M. Osowski, N. Pan, R. Tatavarti, F. Tuminello, A. Wibowo, C. Youtsey, and G. Ragunathan

[32] X. Li, P. C. Li, L. Ji, C. Stender, S. R. Tatavarti, K. Sablon, and E. T. Yu, "Integration of subwavelength optical nanostructures for improved antireflection performance of mechanically flexible GaAs solar cells fabricated by epitaxial lift-off," *Solar Energy Materials and Solar Cells*, vol. 143, pp. 567–572, 2015.

[33] H. Bernas, J. Chaumont, E. Cottereau, R. Meunier, A. Traverse, C. Clerc, O. Kaitasov, F. Lalu, D. L. Du, G. Moroy, and M. Salomé, "Progress report on Aramis, the 2 MV tandem at Orsay," *Nuclear Instruments and Methods in Physics Research Section B: Beam Interactions with Materials and Atoms*, vol. 62, no. 3, pp. 416 – 420, 1992.

[34] N. Núñez, J. R. González, M. Vázquez, C. Algora, and P. Espinet, "Evaluation of the reliability of high concentrator GaAs solar cells by means of temperature accelerated aging tests," *Progress in Photovoltaics: Research and Applications*, vol. 21, pp. 1104–1113, 2013.

[35] ESA-ESTEC Requirements & Standards Division, "ECSS-E-ST-20-08C, Space Engineering: Photovoltaic assemblies and components," 2012.

[36] M. A. Green, Y. Hishikawa, W. Warta, E. D. Dunlop, D. H. Levi, J. Hohl-Ebinger, and A. W. Ho-Baillie, "Solar cell efficiency tables (version 50)," *Progress in Photovoltaics: Research and Applications*, vol. 25, no. 7, pp. 668–676, 2017.

[37] W. Shockley and H. J. Queisser, “Detailed balance limit of efficiency of p-n junction solar cells,” *Journal of Applied Physics*, vol. 32, no. 3, pp. 510–519, 1961.

[38] X. Wang, M. R. Khan, J. L. Gray, M. A. Alam, and M. S. Lundstrom, “Design of gaas solar cells operating close to the shockley-queisser limit,” *IEEE Journal of Photovoltaics*, vol. 3, no. 2, pp. 737–744, 2013.

[39] E. D. E. Kosten, J. H. J. Atwater, J. Parsons, A. Polman, and H. A. Atwater, “Highly efficient GaAs solar cells by limiting light emission angle,” *Light: Science & Applications*, vol. 2, no. 1, pp. 1–6, 2013.

[40] F. Cappelluti, G. Ghione, M. Gioannini, G. Bauhuis, P. Mulder, J. Schermer, and M. Cimino, “Novel Concepts for High-Efficiency Lightweight Space Solar Cells,” *E3S Web of Conferences*, vol. 16, no. 1, p. 03007, 2017.

[41] N. Vandamme, H. L. Chen, A. Gaucher, B. Behaghel, A. Lemaître, A. Cattoni, C. Dupuis, N. Bardou, J. F. Guillemoles, and S. Collin, “Ultrathin GaAs solar cells with a silver back mirror,” *IEEE Journal of Photovoltaics*, vol. 5, no. 2, pp. 565–570, 2015.

[42] S. M. Lee, A. Kwong, D. Jung, J. Faucher, R. Biswas, L. Shen, D. Kang, M. L. Lee, and J. Yoon, “High Performance Ultrathin GaAs Solar Cells Enabled with Heterogeneously Integrated Dielectric Periodic Nanostructures,” *ACS Nano*, vol. 9, no. 10, pp. 10356–10365, 2015.

[43] W. Yang, J. Becker, Y. S. Kuo, J. J. Li, S. Liu, B. Landini, K. Campman, and Y. H. Zhang, “Ultra-thin GaAs single-junction solar cells integrated with an AlInP layer for reflective back scattering,” *Conference Record of the IEEE Photovoltaic Specialists Conference*, vol. 203105, pp. 3329–3332, 2014.

[44] K. Nakayama, K. Tanabe, and H. A. Atwater, “Plasmonic nanoparticle enhanced light absorption in GaAs solar cells,” *Applied Physics Letters*, vol. 93, no. 12, pp. 2006–2009, 2008.

[45] G. Bauhuis, P. Mulder, Y. Y. Hu, and J. Schermer, “Deep junction III-V solar cells with enhanced performance,” *Physica Status Solidi (A) Applications and Materials Science*, vol. 213, no. 8, pp. 2216–2222, 2016.

[46] J. E. Parrott, “Radiative recombination and photon recycling in photovoltaic solar cells,” *Solar Energy Materials and Solar Cells*, vol. 30, no. 3, pp. 221–231, 1993.

[47] G. B. Lush, “B-coefficient in n-type GaAs,” *Solar Energy Materials and Solar Cells*, vol. 93, no. 8, pp. 1225–1229, 2009.

[48] B. M. Kayes, H. Nie, R. Twist, S. G. Spruytte, F. Reinhardt, I. C. Kizilyalli, and G. S. Higashi, “27.6% Conversion efficiency, a new record for single-junction solar cells under 1 sun illumination,” *Conference Record of the IEEE Photovoltaic Specialists Conference*, pp. 4–8, 2011.

[49] V. Ganapati, M. A. Steiner, and E. Yablonovitch, “The Voltage Boost Enabled by Luminescence Extraction in Solar Cells,” *IEEE Journal of Photovoltaics*, vol. 6, no. 4, pp. 801–809, 2016.

[50] S. T. Hwang, S. Kim, H. Cheun, H. Lee, B. Lee, T. Hwang, S. Lee, W. Yoon, H. M. Lee, and B. Park, “Bandgap grading and Al0.3Ga0.7As heterojunction emitter for highly efficient GaAs-based solar cells,” *Solar Energy Materials and Solar Cells*, vol. 155, pp. 264–272, 2016.

[51] “SOPRA n-k database.”

[52] E. F. Schubert, *Light-Emitting Diodes*. 2006.

[53] P. Espinet-González, I. Rey-Stolle, M. Ochoa, C. Algora, I. García, and E. Barrigón, “Analysis of perimeter recombination in the subcells of GaInP / GaAs / Ge triple-junction solar cells,” *Prog. Photovolt: Res. Appl.*, vol. 23, pp. 874–882, 2015.

[54] J. Adams, V. Elarde, A. Hains, C. Stender, F. Tuminello, C. Youtsey, A. Wibowo, and M. Osowski, “Demonstration of multiple substrate reuses for inverted metamorphic solar cells,” in *Photovoltaic Specialists Conference (PVSC), Volume 2, 2012 IEEE 38th*, pp. 1–6, IEEE, 2012.

[55] M. van Eerden, G. Bauhuis, P. Mulder, N. Gruginskie, M. Passoni, L. Andreani, E. Vlieg, and J. Schermer, “A Facile Light Trapping Approach for Ultra-Thin GaAs Solar Cells using Wet Chemical Etching,” *Progress in Photovoltaics: Research and Applications*, Submitted.

[56] L. C. Hirst, M. K. Yakes, J. H. Warner, M. F. Bennett, K. J. Schmieder, R. J. Walters, and P. P. Jenkins, "Intrinsic radiation tolerance of ultra-thin GaAs solar cells," *Applied Physics Letters*, vol. 109, no. 3, 2016.

[57] N. Gruginskie, F. Cappelluti, G. Bauhuis, P. Mulder, E. Haverkamp, E. Vlieg, and J. Schermer, "Electron radiation induced degradation of GaAs solar cells with different architectures," *Progress in Photovoltaics: Research and Applications*, 2019.

[58] J. Feenstra, R. H. V. Leest, N. J. Smeenk, G. Oomen, E. Bongers, P. Mulder, E. Vlieg, and J. J. Schermer, "Flexible shielding layers for solar cells in space applications," vol. 28, p. 43661, 2016.

[59] S. Moon, K. Kim, Y. Kim, J. Heo, and J. Lee, "Highly efficient single-junction GaAs thin-film solar cell on flexible substrate," *Scientific Reports*, vol. 6, no. February, pp. 1–6, 2016.

[60] P. Kwak, N. Kim, J. Kim, D. Kim, K. Song, and J. Lee, "Flexible space solar cell array with radiation shield fabricated by guided-printing of cover glasses," *Solar Energy Materials and Solar Cells*, vol. 169, pp. 210–214, 2017.

[61] S. T. Hwang, T. Hwang, S. Lee, B. Gil, and B. Park, "Selective rear contact for Ga0.5In0.5P- and GaAs- based solar cells," *Solar Energy Materials and Solar Cells*, vol. 182, no. March, pp. 348–353, 2018.

[62] E. D. Kosten, B. M. Kayes, and H. A. Atwater, "Experimental demonstration of enhanced photon recycling in angle-restricted GaAs solar cells," *Energy and Environmental Science*, vol. 7, no. 6, pp. 1907–1912, 2014.

[63] A. W. Walker, O. Höhn, D. N. Micha, B. Bläsi, A. W. Bett, and F. Dimroth, "Impact of Photon Recycling on GaAs Solar Cell Designs," *IEEE Journal of Photovoltaics*, 2015.

[64] N. Gruginskie, S. van Laar, G. Bauhuis, P. Mulder, M. van Eerden, E. Vlieg, and J. Schermer, "Increased performance of thin-film GaAs solar cells by rear contact/mirror patterning," *Thin Solid Films*, vol. 660, pp. 10–18, 2018.

[65] D. N. Micha, O. Hohn, E. Oliva, A. W. Bett, and F. Dimroth, "Development of back side technology for light trapping and photon recycling in GaAS solar cells," *Progress in Photovoltaics: Research and Applications*, no. 27, pp. 163–170, 2019.

[66] C. L. Schilling, O. Höhn, D. N. Micha, S. Heckelmann, V. Klinger, E. Oliva, S. W. Glunz, and F. Dimroth, "Combining photon recycling and concentrated illumination in a GaAs heterojunction solar cell," *IEEE Journal of Photovoltaics*, vol. 8, no. 1, pp. 348–354, 2018.

[67] J. Yoon, S. Jo, I. S. Chun, I. Jung, H.-S. Kim, M. Meitl, E. Menard, X. Li, J. J. Coleman, U. Paik, and J. a. Rogers, "GaAs photovoltaics and optoelectronics using releasable multilayer epitaxial assemblies.," *Nature*, vol. 465, no. 7296, pp. 329–33, 2010.

[68] M. Sotoodeh, A. H. Khalid, and A. A. Rezazadeh, "Empirical low-field mobility model for III-V compounds applicable in device simulation codes," *Journal of Applied Physics*, vol. 87, no. 6, pp. 2890–2900, 2000.

[69] Y. Sun, A. Perna, and P. Bermel, "Comparing Front- and Rear-Junction GaInP Photovoltaic Devices Through Detailed Numerical and Analytical Modeling," *IEEE Journal of Photovoltaics*, vol. 9, no. 2, pp. 437–445, 2019.

[70] S. Adachi, "GaAs, AlAs and AlxGa1-xAs: Materials parameters for use in research and device applications," *Journal of applied physics*, vol. 58, no. 3, pp. 1–29, 1985.

[71] E. D. Palik, "Handbook of optical constants of solids," *Acdemic Press*, vol. 3, 1998.

[72] Y. Jiang, S. Pillai, and M. A. Green, "Realistic silver optical constants for plasmonics," vol. 6, p. 30605, 2016.

[73] J. Nelson, *The physics of solar cells.* Imperial College Press, 2003.

[74] M. Ochoa, C. Algora, P. Espinet-González, and I. García, "3-D modeling of perimeter recombination in GaAs diodes and its in fl uence on concentrator solar cells," *Solar Energy Materials and Solar Cells*, vol. 120, pp. 48–58, 2014.

[75] C. J. Sandroff, R. N. Nottenburg, J. Bischoff, and R. Bhat, "Dramatic enhancement in the gain of a GaAs/AlGaAs heterostructure bipolar transistor by surface chemical passivation," *Applied Physics Letters*, vol. 51, no. 1, pp. 33–35, 1987.

[76] M. T. Sheldon, C. N. Eisler, and H. A. Atwater, "Gaas passivation with trioctylphosphine sulfide for enhanced solar cell efficiency and durability," *Advanced Energy Materials*, vol. 2, no. 3, pp. 339–344, 2012.

[77] T. Nakano, T. Shioda, N. Enomoto, E. Abe, M. Sugiyama, Y. Nakano, and Y. Shimogaki, "Precise structure control of GaAs/InGaP hetero-interfaces using metal organic vapor phase epitaxy and its abruptness analyzed by STEM," *Journal of Crystal Growth*, vol. 347, no. 1, pp. 25–30, 2012.

[78] Y. Fukushima, T. Nakano, Y. Nakano, and Y. Shimogaki, "Control of In Surface Segregation and Inter- Diffusion in GaAs on InGaP Grown by Metal – Organic Vapor Phase Epitaxy," *Japanese Journal of Applied Physics*, vol. 51, p. 055601, 2012.

[79] N. P. Wells, T. U. Driskell, A. I. Hudson, S. D. Lalumondiere, W. T. Lotshaw, D. V. Forbes, S. M. Hubbard, W. T. Lotshaw, D. V. Forbes, and S. M. Hubbard, "Carrier quenching in InGaP / GaAs double heterostructures," *Journal of Applied Physics*, vol. 118, p. 065703, 2015.

[80] M. C. López-escalante, M. Gabás, I. García, E. Barrigón, I. Rey-stolle, and C. Algora, "Applied Surface Science Differences between GaAs / GaInP and GaAs / AlInP interfaces grown by movpe revealed by depth profiling and angle-resolved X-ray photoelectron spectroscopies," *Applied Surface Science*, vol. 360, pp. 477–484, 2016.

[81] M. A. Green, Y. Hishikawa, E. D. Dunlop, D. H. Levi, J. Hohl-Ebinger, and A. W. Ho-Baillie, "Solar cell efficiency tables (version 51)," *Progress in Photovoltaics: Research and Applications*, vol. 26, no. 1, pp. 3–12, 2018.

[82] G. F. Strobl, L. Ebel, D. Fuhrmann, W. Guter, R. Kern, V. Khorenko, W. Kostler, and M. Meusel, "Development of lightweight space solar cells with 30% efficiency at end-of-life," *2014 IEEE 40th Photovoltaic Specialist Conference, PVSC 2014*, pp. 3595–3600, 2014.

[83] C. Colin, A. Jaouad, M. Darnon, M. De Lafontaine, M. Volatier, A. Boucherif, R. Arès, S. Fafard, and V. Aimez, "The handling of thin substrates and its potential for new architectures in multi-junction solar cells technology," *AIP Conference Proceedings*, vol. 1881, no. 1, p. 040001, 2017.

[84] R. Tatavarti, G. Hillier, A. Dzankovic, G. Martin, F. Tuminello, R. Navaratnarajah, G. Du, D. P. Vu, and N. Pan, "Lightweight, low cost gaas solar cells on 4- epitaxial liftoff (elo) wafers," *Proceedings 33rd IEEE Photovoltaic Specialists Conference*, pp. 1–4, 2008.

[85] S. Saravanan, T. Krishna Teja, R. S. Dubey, and S. Kalainathan, "Design and analysis of GaAs thin film solar cell using an efficient light trapping bottom structure," *Materials Today: Proceedings*, vol. 3, no. 6, pp. 2463–2467, 2016.

[86] F. Cappelluti, D. Kim, M. van Eerden, A. P. Cédola, T. Aho, G. Bissels, F. Elsehrawy, J. Wu, H. Liu, P. Mulder, G. Bauhuis, J. Schermer, T. Niemi, and M. Guina, "Light-trapping enhanced thin-film III-V quantum dot solar cells fabricated by epitaxial lift-off," *Solar Energy Materials and Solar Cells*, vol. 181, no. October 2017, pp. 83–92, 2018.

[87] N. Z. Vagidov, K. H. Montgomery, G. K. Bradshaw, and D. A. Wilt, "Light trapping structures for radiation hardness enhancement of space solar cells," *Solar Energy Materials and Solar Cells*, vol. 182, no. March, pp. 136–141, 2018.

[88] J. F. Geisz, M. A. Steiner, I. García, S. R. Kurtz, and D. J. Friedman, "Enhanced external radiative efficiency for 20.8% single-junction GaInP solar cells," *Appl. Phys. Lett.*, vol. 103, no. July, p. 041118, 2013.

[89] M. Yamaguchi and C. Amano, "Numerical analysis for radiation-resistant GaAs heteroface solar cell structures," *Journal of Applied Physics*, vol. 57, no. 2, pp. 537–544, 1985.

[90] M. A. Steiner, M. P. Lumb, R. Hoheisel, J. F. Geisz, R. M. France, D. Scheiman, R. J. Walters, and P. P. Jenkins, "Radiation effects on luminescent coupling in iii–v solar cells," in *2015 IEEE 42nd Photovoltaic Specialist Conference (PVSC)*, pp. 1–5, 2015.

[91] R. H. van Leest, P. Mulder, N. Gruginskie, S. C. W. V. Laar, G. J. Bauhuis, H. Cheun, H. Lee, W. Yoon, R. V. D. Heijden, E. Bongers, E. Vlieg, and J. J. Schermer, "Temperature-Induced Degradation of Thin-Film III – V Solar Cells for Space Applications," no. 1, pp. 1–7, 2016.

[92] J. C. Bourgoin and M. Zazoui, “Irradiation-induced degradation in solar cell: Characterization of recombination centres,” *Semiconductor Science and Technology*, vol. 17, no. 5, pp. 453–460, 2002.

[93] J. H. Warner, S. R. Messenger, R. J. Walters, G. P. Summers, J. R. Lorentzen, D. M. Wilt, and M. A. Smith, “Correlation of electron radiation induced-damage in gaas solar cells,” *IEEE Transactions on Nuclear Science*, vol. 53, no. 4, pp. 1988–1994, 2006.

[94] M. Salzberger, M. Rutzinger, C. Nömayr, P. Lugli, and C. G. Zimmermann, “Voltage-dependent photocurrent in irradiated GaAs solar cells,” *Progress in Photovoltaics: Research and Applications*, no. September 2017, pp. 1–7, 2018.

[95] C. Pellegrino and C. G. Zimmermann, “Difference in space - charge recombination of proton and electron irradiated GaAs solar cells,” *Progress in Photovoltaics: Research and Applications*, vol. 27, no. November 2018, pp. 379–390, 2019.

[96] B. E. Anspaugh, “GaAs Solar Cell Radiation Handbook,” 1996.

[97] H. Mazouz, P. O. Logerais, A. Belghachi, O. Riou, F. Delaleux, and J. F. Durastanti, “Effect of electron irradiation fluence on the output parameters of GaAs solar cell,” *International Journal of Hydrogen Energy*, vol. 40, no. 39, pp. 13857–13865, 2015.

[98] M. Imaizumi, S. J. Taylor, M. Yamaguchi, T. Ito, T. Hisamatsu, and S. Matsuda, “Analysis of structure change of Si solar cells irradiated with high fluence electrons,” *Journal of Applied Physics*, vol. 85, no. 3, pp. 1916–1920, 1999.

[99] M. Wolf and H. Rauschenbach, “Series resistance effects on solar cell measurements,” *Advanced Energy Conversion*, vol. 3, pp. 455–479, 1963.

[100] H. Hovel, *Semiconductors and semimetals. Volume 11. Solar cells.* 1975.

[101] M. P. Lumb, C. G. Bailey, J. G. J. Adams, G. Hillier, F. Tuminello, V. C. Elarde, and R. J. Walters, “Extending the 1-d hovel model for coherent and incoherent back reflections in homojunction solar cells,” *IEEE Journal of Quantum Electronics*, vol. 49, no. 5, pp. 462–470, 2013.

[102] S. Tiwari and S. L. Wright, “Material properties of p-type gaas at large dopings,” *Applied Physics Letters*, vol. 56, no. 6, pp. 563–565, 1990.

[103] M. K. Hudait, P. Modak, and S. B. Krupanidhi, “Si incorporation and Burstein–Moss shift in n-type GaAs,” *Materials Science and Engineering: B*, vol. 60, no. 1, pp. 1–11, 1999.

[104] C.-T. Sah, R. N. Noyce, and W. Shockley, “Carrier Generation and Recombination in P-N Junctions,” *Proceedings of the IRE*, vol. 45, no. 9, p. 1243, 1957.

[105] K. Bertness, B. Cavicchi, S. Kurtz, J. Olson, A. Kibbler, and C. Kramer, “Effect of base doping on radiation damage in GaAs single junction solar cells,” *Conference Record of the Twenty-Second IEEE Photovoltaic Specialists Conference*, vol. 2, pp. 1582–1587, 1991.

[106] R. Hoheisel, M. Gonzalez, M. P. Lumb, D. A. Scheiman, S. R. Messenger, C. G. Bailey, J. Lorentzen, T. N. Tibbits, M. Imaizumi, T. Ohshima, S. Sato, P. P. Jenkins, and R. J. Walters, “Quantum-well solar cells for space: The impact of carrier removal on end-of-life device performance,” *IEEE Journal of Photovoltaics*, vol. 4, no. 1, pp. 253–259, 2014.

[107] L. Ming, W. Rong, Y. Kui, and Y. Tiancheng, “Photoluminescence analysis of electron irradiation-induced defects in GaAs/Ge space solar cells,” *Nuclear Instruments and Methods in Physics Research, Section B: Beam Interactions with Materials and Atoms*, vol. 312, pp. 137–140, 2013.

[108] P. Dai, L. Ji, M. Tan, S. Uchida, Y. Wu, A. Abduwayiti, M. Heini, Q. Guo, L. Bian, S. Lu, and H. Yang, “Electron irradiation study of room-temperature wafer-bonded four-junction solar cell grown by MBE,” *Solar Energy Materials and Solar Cells*, vol. 171, pp. 118–122, 2017.

[109] A. Walker, S. Heckelmann, T. Tibbits, D. Lackner, A. Bett, and F. Dimroth, “Electron irradiation study of room-temperature wafer-bonded four-junction solar cell grown by MBE,” *Solar Energy Materials and Solar Cells*, vol. 171, pp. 118–122, 2017.

[110] R. H. Maurer, G. A. Herbert, J. D. Kinnison, and A. Meulenberg, “Gallium arsenide solar cell radiation damage study,” *IEEE Transactions on Nuclear Science*, vol. 36, no. 6, pp. 2083–2091, 1989.

[111] C. Baur, M. Gervasi, P. Nieminen, S. Pensotti, P. G. Rancoita, and M. Tacconi, "NIEL Dose Dependence for Solar Cells Irradiated with Electrons and Protons," in *Proceedings, 14th ICATPP Conference on Astroparticle, Particle, Space Physics and Detectors for Physics Applications (ICATPP 2013): Como, Italy, September 23-27, 2013*, pp. 692–707, 2014.

[112] S. M. Sze, *Physics of Semiconductor Devices: 2nd Edition.* John Wiley and Sons, 1981.

[113] J. F. Geisz, S. Kurtz, M. W. Wanlass, J. S. Ward, A. Duda, D. J. Friedman, J. M. Olson, W. E. McMahon, T. E. Moriarty, and J. T. Kiehl, "High-efficiency GaInP/GaAs/InGaAs triple-junction solar cells grown inverted with a metamorphic bottom junction," *Applied Physics Letters*, vol. 91, p. 023502, 2007.

[114] M. Stan, D. A. Aiken, B. Cho, A. Cornfeld, V. Ley, P. Patel, P. Sharps, and T. Varghese, "High-efficiency quadruple junction solar cells using OMVPE with inverted metamorphic device structures," *Journal of Crystal Growth*, vol. 312, pp. 1370–1374, 2010.

[115] R. M. France, J. F. Geisz, I. García, M. A. Steiner, W. E. McMahon, D. J. Friedman, T. E. Moriarty, C. Osterwald, J. S. Ward, A. Duda, M. Young, and W. Olavarria, "Quadruple-Junction Inverted Metamorphic Concentrator Devices," *IEEE Journal of Photovoltaics*, vol. 5, pp. 432–437, 2015.

[116] F. Dimroth, T. N. D. Tibbits, M. Niemeyer, P. F., P. Beutel, C. Karcher, E. Oliva, G. Siefer, D. Lackner, P. Fuß-Kailuweit, A. W. Bett, R. Krause, C. Drazek, E. Guiot, J. Wasselin, A. Tauzin, and T. Signamarcheix, "Four-Junction Wafer-Bonded Concentrator Solar Cells," *IEEE Journal of Photovoltaics*, vol. 6, pp. 343–349, 2016.

[117] M. A. Steiner, J. F. Geisz, J. S. Ward, I. García, D. J. Friedman, R. R. King, P. T. Chiu, R. M. France, A. Duda, W. J. Olavarria, M. Young, and S. R. Kurtz, "Optically Enhanced Photon Recycling in Mechanically Stacked Multijunction Solar Cells," *IEEE Journal of Photovoltaics*, vol. 6, pp. 358–365, 2016.

[118] A. van Geelen, P. R. Hageman, G. J. Bauhuis, P. C. van Rijsingen, P. Schmidt, and L. Giling, "Epitaxial lift-off GaAs solar cell from a reusable GaAs substrate," *Materials Science and Engineering*, vol. B45, pp. 162–171, 1997.

[119] J. van Deelen, G. J. Bauhuis, J. J. Schermer, P. Mulder, E. J. Haverkamp, and P. K. Larsen, "On the development of high-efficiency thin-film GaAs and $GaInP_2$ cells," *Journal of Crystal Growth*, vol. 298, pp. 772–776, 2007.

[120] S. W. Bedell, D. Sharjerdi, B. Hekmatshoar, K. Fogel, P. A. Lauro, J. A. Ott, N. Sosa, and D. Sadana, "Kerf-Less Removal of Si, Ge, and III-V Layers by Controlled Spalling to Enable Low-Cost PV Technologies," *IEEE Journal of Photovoltaics*, vol. 2, pp. 141–147, 2012.

[121] D. Shahrjerdi, S. W. Bedell, C. Ebert, C. Bayram, B. Hekmatshoar, K. Fogel, P. Lauro, M. Gaynes, T. Gokmen, J. A. Ott, and D. K. Sadana, "High-efficiency thin-film InGaP/InGaAs/Ge tandem solar cells enabled by controlled spalling technology," *Applied Physics Letters*, vol. 100, p. 053901, 2012.

[122] J. Adams, V. Elarde, A. Hains, C. Stender, F. Tuminello, C. Youtsey, A. Wibowo, and M. Osowski, "Demonstration of Multiple Substrate Reuses for Inverted Metamorphic Solar Cells," *IEEE Journal of Photovoltaics*, vol. 3, pp. 899–903, 2013.

[123] R. France, J. Geisz, I. García, M. Steiner, W. McMahon, D. Friedman, T. Moriarty, C. Osterwald, J. Ward, A. Duda, M. Young, and W. Olavarria, "Design Flexibility of Ultrahigh Efficiency Four-Junction Inverted Metamorphic Solar Cells," *IEEE Journal of Photovoltaics*, vol. 6, pp. 578–583, 2016.

[124] I. Garcia, R. M. France, J. F. Geisz, W. E. McMahon, M. A. Steiner, S. Johnston, and D. J. Friedman, "Metamorphic III-V Solar Cells: Recent Progress and Potential," *IEEE Journal of Photovoltaics*, vol. 6, pp. 366–373, 2016.

[125] C. Morioka, K. Shimazaki, S. Kawakita, M. Imaizumi, H. Yamaguchi, T. Takamoto, S. Sato, T. Ohshima, Y. Nakamura, K. Hirako, and M. Takahashi, "First flight demonstration of film-laminated InGaP/GaAs and Cigs thin-film solar cells by JAXA's small satellite in LEO," *Progress in Photovoltaics: Research and Applications*, vol. 19, pp. 825–833, 2011.

[126] P. Patel, D. Aiken, A. Boca, B. Cho, D. Chumney, M. Clevenger, A. Cornfeld, N. Fatemi, Y. Lin, J. McCarty, F. Newman, P. Sharps, J. Spann, M. Stan, J. Steinfeldt, C. Strautin, and T. Varghese, "Experimental Results From Performance Improvement and Radiation Hardening of Inverted Metamorphic Multijuction Solar Cells," *IEEE Journal of Photovoltaics*, vol. 2, pp. 377–381, 2012.

[127] C. Youtsey, J. Adams, R. Chan, V. Elarde, G. Hillier, M. Osowski, D. Mccallum, H. Miyamoto, N. Pan, C. Stender, R. Tatavarti, F. Tuminello, and A. Wibowo, "Epitaxial Lift-Off of Large-Area GaAs Thin-Film Multi-Junction Solar Cells," *CS MANTECH Conference*, pp. 4–7, 2012.

[128] N. Pan, "Epitaxial Lift-Off of Large-Area GaAs Multi-Junction Solar Cells for High Efficiency Clean and Portable Energy Power Generation," in *Proceedings of the 11th IEEE International Conference on Semiconductor Electronics*, 2014.

[129] C. L. Stender, C. Youtsey, F. Tuminello, M. Osowski, J. Adams, V. Elarde, H. Miyamoto, A. Wibowo, G. Hillier, R. Tatavarti, and N. Pan, "S4-P8: Applications for epitaxial lift-off of III-V materials," *Lester Eastman Conference 2014 - High Performance Devices, LEC 2014*, pp. 3–5, 2014.

[130] S. W. Bedell, K. Fogel, P. Lauro, D. Shahrjerdi, J. A. Ott, and D. Sadana, "Layer transfer by controlled spalling," *Journal of Physics D: Applied Physics*, vol. 46, p. 152002, 2013.

[131] D. Shahrjerdi, S. W. Bedell, C. Bayram, C. C. Lubguban, K. Fogel, P. Lauro, J. A. Ott, M. Hopstaken, M. Gayness, and D. Sadana, "Ultralight High-Efficiency Flexible InGaP/(In)GaAs Tandem Solar Cells on Plastic," *Advanced Energy Materials*, vol. 3, pp. 566–571, 2013.

[132] R. N. Hall and J. H. Racette, "Diffusion and solubility of copper in extrinsic and intrinsic germanium, silicon, and gallium arsenide," *Journal of Applied Physics*, vol. 35, no. 2, pp. 379–397, 1964.

[133] S. Sze and J. Irvin, "Resistivity, mobility and impurity levels in GaAs, Ge, and Si at 300°K," *Solid-State Electronics*, vol. 11, no. 6, pp. 599–602, 1968.

[134] N. Nuñez, M. Vazquez, V. Orlando, P. Espinet-González, and C. Algora, "Semi-quantitative temperature accelerated life test (ALT) for the reliability qualification of concentrator solar cells and cell on carriers," *Progress in Photovoltaics: Research and Applications*, vol. 23, no. 12, pp. 1857–1866, 2015.

[135] M. Vázquez, C. Algora, I. Rey-Stolle, and J. R. González, "III–V Concentrator Solar Cell Reliability Prediction Based on Quantitative LED Reliability Data," *Progress in Photovoltaics: Research and Applications*, vol. 15, pp. 477–491, 2007.

[136] J. R. González, M. Vázquez, N. Núñez, C. Algora, I. Rey-Stolle, and B. Galiana

[137] R. H. Van Leest, G. J. Bauhuis, P. Mulder, R. Van Der Heijden, E. Bongers, E. Vlieg, and J. J. Schermer, "Effects of copper diffusion in gallium arsenide solar cells for space applications," *Solar Energy Materials and Solar Cells*, vol. 140, pp. 45–53, 2015.

[138] R. H. van Leest, K. de Kleijne, G. J. Bauhuis, P. Mulder, H. Cheun, H. Lee, W. Yoon, R. van der Heijden, E. Bongers, E. Vlieg, and J. J. Schermer, "Degradation mechanism(s) of GaAs solar cells with Cu contacts," *Phys. Chem. Chem. Phys.*, vol. 18, no. 15, pp. 10232–10240, 2016.

[139] R. H. van Leest, K. de Kleijne, G. J. Bauhuis, P. Mulder, R. van der Heijden, E. Bongers, E. Vlieg, and J. J. Schermer, "Copper diffusion in GaAs solar cells for space applications," in *Proceedings of the 31st European Photovoltaic Solar Energy Conference and Exhibition*, pp. 1422–1425, 2015.

[140] A. Istratov, C. Flink, and E. Weber, "Impact of the unique physical properties of copper in silicon on characterization of copper diffusion barriers," *physica status solidi (b)*, vol. 222, no. 1, pp. 261–277, 2000.

[141] F. Hasegawa, "Different diffusion behavior of copper in epitaxial and in bulk GaAs Different diffusion behavior of copper in epitaxial and in bulk GaAs," vol. 1944, no. 1974, pp. 1–5, 1974.

[142] M.-A. Nicolet, "Diffusion barriers in thin films," *Thin Solid Films*, vol. 52, no. 3, pp. 415 – 443, 1978.

List of Publications

- N. Gruginskie, F.Capelluti, G. Bauhuis, P. Mulder, E. Vlieg and J.J. Schermer. **Performance limiting mechanisms for photon recycling in thin-film GaAs solar cells**. *In preparation.*
- N. Gruginskie, F.Capelluti, M. van Eerden, G. Bauhuis, P. Mulder, E. Vlieg and J.J. Schermer. **Proton radiation induced degradation of GaAs solar cells**. *In preparation.*
- N. Gruginskie, F. Cappelluti, G. Bauhuis, P. Mulder, E.J. Haverkamp, E. Vlieg and J.J. Schermer. **Electron radiation induced degradation of GaAs solar cells with different architectures**. *Progress in Photovoltaics: Research and Application (2019).*
- N. Gruginskie, F.Capelluti, G. Bauhuis, P. Mulder, L.B. Rebouças, E. Vlieg and J.J. Schermer. **Electron and proton irradiation of GaAs solar cells with different architectures**. *Proceedings of the 12th European Space Power Conference - ESPC (2019)*
- N. Gruginskie, F. Capelluti, G. Bauhuis, P. Mulder, E. Vlieg and J.J. Schermer. **Electron and proton irradiation of GaAs solar cells**. *Proceedings of the 36th European Photovoltaics Specialists - EU-PVSEC (2019)*
- M. van Eerden, G. Bauhuis, P. Mulder, N. Gruginskie, E. Vlieg and J.J. Schermer. **A Facile Light Trapping Approach for Ultra-Thin GaAs Solar Cells using Wet Chemical Etching**. *Progress in Photovoltaics: Research and Application (2019).*
- N. Gruginskie, Federica Cappelluti, Maarten van Eerden, Ariel P. Cedola, G. Bauhuis, P. Mulder, E. Vlieg and J.J. Schermer. **Increased performance of thin-film GaAs solar cells with increased rear mirror reflectivity**. *Proceedings of the VII World Conference of Photovoltaic Energy Conversion - WCPEC-7 (2018).*

- N. Gruginskie, G. Bauhuis, P. Mulder, E. Vlieg and J.J. Schermer. **Photon recycling in thin-film GaAs solar cells**. *Proceedings of the VII Brazilian Conference of Solar Energy - VII CBENS (2018).*

  This conference paper will be published as a chapter in the book "Energy in Brazil", by Poisson publisher, Brazil (2019).

- N. Gruginskie, S.C.W. van Laar, G. Bauhuis, P. Mulder, M. van Eerden, E. Vlieg and J.J. Schermer. **Increased performance of thin-film GaAs solar cells by rear contact/mirror patterning**. *Thin Solid Films 660 (2018) 10-18.*

- R.H van Leest, P. Mulder, N. Gruginskie, S.C.W van Laar, G. Bauhuis, H. Cheun, H. Lee, W. Yoon, R. van der Heijden, E. Bongers E. Vlieg and J.J. Schermer. **Temperature induced degradation of thin-film III-V solar cells for space application**. *IEEE Journal of Photovoltaics, vol. 7, no. 2 (2017) 702-708.*

Acknowledgments

Finishing this thesis was not an easy journey, and I definitely did not get here alone. Therefore, I would like to use this space to celebrate all the great people who made this process such an outstanding time of my life. First of all, I would like to thank my daily supervisor John Schermer for allowing me this opportunity. I truly admire the way you conduct the department, and have learned so much from your mentorship. I would also like to thank my supervisor, Elias Vlieg, for the input on several manuscripts and for the inspiring work discussions.

I want to mention all of the great people that make the Applied Materials Science department an amazing working place. Research is not done easily, and I had only the best supporting me: starting by thanking my office-mates, the world class dart-thrower and solar cell expert, Gerard Bauhuis, and my running coach, old-style music enthusiast and paranymph, Peter Mulder. Even the most difficult days were made nicer by having you both as company. Thanks to Erik Haverkamp and Wil Corbeek for the support with any technical issues I might have encountered, to Ine Hendrix, for the help with many burocratic issues, and for Gunther Bissels, for the interesting discussions, being them about thin-film solar cells or about the ethical aspects of the food we eat. I also thank the colleagues that have already left (some even when I was just arriving), but I remember fondly: Joep Bos Coenraad, Remi Aninat, Yu Ying Wu, Andre Kaldenhoven, Eleni Katsia and Ashkan Tavakoli.

I was in great company with my fellow PhD students at the department, and I would like to thank you all. The ones that already made it: Aryan de Jong, Jon Feenstra, from whom I inherited the (very important) role of discussing good food during the breaks, Linda van Leest, the one who got me (briefly) addicted to the unexpectedly tasty *dropjes* and Leon Bunthof, who provided me with the best (and most fun) discussions about the most random topics. And also the ones that are still on their PhD journeys: the Rockstar and cool kid, Maarten van Eerden (RIP Foam, we'll never get over it), the extremely practical Daan van der Woude (credits for the Dutch abstract of this thesis!) and Lara Rebouças, it was great having another

Brazilian around, so I could have a Portuguese escaping route when the English language was just not enough.

A big thanks is due to the students who worked with me: Simone van Laar, Michaela Eberbach, and Valerio Trinito. Many of the insights in this thesis were only possible because of our collaboration. And to all students that have been a part of the department during my PhD: Frank, Mees, Steven, Remco, Menno, Frank II, Britt, Juul, Nathan, Edwin, Sverre, Ruben, Roy, Vit, Rik, Jasper, Job and to everyone I forgot to mention (which I am sure I did, *sorry*). Thank you all for the fun and interesting discussions and coffee breaks. Furthermore, I would also like to thank my colleagues from the Solid State Chemistry department for the day-outs and Thursday afternoon discussions.

My PhD was also a collaboration with many groups outside of the Radboud University. Therefore I want to thank everyone who in one way or another contributed to this thesis. A special thanks to Federica Cappelluti, for all the inspiring conversation and valuable input, which strengthened my PhD studies.

The ”Brazilian community” in Nijmegen is strong and vast, so I won’t even try to name everyone, because I would be bound to forget some people. But I want to acknowledge everyone who, with a barbecue, a *feijoada*, or a *June party*, brought a little bit of home to my Dutch life. An important aspect from these last four years were the new friends I made, and I want to thank you all. A special shout out to Paula de Almeida; our friendship is one of the most beautiful things that the Nederlands brought to me, and I hope we keep it for life. Thank you for being there at all times.

Durante meu doutorado eu precisei enfrentar o maior desafio de toda a minha vida, que foi me despedir da minha mãe, Rosangela Bavaresco. Ela foi uma mulher maravilhosa, forte e rodeada somente por amor. Mãezinha, eu queria que você ainda estivesse aqui, pra me ver alcançar essa vitória e eu poder te deixar orgulhosa. Eu te amo, e vou sentir saudades eternamente.

Eu não seria nada do que sou hoje, não fosse por ter tido pais maravilhosos, que merecem todo o meu reconhecimento. Então eu quero agradecer por todo o apoio e sabedoria do meu pai, Gilson Gruginskie. Paizinho, eu com toda certeza não estaria aqui se não fosse por ti. De toda e qualquer vitória minha, parte do mérito é teu!

Além disso, eu preciso agradecer de coração pelo carinho e suporte do meu segundo par de pais. Minha ”*boa*drasta” Claudete Lampert Gruginskie, por tanta ternura e acolhimento, e meu padrasto Juliano Marchetto Bavaresco, por ter sido um exemplo de bravura nos tempos mais difíceis. E como família amorosa é o que não me falta, gostaria de agradecer ao meu time de irmãos: meu manão Saulo Gruginskie, minhas meninas, Julia da Cruz Bavaresco e Isabel Lampert Gruginskie e o meu maninho, Juliano Marchetto Bavaresco Filho. Vocês são parte de mim, e eu não posso nem começar a explicar a saudade que sinto.

E por fim, ao meu parceiro Renato Bennemann, por ter embarcado nessa aventura comigo, ter entendido meus dias difíceis e ter celebrado até minhas pequenas vitórias. A vida ao teu lado é leve e colorida, e eu me considero muito sortuda por ter te encontrado. Que as nossas aventuras e celebrações continuem por muitos anos!

Com muito amor

Natasha

Curriculum vitae

Natasha Gruginskie
Born in June 16th, 1992
in Porto Alegre - Brazil

2015-2019: PhD degree in Materials Science at the Institute for Molecules and Materials (IMM), department of Applied Materials Science (AMS), at Radboud University - The Netherlands. Thesis title: ***Thin-film III-V solar cells - photon recycling and space application testing***.

2014-2015: Master's degree in Materials Engineering at the Federal University of Rio Grande do Sul (UFRGS) - Brazil. Masters dissertation title: ***Synthesis of $PbTiO_3$, $PbZrO_3$ and $Pb(Ti,Zr)O_3$ via polymeric sol-gel, thin-film production by spin-coating and characterization of micro-structural and photophysical properties***.

2009-2014: Bachelor in Energy Engineering at the State University of Rio Grande do Sul (UERGS) - Brazil. Bachelor thesis title: ***Decision support study for energetic recycling of urban solid waste in the city of Novo Hamburgo - Brazil***.